UNIVERSITY OF BELGRADE

SCHOOL OF ELECTRICAL ENGINEERING

Marko Mladenović

ELECTRONIC PROPERTIES OF INTERFACES BETWEEN DOMAINS IN ORGANIC SEMICONDUCTORS

doctoral dissertation

Belgrade, 2016.

UNIVERZITET U BEOGRADU

ELEKTROTEHNIČKI FAKULTET

Marko Mladenović

ELEKTRONSKA SVOJSTVA ORGANSKIH POLUPROVODNIKA NA GRANICAMA DOMENA

doktorska disertacija

Beograd, 2016.

To my family and friends

This thesis was entirely done in Scientific Computing Laboratory (SCL), Institute of Physics Belgrade, under supervision of Dr Nenad Vukmirović. First of all, I would like to thank Nenad for giving me the opportunity to work with him and for introducing me into the exciting world of organic semiconductors. I am gratefully thank to him for his overall support during my master and PhD studies, for teaching me a good scientific practice, for helping me to overcome obstacles I faced with. The lessons and advice I received from him I will use not only in my future carrier, but also in the rest of my life. Friendly and positive environment in SCL has contributed a lot to this work. Therefore, I am grateful to all my colleagues for creating such a nice atmosphere. At this point, I would like to mention some them by name, hopping that the others would not mind. Firstly, I would like to thank Dr Igor Stanković for help and guidance at the first stage of my work in SCL. Additionally, I would like to thank Dr Aleksandar Belić for giving me the opportunity to work at the Institute of Physics. Specially, I would like to thank Dr Antun Balaž, the head of SCL. He was always accessible to hear me and help me with the problems I had both with my research and in private life. Finally, I would like to mention two of my colleagues, but first of all my good friends, Vladimir Slavnić and Marko Opačić for their friendship all these years. In the end, I would like to thank my mother and father for their love and infinite support. I am also grateful to all my friends and professors which contributed explicitly or implicitly to this work.

This work was supported by the Ministry of Education, Science, and Technological Development of the Republic of Serbia under project ON171017 and by the European Community FP7 Marie Curie Career Integration Grant (ELECTROMAT). Numerical simulations were run on the PARADOX supercomputing facility at the Scientific Computing Laboratory of the Institute of Physics Belgrade.

Abstract

The aim of this thesis is to provide a link between atomic and electronic structure of different types of interfaces between domains in organic semiconductors. In polycrystalline small-molecule organic semiconductors interfaces are formed between single crystalline domains. We found that grain boundaries in polycrystalline naphthalene introduce trap states within the band gap of the material. Trap states are localized on closely spaced pairs of molecules from opposite sides of the boundary. Realistic conjugated polymers, such as poly(3-hexylthiophene) (P3HT), contain mixed crystalline and amorphous domains. We found that HOMO state of the interface between crystalline and amorphous domain in P3HT belongs to crystalline domains. States that belong to both domains and trap states were not found. Effects of thermal disorder are important in realistic conjugated polymers. Our results show that disorder in backbone chains of P3HT has strong effect on the electronic structure and leads to the localization of the wave functions of the highest states in the valence band, similar to the ones that occur in amorphous polymers. At the interfaces between two materials in organic electronic devices, effects of spontaneous polarization in one or both of them on electronic properties can be pronounced. We show that ordered P3HT exhibits spontaneous polarization along the backbone direction, which is caused by the lack of inversion symmetry due to head-to-tail side chains arrangement. We additionally show that spontaneous polarization in ordered P3HT keeps significant values even at room temperature when the effects of thermal disorder are important.

Keywords: organic semiconductors, electronic structure, domain interface, thermal disorder, crystalline domain, amorphous domain, spontaneous polarization
Scientific field: Electrical and Computer Engineering
Research area: Nanoelectronics and Photonics
UDC number: 621.3

Apstrakt

Cilj ove disertacije da je pruži vezu između atomske i elektronske strukture različitih tipova granica između domena u organskim poluprovodnicima. U polikristalnim organskim poluprovodnicima na bazi malih molekula granica se formira između homogenih kristalnih domena. Ustanovili smo da granica u polikristalnom naftalinu dovodi do pojave stanja zamki u energijskom procepu materijala, lokalizovanih na parovima molekula sa različitih strana granice između kojih je rastojanje malo. Energije stanja zamki su strogo korelisane sa rastojanjem između molekula. Realistični konjugovani polimeri, kao što je poli(3-heksiltiofen) (P3HT), sadrže izmešane kristalne i amorfne domene. Utvrdili smo da HOMO stanja granice između kristalnog i amorfnog dela pripadaju kristalnom domenu. Stanja koja pripaduju i kristalnom i amorfnom domenu i stanja zamki se ne formiraju. Efekti termalne neuređenosti su značajni u realnim konjugovanim polimerima. Naši rezultati pokazuju da neuređenost glavnih lanaca u P3HT ima jak uticaj na elektronsku strukturu i dovodi do lokalizacije talasnih funkcija najviših stanja u valentnoj zoni, slično kao u amorfnim polimerima. Na granici dva materijala u organskim elektronskim napravama, efekti spontane polarizacije u jednom ili oba materijala na elektronska svojstva mogu biti značajni. Utvrdili smo da uređeni P3HT iskazuje spontanu polarizaciju duž glavnog lanca usled nedostatka simetrije na prostornu inverziju zbog glava-rep rasporeda bočnih lanaca. Pokazali smo i da spontana polarizacija u P3HT ima značajne vrednosti čak i na sobnoj temperaturi kada su efekti termalne neuređenosti značajni.

Ključne reči: organski poluprovodnici, elektronska struktura, granica domena, termalna neuređenost, kristalni domen, amorfni domen, spontana polarizacija
Naučna oblast: Elektrotehnika i računarstvo
Oblast istraživanja: Nanoelektronika i fotonika
UDK broj: 621.3

Contents

Chapter 1

Introduction to organic semiconductors

1.1 General information about organic semiconductors

Organic semiconductors are materials that gained a lot of interest in last decades due to their applications in electronic devices, such as organic field-effect transistors (OFET), organic light emitting diodes (OLED) and organic solar cells (OSC) [1–6]. Their advantage over inorganic counterparts is that they are flexible and have low processing cost. However, devices made of organic semiconductors still have relatively low charge mobility and low efficiency. Organic semiconductors are mostly composed of carbon atoms and hydrocarbon groups. They can be divided into two main categories: (1) small-molecule organic semiconductors and (2) conjugated polymers. Some common organic semiconductors are shown in Fig. 1.1.

Small-molecule based crystalline organic semiconductors (such as pentacene and rubrene) exhibit the highest mobilities among organic semiconductors that are on the order of $10^2\ cm^2\ V^{-1}\ s^{-1}$ [7]. Electronic devices based on these materials are typically obtained using vacuum-evaporation technique [8–13]. More recently, it became possible to use an inexpensive solution processing technique to obtain structures with high degree of crystallinity and good charge transport properties [14–

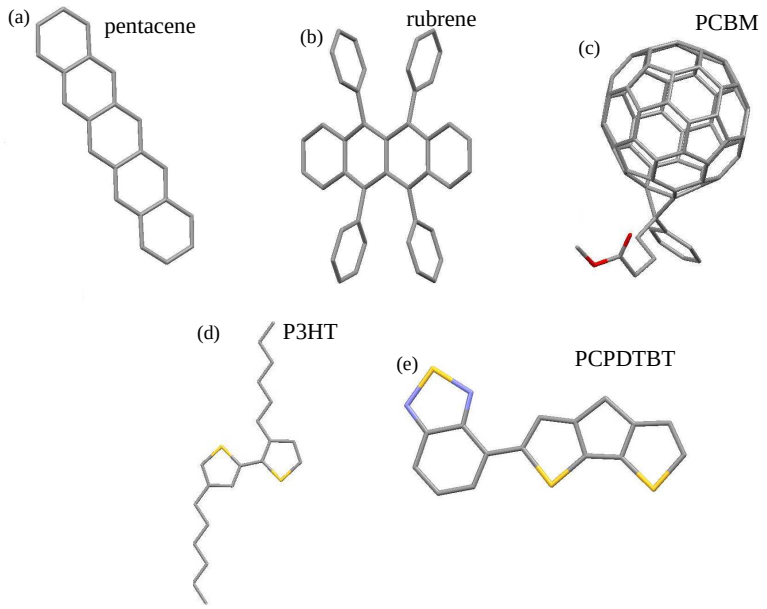

Figure 1.1: Examples of organic semiconductors given by their structural formulas. Molecules in the first row are small-molecule organic semiconductors, while those in the second row are conjugated polymers.

19], which opens the way towards large scale applications. However, highest achieved mobilities of OFETs based on small molecules are still few orders of magnitude below inorganic transistors. OSCs mostly use conjugated polymers as constitutive materials. Currently, the highest reached OSC efficiency is 11.5 %. Besides relatively low efficiency, the main issue that still keeps OSCs away from markets is instability. OLEDs are the most commercialized organic electronic devices which are used for displays and lightnings.

Organic semiconductors not only open possibilities towards low-cost devices, they also contain intriguing physics. The similarity to inorganic semiconductors is the existence of bands and band gap. Band gap in organic semiconductors is defined as difference between the lowest unoccupied molecular orbital (LUMO) and the highest occupied molecular orbital (HOMO). Now, we look in more detail into the structure of organic semiconductors, which are carbon-based materials. Carbon in the ground state has 6 electrons in configuration: $1s^2$, $2s^2$, $2p_x^1$, $2p_y^1$, $2p_z^0$, which means that 2 electrons populate 1s orbital, 2 electrons populate 2s orbital etc. When carbon

atoms approach their binding partners (other carbon atoms, hydrogen atoms...) they form hybrid σ and π orbitals which correspond to chemical bonds. These orbitals determine electronic and optical properties of the material. To show how molecular states are formed, we use ethylene molecule (C_2H_4) as example. Ethylene hybrid orbitals are shown in Fig. 1.2. Two π orbitals form HOMO (bonding) and LUMO (antibonding) states, as shown in Fig. 1.3.

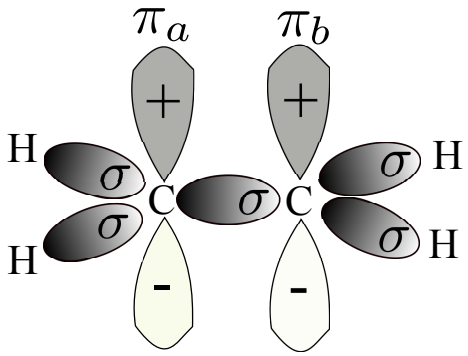

Figure 1.2: Hybrid orbitals of ethylene molecule.

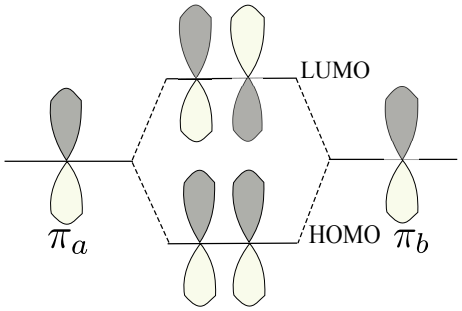

Figure 1.3: HOMO and LUMO states formation in ethylene.

1.2 Interfaces in organic semiconductors

In order to improve electronic properties of organic semiconductors, researchers put effort to understand processes that occur at the atomic level. Understanding of electronic processes that occur at the interfaces in organic semiconductors is crucial issue that has to be properly addressed. Generally speaking, there are there main interface types in organic semiconductors:

(1) Interface between different crystalline grains in the same material.

(2) Interface between ordered (crystalline) and disordered (amorphous) phases of the same material.

(3) Interface between different materials.

In realistic polycrystalline small-molecule organic semiconductors there are crystalline grains with different crystalographic orientations, as sketched in Fig. 1.4. The detailed structure of interfaces between grains is not yet well understood. At the interface periodicity of crystals is broken. The interface can be either sharp or disordered with amorphous region between two crystalline grains. Molecules can exhibit both stronger or weaker electronic coupling than in single crystal. Experimental measurements show existence of trap states that are attributed to grain boundaries [11]. However, the origin of trap states is not clarified. Trap states can originate from the higher electronic coupling that occurs at the boundary [20] (Fig. 1.5 a). On the other hand, there are suggestions that charges are trapped by grains and grain boundary acts as barrier [21] (Fig. 1.5 b), which is satisfied if electronic coupling at the boundary is lower that in single crystal (which is true if there is significantly long void between grains). Commonly used model is that grain boundary act as depletion area, which shifts the levels near the boundary toward higher energies [12]. In this case, boundary acts as trap for holes and barrier for electrons (Fig. 1.5c). Levels at the boundary can be also shifted in the opposite direction, toward lower energies (Fig. 1.5d). While there is no consensus on the electronic structure of grain boundaries in organic semiconductors, it is clear that grain boundaries disrupt charge mobility [9, 11]. Realistic description of grain boundaries is probably a combination of effects shown in Fig. 1.5, where the domination of one effect depends on the molecule type and the processing procedure of the samples.

The second interface type that occurs in organic semiconductors is the interface between ordered and disorder phase of the same material. While this interface type takes place both in small molecules and conjugated polymers, we focus on conjugated polymers. Realistic conjugated polymers are found to be complex with interlaced crystalline and amorphous domains, as shown in Fig. 1.6. It is believed that chains mostly belong to both domains [22, 23]. There are three types of such chains:

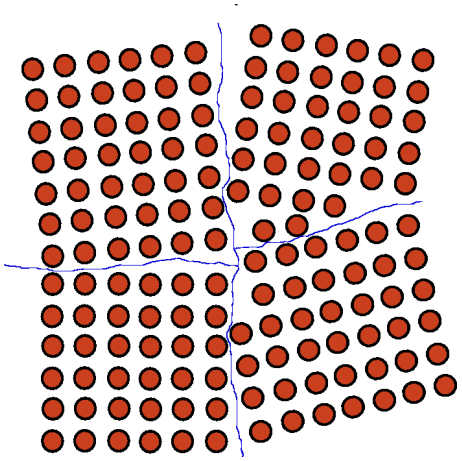

Figure 1.4: Sketch of a polycrystalline small-molecule material.

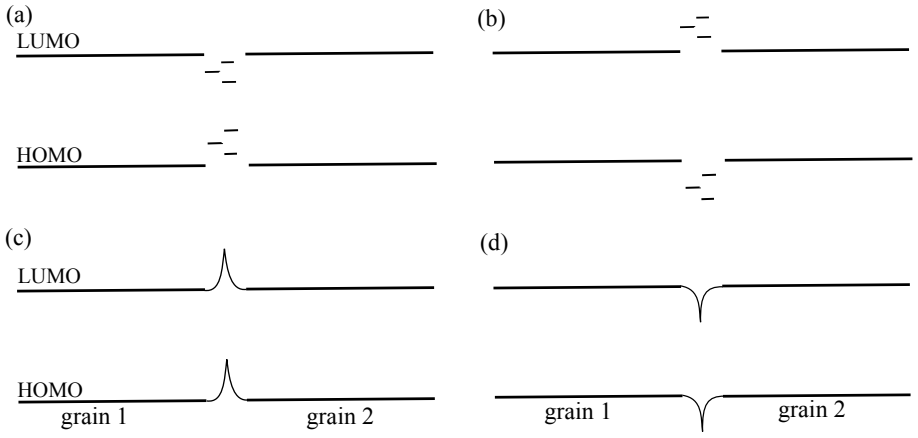

Figure 1.5: Schematic descriptions of a grain boundary in small-molecule organic semiconductors: (a) trap for electrons and holes; (b) barrier for electron and holes; (c) trap for holes, barrier for electrons and (d) barrier for holes and trap for electrons.

(1) bridge chains, which connect different crystalline domains through amorphous domain, (2) folded chains, which connect different parts of the same crystalline domain and (3) extended chains, which extend from crystalline domain and have end in amorphous domain. The knowledge of electronic structure of the interface between crystalline and amorphous domain is based on the calculations of single domains, which show that crystalline conjugated polymers have lower band gap than amorphous [22–25]. Therefore, it is intuitive to assume that HOMO and LUMO band offsets are roughly equal to the half of the band gap difference between amorphous and crystalline domain, as shown in Fig. 1.7. By following this picture, amorphous domains present barrier for charge carriers. However, this simple model does not take into account any interaction between crystalline and amorphous domains, which can significantly affect electronic structure at domain edges. Therefore, to properly investigate electronic structure of the interface between crystalline and amorphous domains, calculations that include both domains are needed.

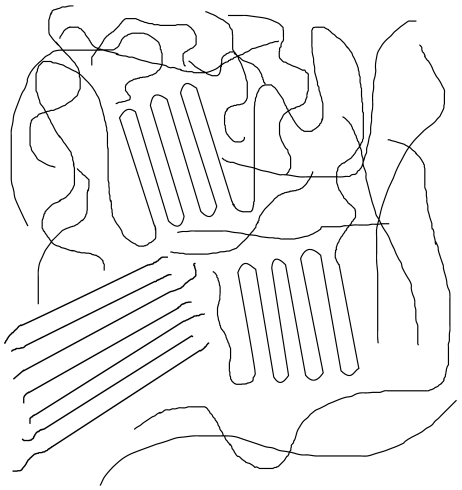

Figure 1.6: Sketch of a realistic conjugated polymer structure with mixed amorphous and crystalline domains.

Finally, third interface type that exists in organic semiconductors is the interface between different materials. OSCs are mostly produced as heterojunctions of two materials, donor and acceptor, where at least one of the materials is organic. One of the most studied OSC is P3HT/PCBM heterojunction. Charge separation of excitons formed by photon absorption takes place at the interfaces between donor

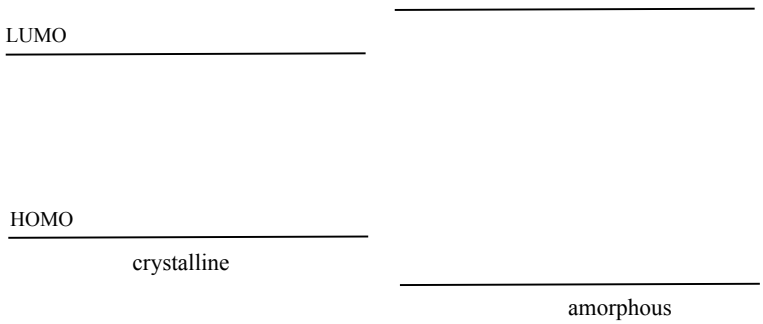

Figure 1.7: Possible electronic level alignment at the interface between crystalline and amorphous domains in conjugated polymers.

and acceptor, as shown in Fig. 1.8. After dissociation at the interface, charges flow independently, which form electric current. Hence, this interface type is important for OSC performance.

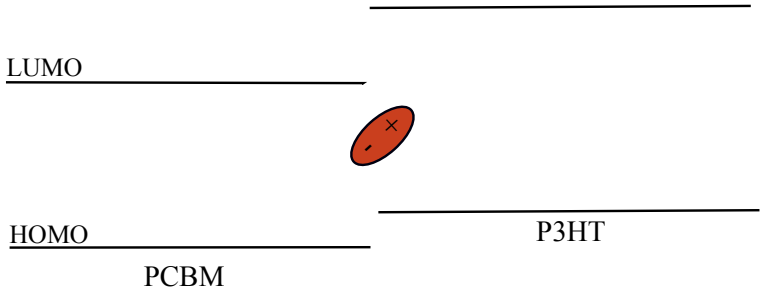

Figure 1.8: Sketch of the interface between P3HT and PCBM.

1.3 Transport in organic semiconductors

To explain transport models used for organic semiocinductors, we start with the most simple representation of an organic semiconductor: one-dimensional array of molecules where each molecule is coupled with its first neighbor. Such representation is given by a purely electronic Hamiltonian:

$$H_{el} = \sum_j \varepsilon_j a_j^\dagger a_j - \tau \sum_j a_j^\dagger a_{j+1}, \tag{1.1}$$

where $a_j^\dagger$ and a_j are the creation and annhilation operators of a charge carrier on site j, ε_j is the site energy and τ is the electronic coupling between sites j and $j+1$.

Electronic coupling in organic semiconductors will be discussed in more detail in the next section. Now we introduce phonons into the model. We assume that molecules have one vibrational degree of freedom which is not coupled with vibrations of the other molecules. Phonons of the one-dimensional system have energy $\hbar\omega_0$. Then, phonon Hamiltonian can be written as:

$$V_{phon} = \sum_j \hbar\omega_0 (b_j^\dagger b_j + \frac{1}{2}), \tag{1.2}$$

where $b_j^\dagger$ and b_j are creation and annhilation operators of phonons. When a charge carrier is present on a site, the site energy is changed along its vibrational mode and its energy is reduced by $\frac{1}{2}\hbar\omega_0 g^2$, where g is the Holstein electron-phonon coupling constant. Instead of Holstein constant, reorganization energy $\lambda = \frac{1}{2}\hbar\omega_0 g^2$ can be used as a measure of the strength of electron-phonon coupling. Hamiltonian that describes local electron-phonon interaction is given by:

$$H_{el-phon}^{local} = \sum_j g\hbar\omega_0 (b_j^\dagger + b_j) a_j^\dagger a_j. \tag{1.3}$$

Here, "local" refers to electron-phonon coupling that arises from modulations of site energies. If electron-phonon coupling arises from modulation of electronic couplings, such electron-phonon coupling is nonlocal, which is now neglected. Finally, total Hamiltonian can be written as:

$$H = H_{el} + H_{phon} + H_{el-phon}^{local}. \tag{1.4}$$

In low temperature limit ($T \rightarrow 0$) charge carrier wavefunctions are delocalized. Charge propagating through the lattice carries with itself a deformation of surrounding molecules. A charge carrier and the corresponding deformation form a polaron. If charge carrier wavefunctions are delocalized, polarons are also delocalized and transport is band-like, as in inorganic semiconductors. Mobility can be calculated by a simple formula:

$$\mu = et_s/m^*, \tag{1.5}$$

where m^* is the effective mass and t_s is the average time between collisions. As temperature increases, charge carrier wavefunctions and polarons become more localized. In the high temperature limit ($k_B T >> \hbar\omega$), charges (and polarons) are

localized on single molecules. Transport is now described as hopping between neighboring molecules. Such transport model is referred as small polaron hopping model, in contrast to polaron band transport model, valid in the low temperature limit. The hopping probability rate is given by:

$$k_{hop} = \frac{\tau^2}{\hbar}(\frac{\pi}{k_B T \lambda})^{1/2} e^{-\lambda/4k_B T}, \tag{1.6}$$

which is in principle the same expression as that given by Marcus formula for charge hopping probability rate. This formula can be also applied in the strong electron-phonon coupling regime, where $\tau << \lambda$. Mobility in the high temperature limit can be roughly calculated by:

$$\mu = \frac{eL^2}{k_B T} k_{hop}, \tag{1.7}$$

where L is the distance between sites. Therefore, transport under small polaron hopping model is thermally activated (mobility increases as temperature incraeses), contrary to polaron band model [1, 7, 26].

Two decribed transport models correspond to two opposite limit cases. It is still not very clear what happens between two limits. Experimental evidences lead to mutually opposite conclusions. In pure organic crystals, mobility was shown to decrease upon the increasing the temperature, which favors the band-like transport [7]. On the other hand, there are experimental evidences that states in organic crystals at the room temperature are localized, which supports hopping transport [7]. Moreover, there are recent results that show that polaronic effect in some organic semiconductors is weak and can be neglected [27]. The criteria for polaron formation is $\tau < \lambda/2$. If this condition is not fulfilled, transport entirely consists of charges.

The transport model described above can be applied for organic crystals where charge transport is limited by dynamic disorder. To describe transport in conjugated polymers, which exhibit significant amount of disorder even in the ordered phase, disorder model is more appropriate [26]. Transport is now described as charge hopping process. In the case of strong electron-phonon coupling and high temperature regimes, Marcus formula given above is often used to calculate hopping rates between the sites. In the case of low temperature and weak electronic coupling regime, Miller-Abrahams formalism is commonly used. Formula for the

Miller-Abrahams hopping rate is given by:

$$k_{ij} = \nu \exp(-2\gamma R_{ij}) \begin{cases} \exp(-\frac{\varepsilon_j - \varepsilon_i}{k_B T}), & \varepsilon_j > \varepsilon_i \\ 1, & \varepsilon_j < \varepsilon_i \end{cases}, \tag{1.8}$$

where ν is the attempt hopping frequency, R_{ij} is the separation between sites i and j and γ is the overlap factor [1, 7, 26].

Expressions for hopping rates and mobilities (with polarons or without) given above can be used only under specific conditions. Even then, their accuracy and applicability is the subject of suspect. Until now, there is no formalism which can entirely describe transport in organic semiconductors.

1.4 Electronic coupling in organic semiconductors

Electronic properties of an organic semiconductor are strongly affected by the modulation of electronic couplings between molecules (or monomers) and site energies of molecules (or monomers). Such modulation takes a place in amorphous domains, near interfaces or as a consequence of thermal disorder. To explain the effects of electronic coupling on the electronic structure, we consider a simple system of two organic molecules (dimer). Assume that electronic Hamiltonian of dimer H is represented by a set of orthonormal molecular orbitals φ_i. Site energies ε_i and couplings τ_{ij} are calculated by:

$$\varepsilon_i = \langle \varphi_i \mid H \mid \varphi_i \rangle, \tag{1.9}$$

$$\tau_{ij} = \langle \varphi_i \mid H \mid \varphi_j \rangle. \tag{1.10}$$

Energy of dimer splitting ΔE_{12} between HOMO and HOMO - 1 dimer states reads:

$$\Delta E_{12} = \sqrt{(\varepsilon_1 - \varepsilon_2)^2 + 4\tau_{12}^2}. \tag{1.11}$$

As can be seen from the previous equation, energy splitting depends on the difference between molecule site energies and the electronic coupling between them. If the site energies are equal, then electronic coupling can be calculated as a half of the dimer splitting energy. The coupling between molecule HOMOs and the resulting

HOMO state of dimer are schematically described in Fig. 1.9. If the coupling between the states is nonzero dimer HOMO state will be coupled state (belonging to both molecules) and its energy will increase as the coupling between the molecules increases. On the other hand, if $\tau_{12} = 0$, then dimer HOMO will belong to the molecule with higher site energy. Both site energies and electronic couplings are sensitive on molecular mutual arrangement and can be rationalized only if molecules adopt cofacial arrangements [26].

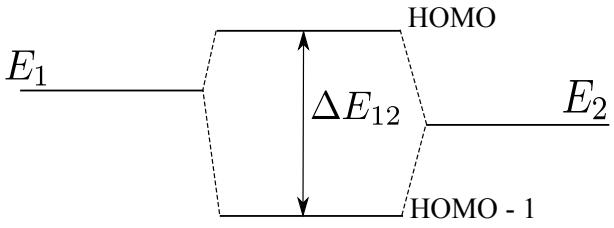

Figure 1.9: The illustration of dimer energy splitting.

1.5 Outline

The thesis is organized as follows. In Chapter 2 the overview of used methods for electronic structure calculations is given. To obtain equilibrium atomic structure, Monte Carlo (MC) method is used, which is explained in detail in Sec. 2.1. The basis for all modern electronic structure calculations is density functional theory (DFT), explained in Sec. 2.2. However, standard DFT approach is not computationally efficient enough to calculate the electronic structure for a large system. Methods used as extension to DFT are summarized in Sec. 2.3-2.6. Finally, modern polarization theory, used to calculate spontaneous polarization in conjugated polymers is explained in Sec. 2.7. In Chapter 3 we investigate the influence of grain boundaries on electronic properties of polycrystalline small-molecule organic semiconductors naphthalene, BTBT and ditBu-BTBT (BTBT with tert-butyl side groups). Based on the results obtained for small grain boundaries, we calculate density of states for bigger boundaries. The effects of thermal disorder on electronic properties of crystalline polymers are investigated in Chapter 4. We consider two different stable

configurations of crystalline P3HT and calculate the density of electronic states and the wave function localization. In Chapter 5, we investigate electronic structure of the interface between crystalline and amorphous P3HT. Two interface types are considered: sharp interface and interface composed of extended chains. Finally, in Chapter 6, we investigate spontaneous polarization in ideally ordered P3HT, thermally disordered P3HT and its effect on electronic structure of the interface between ordered and disordered P3HT.

Chapter 2

Methods for atomic and electronic structure calculations

This chapter is dedicated to the methodology used to calculate atomic and electronic structure of organic semiconductors. Procedure of electronic structure calculations is divided into two main steps (1) generation of equilibrium atomic (molecular) structure and (2) performing electronic structure calculations for obtained atomic structure. Atomic structure can be generated using well-known techniques such as MC simulations or molecular dynamics (MD). In this work MC technique was chosen as method to generate atomic structure because it was shown that MC could reach equillibrium confugraton faster than MD for similar systems [28]. Hence, it will be the subject of detailed explanation in Sec. 2.1. Electronic structure calculations are mostly done using DFT approach. This approach, implemented in many computer codes, is described in Sec. 2.2. However, standard implementations of DFT with plane basis representation do not allow one to calculate electronic structure of a large system (with more than thousand atoms). Methods used in this work which overcome computational limits of DFT, namely the charge patching method (CPM), the folded spectrum method (FSM), the overlapping fragments method (OFM) and density functional tight-binding method (DFTB) are discussed in Sec. 2.3-2.6. Finally, modern polarization theory using Berry phase approach, implemented in many DFT-based computer codes is explained in Sec. 2.7.

2.1 Monte Carlo simulations

Monte Carlo (MC) technique is widely used simulation techniques in science. It was developed by von Neumann, Ulam and Metropolis at the end of the Second World War during the investigation of the diffusion of neutrons in fissionable materials [29]. It has many applications in physics, mathematics, material science, finance etc.

2.1.1 Fundamentals of statistical physics

Firstly, we recall some fundamentals of statistical physics. Let us consider, a macroscopic system, given by coordinates (particle positions and momenta) in multidimensional space that is called phase space. If the system has N particles (which can be atoms, molecules, charges...), the phase space is 6N-dimensional. Having the coordinates in hand, one can observe parameters such as temperature and pressure, while other parameters can be calculated using fundamental equations of thermodynamics. Let us use abbreviation Γ for a particular point in the phase space. Instantaneous value of observed parameter A is denoted by $A(\Gamma)$. As the system evolves in time, it is therefore more reasonable to calculate time average of $A(\Gamma)$, which is given by:

$$A_{obs} = \langle A(\Gamma(t)) \rangle_{time} = \lim_{t_{obs} \to \infty} \frac{1}{t_{obs}} \int_0^{t_{obs}} A(\Gamma(t)) dt. \tag{2.1}$$

Parameters are measured in discrete points in time. If the number of points in time is τ_{obs}, we can rewrite preceding equation in discrete form:

$$A_{obs} = \langle A \rangle_{time} = \frac{1}{\tau_{obs}} \sum_{\tau=1}^{\tau_{obs}} A(\Gamma(\tau)) \tag{2.2}$$

Due to the complexity of time evolution of observed parameters, it is more convenient to use ensemble averages instead of time averages. Ensemble is a set of Γ points in phase space. The distribution of points in the phase space is given by a probability density $\rho(\Gamma)$. Each point represents the system in a particular moment in time. Consequently, density function $\rho(\Gamma)$ evolves in time, as well. If the system is in an equilibrium state given by ρ_{eq}, then $\partial \rho_{eq} / \partial t = 0$. By replacing the time average

with average taken over all members of the ensemble, we have:

$$A_{obs} = \langle A \rangle_{ens} = \sum_{\Gamma} A(\Gamma)\rho_{ens}(\Gamma). \tag{2.3}$$

Sometimes it is more convenient to use weight function $w_{ens}(\Gamma)$ instead of density. It satisfies following equations:

$$\rho_{ens}(\Gamma) = Q_{ens}^{-1} w_{ens}(\Gamma), \tag{2.4}$$

$$Q_{ens} = \sum_{\Gamma} w_{ens}(\Gamma), \tag{2.5}$$

$$\langle A \rangle_{ens} = \frac{\sum_{\Gamma} w_{ens}(\Gamma)A(\Gamma)}{\sum_{\Gamma} w_{ens}(\Gamma)}. \tag{2.6}$$

The weight function is actually non-normalized form of density function with a probability function Q_{ens}, which is a sum over states, serving as normalizing factor. Probability function is a function of the macroscopic properties of the ensemble and it is connected with thermodynamic potential Ψ_{ens} by relation:

$$\Psi_{ens} = -\ln Q_{ens}. \tag{2.7}$$

This function has a minimal value at thermodynamical equilibrium.

In statistical physics there are 4 common ensembles:

(1) microcanonical NVE (constant number of particles N, volume V and energy E) ensemble,

(2) canonical NVT (constant number of particles, volume V and temperature T) ensemble,

(3) isothermal - isobaric constant NPT (constant number of particles, pressure P and temperature) ensemble,

(4) grand canonical ensemble μVT (constant chemical potential μ, volume and temperature) ensemble.

The probability density for the canonical ensemble is proportional to:

$$\exp(-H(\Gamma)/k_B T), \tag{2.8}$$

where $H(\Gamma)$ is the Hamiltonian of the system. Partition function is given by:

$$Q_{NVT} = \sum_{\Gamma} \exp(-H(\Gamma)/k_B T), \tag{2.9}$$

or in quasi-classical form:

$$Q_{NVT} = \frac{1}{N!}\frac{1}{h^{3N}}\int \exp(-H(\mathbf{r},\mathbf{p})/k_BT)d\mathbf{r}d\mathbf{p}. \tag{2.10}$$

Appropriate thermodynamic potential is the Helmholtz free energy A:

$$A/k_BT = \ln Q_{NVT}. \tag{2.11}$$

In the case of the isothermal-isobaric ensemble, probability density is proportional to:

$$\exp(-(H+PV)/k_BT). \tag{2.12}$$

The corresponding partition function is given by:

$$Q_{NPT} = \sum_{\Gamma}\sum_{V} \exp(-(H+PV)/k_BT) = \sum_{V} \exp(-PV/k_BT)Q_{NVT}, \tag{2.13}$$

or in quasi-classical form:

$$Q_{NPT} = \frac{1}{N!}\frac{1}{h^{3N}}\frac{1}{V_0}\int dV \int \exp(-(H+PV)/k_BT)d\mathbf{r}d\mathbf{p}. \tag{2.14}$$

The corresponding thermodynamic function is the Gibbs free energy G:

$$G/k_BT = -\ln Q_{NPT}. \tag{2.15}$$

2.1.2 Thermodynamic properties

Ensembles are mutually equivalent. Therefore, thermodynamic properties of the system can be calculated as averages in any ensemble. Now, we give expressions for some common thermodynamic quantities. Total energy of the system is calculated as a sum of average kinetic and potential energy:

$$E = \langle H \rangle = \langle K \rangle + \langle V_{pot} \rangle . \tag{2.16}$$

Temperature and pressure can be derived from the virial theorem, written in the form:

$$\langle p_k \partial H/\partial p_k \rangle = k_BT, \tag{2.17}$$

$$\langle q_k \partial H/\partial q_k \rangle = k_BT, \tag{2.18}$$

for any coordinate q_k and momentum p_k. In atomic case, momenta appear as squared terms in the Hamiltonian. Hence, we can rewrite that equation in the form:

$$\left\langle \sum_{i=1}^{N} \mid \mathbf{p}_i \mid^2 / m_i \right\rangle = 2 \langle K \rangle = 3Nk_BT, \tag{2.19}$$

from which temperature can be directly calculated. Pressure can be derived as follows. If we choose Cartesian coordinates and use equations of motion, the coordinate derivative that appears in the second virial equations is the negative force $\mathbf{f}_i$ on particle i. Hence, we can write:

$$\frac{1}{3} \left\langle \sum_{i=1}^{N} \mathbf{r}_i \cdot \mathbf{f}_i^{tot} \right\rangle = -Nk_BT. \tag{2.20}$$

Here, expression $\mathbf{f}_i^{tot}$ is used to denote total (external and internal) force. External force is related to the average external pressure P that is applied to a container of volume V by:

$$\frac{1}{3} \left\langle \sum_{i=1}^{N} \mathbf{r}_i \cdot \mathbf{f}_i^{ext} \right\rangle = -PV, \tag{2.21}$$

while internal (interparticle) forces are related to the internal pressure that we call internal virial W:

$$\frac{1}{3} \left\langle \sum_{i=1}^{N} \mathbf{r}_i \cdot \mathbf{f}_i^{int} \right\rangle = W. \tag{2.22}$$

Finally, we can write:

$$PV = Nk_BT + \langle W \rangle . \tag{2.23}$$

It may be useful to write W in a more compact form which will be done by writing $\mathbf{f}_i^{int}$ as the sum of forces $\mathbf{f}_i^{int}$ on particle i from particle j:

$$\sum_i \mathbf{r}_i \mathbf{f}_i^{int} = \sum_i \sum_{j \neq i} \mathbf{r}_i \mathbf{f}_{ij} = \frac{1}{2} \sum_i \sum_{j \neq i} (\mathbf{r}_i \mathbf{f}_{ij} + \mathbf{r}_j \mathbf{f}_{ji}). \tag{2.24}$$

Now we exploit Newton's third law $\mathbf{f}_{ij} = -\mathbf{f}_{ji}$ to switch indices:

$$\begin{aligned} \sum_i \mathbf{r}_i \cdot \mathbf{f}_i^{int} = \frac{1}{2} \sum_i \sum_{i \neq j} \mathbf{r}_{ij} \cdot \mathbf{f}_{ij} = \sum_i \sum_{j>i} \mathbf{r}_{ij} \cdot \mathbf{f}_{ij} = \\ = \sum_i \sum_{j>i} \mathbf{r}_{ij} \cdot \nabla_{\mathbf{r}_{ij}} v(\mathbf{r}_{ij}) = -\sum_i \sum_{j>i} w(r_{ij}), \end{aligned} \tag{2.25}$$

where $\mathbf{r}_{ij} = \mathbf{r}_i - \mathbf{r}_j$ and $w(r)$ is interparticle pair virial function. Now, virial term can be written as:

$$W = -\frac{1}{3}\sum_i \sum_{j>i} w(r_{ij}). \tag{2.26}$$

Fluctuations of observed variables are important as they are related to some thermodynamic properties. Root-mean-square deviation of the observed variable A is defined as:

$$\sigma^2(A) = \left\langle \delta A^2 \right\rangle_{ens} = \left\langle A^2 \right\rangle_{ens} - \left\langle A \right\rangle_{ens}^2 , \tag{2.27}$$

where $\delta A = A - \left\langle A \right\rangle_{ens}$. Now, let us assume canonical ensemble. Specific heat C_V is given by fluctuation in the total energy:

$$\left\langle \delta H^2 \right\rangle_{NVT} = k_B T^2 C_V \tag{2.28}$$

Cross-correlation of potential energy and virial fluctuations gives the expression for the thermal pressure coefficient γ_V:

$$\left\langle \delta V \delta W \right\rangle_{NVT} = k_B T^2 (V\gamma_V - N k_B). \tag{2.29}$$

In the isothermal-isobaric ensemble volume and energy fluctuations may occur. Volume fluctuations are related to the isothermal compessibility β_T:

$$\left\langle \delta V^2 \right\rangle_{NPT} = V k_B T \beta_T. \tag{2.30}$$

Thermally expansion coefficient α_P can be calculated from the cross-correlation of the enthalpy $H + PV$ and volume:

$$\left\langle \delta V \delta (H + PV) \right\rangle_{NPT} = k_B T^2 V \alpha_P. \tag{2.31}$$

2.1.3 Structural properties

The simulated structure can be charaterized by several structural quantities. The most common one is the pair distribution function $g(\mathbf{r}_i, \mathbf{r}_j)$ or $g(r_{ij})$. It is defined by the probability that pair of atoms is found to have mutual distance r_{ij} relative to the probability expected for completely random pair distribution at the same density. This quantity is a good measure of the system ordering and can be used to

distinguish between crystalline and amorphous phase of solids. The expression for the pair distribution function is given by:

$$g(r) = \frac{V}{N^2} \left\langle \sum_i \sum_{j \neq i} \delta(\mid \mathbf{r} \mid - \mid \mathbf{r}_{ij} \mid) \right\rangle . \tag{2.32}$$

The other structural quantity of interest is the spatial Fourier transform of the number density, given by:

$$\rho(k) = \sum_{i=1}^{N} \exp(i\mathbf{k} \cdot \mathbf{r}_i), \tag{2.33}$$

with $\mathbf{k} = (2\pi/L)(k_x, k_y, k_z)$, where L is the length of the box and k_x, k_y and k_z are integers. This quantity is related to the structure factor $S(k)$:

$$S(k) = N^{-1} \langle \rho(k)\rho(-k) \rangle , \tag{2.34}$$

which can be experimentally measured [29, 30].

2.1.4 Basic example of MC technique

Now, we can get back to MC simulations. Firstly, let us have a look at simple example that illustrates the MC technique. The most common illustration of MC technique is the evaluation of the number π. The value of π is equal to the surface of the circle with unit radius, shown in Fig. 2.1. Trial shots are generated within square OABC. At each trial, two random number between 0 and 1 are chosen. These number represent coordinates of the chosen point. Then, distance between the chosen point and the center of the circle (and square) is calculated. If the distance is smaller or equal 1, then point belongs to the shaded area and trail is counted as hit. Otherwise, it is counted as miss. If the total number of trials is N_{trial} and total number of hits is N_{hits}, then:

$$\pi \approx \frac{4 \times P(OCA)}{P(OABC)} = \frac{4N_{hits}}{N_{trial}}. \tag{2.35}$$

The value of π is closer to the exact value as the number of trials increases.

2.1.5 Metropolis algorithm

This example has illustrated the main idea of MC technique that some variable can be calculated from random configuration after sufficient number of trials. Let us

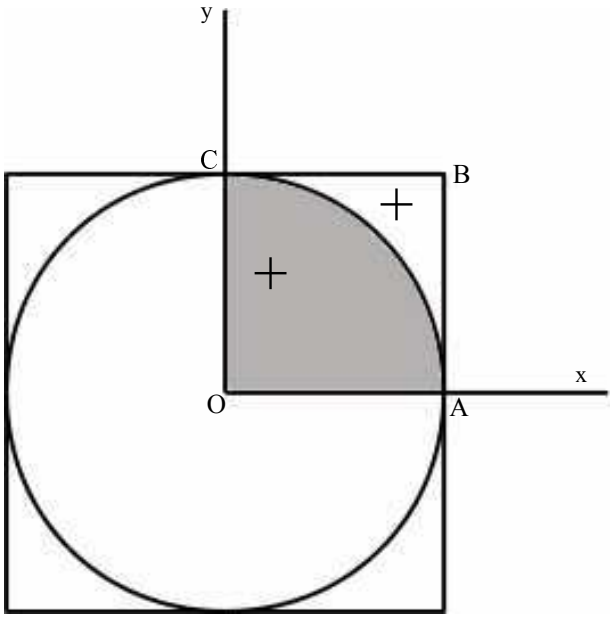

Figure 2.1: The illustration of the evaluation of the number π by hit and miss approach. The figure is taken from Ref. 30.

consider canonical ensemble and property A that has to be evaluated. Therefore, we want to calculate:

$$\langle A \rangle_{NVT} = \int d\Gamma \rho_{NVT}(\Gamma) A(\Gamma). \tag{2.36}$$

Metropolis algorithm requires the sequence of random states (trials) where each state occurs with appropriate probability. Such sequence is called Markov chain and its satisfies two conditions:

(1) Each state belongs to a finite set of states $\Gamma_1, \Gamma_2, ..., \Gamma_n$ that is called state space,

(2) Each state is dependent only on the preceding state.

Two neighboring states Γ_m and Γ_n are connected with a transition probability π_{mn} which is the probability of moving from state m to state n. Let $\rho(i)$ be the probability that system is in state i. This probability is proportional to the Boltzmann factor $\exp(-H(i)/k_BT)$. In equilibrium, the average number of moves from state m to state n should be equal to the number of reverse moves. This statement is expressed by the detailed balance condition:

$$\rho_m \pi_{mn} = \rho_n \pi_{nm}. \tag{2.37}$$

Many possible transition matrices π_{mn} satisfy the previous equation. MC simulation uses Metropolis algorithm to calculate the transition matrix. Probability π_{mn} can be decomposed into two probabilities: (1) probability of performing the trial move from m to n, denoted by $\alpha(m \to n)$ and (2) probability that trial move is accepted, denoted by $p(m \to n)$. Therefore, we can write:

$$\pi_{mn} = \alpha(m \to n) \times p(m \to n) \tag{2.38}$$

In the original Metropolis scheme, matrix α is chosen to by symmetric: $\alpha(m \to n) = \alpha(n \to m)$. If we insert this condition into the detailed balance condition, we obtain:

$$\rho(m)p(m \to n) = \rho(n)p(n \to m) \tag{2.39}$$

and

$$\frac{p(m \to n)}{p(n \to m)} = \frac{\rho(n)}{\rho(m)} = \exp(-\frac{H(n) - H(m)}{k_B T}). \tag{2.40}$$

There is the apparent condition that probabilities $p(m \to n)$ and $p(n \to m)$ should not exceed 1. Metropolis algorithm in the final form is given by:

$$p(m \to n) = \begin{cases} \frac{\rho(n)}{\rho(m)} = e^{-(H(n)-H(m))/k_B T}, & H(n) > H(m) \\ 1, & H(n) \leq H(m) \end{cases} \tag{2.41}$$

As noticed previously, there are other possible solutions, but Metropolis algorithm was shown to give better sampling of the phase space than other solutions. Metropolis algorithm accepts new state n unconditionally if its energy is lower than the energy of the previous state m. Otherwise, new state is accepted with a probability equal to the Boltzmann weights ratio of states n and m. In practice, ratio of the Boltzmann weights is compared with a random chosen number between 0 and 1. If the number is lower than the ratio, trial move is accepted, otherwise it is rejected.

Metropolis condition given above assumes NVT ensemble. In the case of NPT ensemble, the condition should be modified. Instead of calculating only energy difference, we now include volume change. We calculate Δ given by:

$$\Delta = \frac{1}{k_B T}\left[H(f) - H(i) + P(V(f) - V(i)) - N \ln \frac{V(f)}{V(i)}\right], \tag{2.42}$$

where $V(f)$ and $V(i)$ are volumes of the final and the initial state, respectively. Again, if Δ is negative, new configuration is accepted, otherwise, it is accepted with a probability equal to $\exp(-\Delta)$ [29, 30].

The schematic description of the MC algorithm is given in Fig. 2.2. We assume system which consists of N molecules. The algorithms starts with an initial configuration, which can be either random or lattice structure. Random initial configuration is appropriate choice for amorphous structure simulation. On the other hand, if one wants to simulate ordered structure, the initial structure given by lattice is more appropriate choice. The MC algorithm is repeated T times, where T is the number of MC steps. In each MC step, energy of the present system configuration is calculated. Then, a random molecule is chosen, which is afterwards translated and rotated by a random vector. In such a way the new configuration of the system is obtained. The energy of the new system configuration is calculated and Metropolis condition is applied to decide whether the new configuration is accepted or not. The number of MC steps should be large enough to ensure that the system has reached the thermodynamic equilibrium. The saturation of the total energy of the system is the most common indicator that system is in the equilibrium.

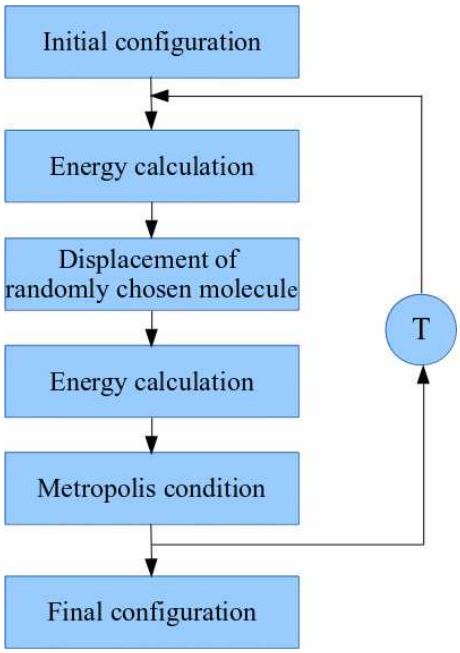

Figure 2.2: The schematic description of the MC algorithm.

2.1.6 Technical aspects of MC simulations

In this subsection we discuss on some technical aspects of MC simulation such as energy calculation and problem of finite size simulation box. Energy of molecular system is calculated using classical force fields. Generally, there are two different types of interactions in molecular systems: (1) short-range interactions and (2) long-range interactions. Short-range interactions describe interactions between pairs, triples and dihedrals of neighboring atoms of the same molecule. On the other hand, long-range interactions describe interactions between non-bonded pairs of atoms. Two atoms are non-bonded if they belong to different molecules or if there are at least four bonds apart in the case they belong to the same molecule. Potential of the interaction between two neighboring atoms i and j is calculated as:

$$E_{ij} = K_r(r - r_0)^2, \tag{2.43}$$

where K_r is a coefficient that depends on the atom types and r and r_0 are instantaneous and equilibrium distance between atoms, respectively. Potential of the interaction between atoms i, j and k that form a triplet of the neighboring atoms is given by:

$$E_{ijk} = k_\theta(\theta - \theta_0)^2, \tag{2.44}$$

where k_θ is a coefficient that depend on the atom types and θ and θ_0 are instantaneous and equilibrium angle formed by the atoms, respectively. Potential of a dihedral that form neighboring atoms i, j, k and l is usually given in the form:

$$E_{ijkl} = \frac{V_1}{2}(1+\cos(\varphi+\varphi_1))+\frac{V_2}{2}(1+\cos(\varphi+\varphi_2))+\frac{V_3}{2}(1+\cos(\varphi+\varphi_3))+\frac{V_4}{2}(1+\cos(\varphi+\varphi_4)), \tag{2.45}$$

where V_1, V_2, V_3 and V_4 are coefficients that depend on the atom type, φ is the dihedral angle and φ_1, φ_2, φ_3 and φ_4 are phase angle that also depend on the atom type. All components of short-range potentials are intramolecular potentials. Most small molecules can be regarded as rigid molecules and interatomic bonds, angles and dihedrals within such molecules remain constant during the simulation. Consequently, corresponding potential terms are constant and do not affect the energy difference. Therefore, for rigid molecules, calculations of short-range interactions

can be avoided, which saves a lot of computation time. Long-range interaction is given as a sum of Van der Waals non-bonding potential and Coulomb potential. Van der Waals potential between non-bonding atoms i and j is commonly given by Lennard-Jones (LJ) potential:

$$v_{LJ} = 4\varepsilon_{ij}((\frac{\sigma_{ij}}{r_{ij}})^{12} - (\frac{\sigma_{ij}}{r_{ij}})^{6}), \tag{2.46}$$

where r_{ij} is the distance between atoms and σ_{ij} and ε_{ij} are LJ parameters. This potential is extensively used in molecular simulations. Hence, it will be examined in more detail. The typical LJ potential shape is given in Fig. 2.3. The potential contains strong repulsive part, which is dominant at low distances and weak attractive part which is dominant at higher distances. The minimum of the potential is at $(2^{1/6}\sigma, -\varepsilon)$, while the zero value is obtained at $r = \sigma$. As can be seen in Fig. 2.3, potential has very large values at low distances. Therefore, it is convenient to set minimal distance between atoms that can occur in the simulation. Usually, this minimal distance is set to be between 0.7σ and 0.9σ. Additionally, one can notice that potential converges to 0 at higher distances. Hence, potential cut-off distance r_C can be introduced and potential can be neglected at distances higher than r_C, which is computationally efficient. Cut-off distance usually takes values from 2.5σ to 4σ. Values for σ and ε are given for particular atoms or atom groups. To calculate these parameters for the interaction between different atoms or groups, combination rules have to be applied. Combination rules for atoms A and B according to OPLS force filed [31] are given by $\sigma_{AB} = \sqrt{\sigma_A \sigma_B}$ and $\varepsilon_{AB} = \sqrt{\varepsilon_A \varepsilon_B}$. Finally, Coulomb potential defines the interaction between atomic charges q_i and q_j by:

$$E_q = \frac{1}{4\pi\epsilon_0}\frac{q_i q_j}{r_{ij}}, \tag{2.47}$$

where ϵ_0 is the electric permittivity of vacuum.

Simulation boxes used in molecular simulations are finite and their size is usually limited by the amount of available computer resources. On the other hand, the simulations of bulk system are often required. In that case, periodic boundary conditions are applied to extend finite system into infinite bulk system. Periodic boundary conditions replicate the system box in the each of three dimensions. In

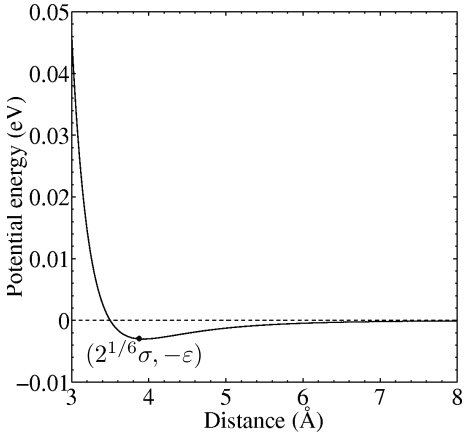

Figure 2.3: The LJ potential between two carbon atoms with values for σ and ε given by OPLS parameter set [31].

such a way, each particle in the original box has its pair in each replicated box, which is illustrated in Fig. 2.4. Particles, denoted by red dots, interact with other particles in the original gray box and in the surrounding boxes within cut-off radius r_c. Here, a distinction between short-range and long-range interactions should be made. In the case of short-range interactions, cut-off radius should be less than a half of the box size to ensure that particle interact with other particles only ones (with original particle or one of its copies, the closest one). This is known as minimum image convention. In the case of long-range interactions, interaction with original particle and all (or most of) copies should be taken into account. In order to make such calculation faster, Ewald summation technique can be applied [29, 30].

2.1.7 MC simulations of molecules

As mentioned, Monte Carlo move involves molecule translation and rotation. Translation occurs in three dimensions, where the molecule center of mass is translated by a random number X between 0 and 1:

$$r_x^{'} = r_x + (2X - 1)\delta r_{max}, \tag{2.48}$$

$$r_y^{'} = r_y + (2X - 1)\delta r_{max}, \tag{2.49}$$

$$r_z^{'} = r_z + (2X - 1)\delta r_{max}, \tag{2.50}$$

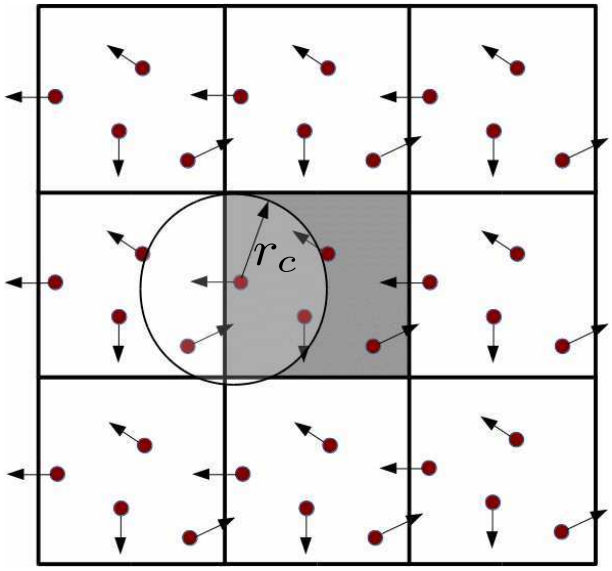

Figure 2.4: The illustration of the periodic boundary condition in two dimensions.

where δr_{max} is a parameter which defines maximal allowed translation along each axis. Rotation of rigid molecules requires three rotation angles to be assigned to a molecule. The most common is to use Euler angles or some similar set of angles. Here, we use Tait-Brian angles Ψ, θ and Φ, defined as in Fig. 2.5. These angles are also known as yaw, pitch and roll angles. The change of angles in each MC step is the same as for translation moves:

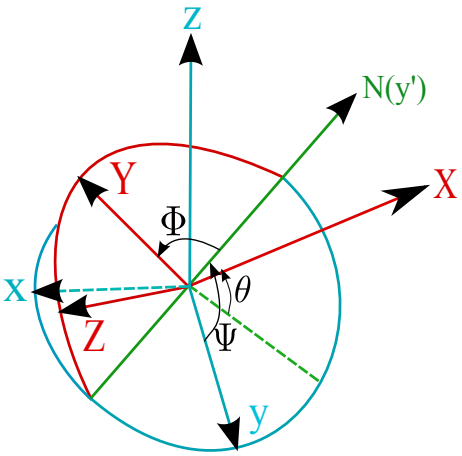

Figure 2.5: The definition of Tait-Brian angles in Cartesian coordinate system.

$$\Psi^{'} = \Psi + (2X - 1)\delta\Psi_{max}, \tag{2.51}$$

$$\theta^{'} = \theta + (2X - 1)\delta\theta_{max}, \tag{2.52}$$

$$\Phi^{'} = \Phi + (2X - 1)\delta\Phi_{max}, \tag{2.53}$$

where $\delta\Psi_{max}$, $\delta\theta_{max}$ and $\delta\Phi_{max}$ are maximal allowed changes in angles. Position of each atom in the molecule can be determined using rotation matrix which multiplies atom position vector. Rotation matrix for Tait-Brian angles is given by:

$$\begin{pmatrix} \cos\Psi\cos\theta & \cos\Psi\sin\theta\sin\Phi - \cos\Phi\sin\Psi & \sin\Psi\sin\Phi + \cos\Psi\cos\Phi\sin\theta \\ \cos\Phi\sin\Psi & \cos\Psi\cos\Phi + \sin\Psi\sin\theta\sin\Phi & \cos\Phi\sin\Psi\sin\theta - \cos\Psi\sin\Phi \\ -\sin\theta & \cos\theta\sin\Phi & \cos\theta\cos\Phi \end{pmatrix}. \tag{2.54}$$

One should note that using rotation angles involves different phase space as that given by Cartesian coordinates. To transform the original phase space (with Cartesian coordinates) into the new phase space (with rotation angles), we should take into account Jacobian of the transformation. Therefore, we have:

$$d\Gamma = \prod_{i=1,..,N} dx_i dy_i dz_i = J \prod_{j=1,..,M} dq_j \prod_{r=1,..,3N-M} dc_r, \tag{2.55}$$

where J is the Jacobian of the transformation, q_j are new coordinates and c_r are constraints which serve as a complement to the overall number of Cartesian coordinates. Jacobian is given by a matrix:

$$J = \begin{bmatrix} \frac{\partial x_1}{\partial q_1} & \cdots & \frac{\partial x_1}{\partial c_{3N-M}} \\ \vdots & \vdots & \vdots \\ \frac{\partial z_N}{\partial q_1} & \cdots & \frac{\partial z_N}{\partial c_{3N-M}} \end{bmatrix}. \tag{2.56}$$

Modified Metropolis condition (assuming NVT ensemble) is given by:

$$p(i \to f) = \min(1, \frac{\mid \det J(f) \mid}{\mid \det J(i) \mid} e^{-\frac{H(f)-H(i)}{k_B T}}), \tag{2.57}$$

where $J(f)$ and $J(i)$ are Jacobians of the final and the initial state. In the case of rigid molecules for which Tait-Brian-Angles angles are used, it is shown that

determinat of the Jacobian has a simple form. It is equal to $-\cos\theta$, with θ defined as in Fig. 2.5.

However, for non-rigid molecules, such as polymers, the calculation of Jacobian transformation can be rather difficult task due to the torsion of dihedrals that is now allowed. To explain the Jacobian transformation for polymers, let us consider a P3HT dimer, shown in Fig. 2.6. Coordinates that are moved during the simulations are: Cartesian coordinates of the center of mass of the left thiophene ring (denoted by x_{CM}, y_{CM}, z_{CM}), three rotation angles (two of them are denoted by α and β) and torsion of dihedrals within alkyl chains and between thiophene rings (denoted by $\varphi_{5,12}$). Bond lengths and bond angles are considered constant during the simulations, therefore, they act as constraints. Finally, coordinates in Cartesian space are given by the atom coordinates. It is usually more convenient to calculate the inverse derivatives. Therefore, we calculate determinant of the inverse Jacobian matrix:

$$J^{-1} = \begin{bmatrix} \frac{\partial q_1}{\partial x_1} & \cdots & \frac{\partial q_1}{\partial z_N} \\ \vdots & \vdots & \vdots \\ \frac{\partial c_{3N-M}}{\partial x_1} & \cdots & \frac{\partial c_{3N-M}}{\partial z_N} \end{bmatrix}. \tag{2.58}$$

Determinant of the original and the inverse Jacobian matrix are mutually reciprocal, i.e. $\det J^{-1} = 1/\det J$.

There are several characteristic types of derivatives that appear in the inverse Jacobian matrix. We will take a example for the each type. The first type are derivatives of the coordinates of the thiophene center of mass with respect to the coordinates of atoms. Coordinates of the center of mass are simply given as the averages of atom coordinates x_i:

$$x_{CM} = \frac{1}{5}\sum_i x_i, \tag{2.59}$$

where the sum runs over the atoms within thiophene ring. Therefore, appropriate derivative reads:

$$\frac{\partial x_{CM}}{\partial x_i} = \frac{1}{5}. \tag{2.60}$$

The second type of derivatives are derivatives of bond lengths with respect to the atomic coordinates. Bond length $\mid r_{ij} \mid$ between atoms i and j is calculated as:

$$\mid r_{ij} \mid = \sqrt{(x_i - x_j)^2 + (y_i - y_j)^2 + (z_i - z_j)^2}. \tag{2.61}$$

Corresponding derivative is given by:

$$\frac{\partial \mid r_{ij} \mid}{\partial x_i} = \frac{(x_i - x_j)}{\mid r_{ij} \mid}. \tag{2.62}$$

Derivatives of the rotation angles with respect to coordinates can be easily obtain by differentiating the rotation matrix given by Eq. 2.54. For example, for derivative of Ψ with respect to x_i, we obtain:

$$\begin{aligned} \frac{\partial \Psi}{\partial x_i} =& (-\sin\Psi\cos\theta Rx_i + (-\sin\Psi\sin\theta\sin\Phi - \cos\Phi\cos\Psi)Ry_i + \\ & (\cos\Psi\sin\Phi - \sin\Psi\cos\Phi\sin\theta)Rz_i)^{-1}, \end{aligned} \tag{2.63}$$

where (Rx_i, Ry_i, Rz_i) are components of the space-fixed vector of an atom i. Now, we calculate the bond angle derivatives with respect to atomic coordinates. Let us consider angle θ_k formed by bonds $\mathbf{r}_{ki}$ and $\mathbf{r}_{kj}$. From definition of a dot product we have:

$$\cos\theta_k = \frac{\mathbf{r}_{ki} \cdot \mathbf{r}_{kj}}{\mid \mathbf{r}_{ki} \mid\mid \mathbf{r}_{kj} \mid} = \frac{(x_i - x_k)(x_j - x_k) + (y_i - y_k)(y_j - y_k) + (z_i - z_k)(z_j - z_k)}{\mid \mathbf{r}_{ki} \mid\mid \mathbf{r}_{kj} \mid}. \tag{2.64}$$

By calculating the derivative of cosine function, we obtain:

$$\frac{\partial \theta_k}{\partial x_i} = \frac{-1}{\sin\theta_k} \frac{((x_j - x_k) \mid \mathbf{r}_{ki} \mid\mid \mathbf{r}_{kj} \mid - \frac{\partial \mid \mathbf{r}_{ki} \mid}{\partial x_i} \mid \mathbf{r}_{kj} \mid \mathbf{r}_{ki} \cdot \mathbf{r}_{kj})}{(\mid \mathbf{r}_{ki} \mid\mid \mathbf{r}_{kj} \mid)^2}. \tag{2.65}$$

Finally, we have to calculate the derivatives of torsion angles of dihedrals with respect to atomic coordinates. Let us assume a dihedral formed by atoms i, j, k and l, where j and k form the central bond of dihedral. Torsion angle can be calculated from a dot product of vectors $\mathbf{n}_{ijk}$ and $\mathbf{n}_{jkl}$ given by:

$$\mathbf{n}_{ijk} = \mathbf{r}_{ij} \times \mathbf{r}_{jk} \tag{2.66}$$

and

$$\mathbf{n}_{jkl} = \mathbf{r}_{jk} \times \mathbf{r}_{kl}. \tag{2.67}$$

Derivative of the torsion angle with respect to coordinates can be calculated using the similar procedure as for bond angles derivatives. Due to the complexity of detailed

formulas, they are omitted. We have now explained how to calculate derivatives that appear in Jacobian for the system of two P3HT monomers. This approach can be extended for a large system by dividing the large system into the subsets of overlapping dimers.

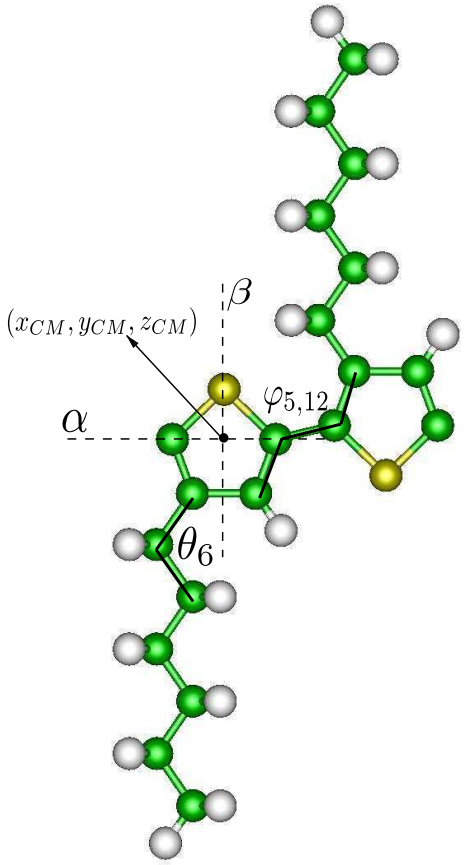

Figure 2.6: Examples of coordinates used in MC simulation of P3HT.

2.2 Density functional theory

Density functional theory (DFT) is widely used approach for electronic structure calculations. It is based on idea that ground state and other properties of a electronic system can be determined from electron density distribution $\rho(\mathbf{r})$. In such a way, N-electron system is replaced by one-electron system.

2.2.1 Hohenberg-Kohn theorems

Hohenberg and Kohn published a work [32] where they described DFT as exact solution to the many-body problem given by Hamiltonian:

$$H = -\frac{\hbar^2}{2m_e}\sum_i \nabla_i^2 + \sum_i V_{ext}(\mathbf{r}_i) + \frac{1}{2}\sum_{i\neq j}\frac{e^2}{\mid \mathbf{r}_i - \mathbf{r}_j \mid}. \tag{2.68}$$

Modern DFT approach is based on two Hohenberg-Kohn theorems which formulations follows.

Theorem 1. *The external potential $V_{ext}(\boldsymbol{r})$ of a system of interacting particles is uniquely defined, except for a constant, by the ground state density $\rho(\boldsymbol{r})$.*

Corollary: *As the external potential fully determines the Hamiltonian of the system, except for a constant energy shift, all properties of the system are determined by the ground state density.*

Proof: Suppose that there are two different external potentials $V_{ext}(\mathbf{r})$ and $V_{ext}(\mathbf{r})^{'}$ which differ by more than a constant and which lead to the same ground density $\rho(\mathbf{r})$. These two different potentials lead to two different wave functions Ψ and $\Psi^{'}$ and two different eigenstates E and $E^{'}$. Since $\Psi^{'}$ is not the ground state for H, then:

$$\begin{aligned} E =& \langle \Psi \mid H \mid \Psi \rangle < \langle \Psi^{'} \mid H \mid \Psi^{'} \rangle = \langle \Psi^{'} \mid H^{'} \mid \Psi^{'} \rangle + \\ & \langle \Psi^{'} \mid H - H^{'} \mid \Psi^{'} \rangle = E^{'} + \int [V_{ext}(\mathbf{r}) - V_{ext}^{'}(\mathbf{r})]\rho(\mathbf{r})d^3\mathbf{r}. \end{aligned} \tag{2.69}$$

Similar inequality is obtained for Ψ, $H^{'}$ and $E^{'}$:

$$E^{'} < E + \int [V_{ext}^{'}(\mathbf{r}) - V_{ext}(\mathbf{r})]\rho(\mathbf{r})d^3\mathbf{r}. \tag{2.70}$$

If we sum up Eq. 2.69 and Eq. 2.70 we obtain $E + E^{'} < E^{'} + E$ which is the contradiction. Therefore, ground density uniquely determines ground state properties of the system.

Theorem 2. *The universal energy functional $E[\rho]$ in the terms of charge density $\rho(\boldsymbol{r})$ can be defined for any external potential $V_{ext}(\boldsymbol{r})$. For a given potential, exact ground state of the system is the minimal value of the functional. The density that minimizes the functional is the exact ground state density.*

Proof: Ground state density determines all properties of the system, including the total energy functional:

$$E[\rho] = T[\rho] + E_{ee}[\rho] + E_{ne} + \int V_{ext}(\mathbf{r})\rho(\mathbf{r})d^3\mathbf{r}, \tag{2.71}$$

where $T[\rho]$ is the kinetic term, $E_{ee}[\rho]$ is the electron-electron interaction term and E_{ne} is the nuclei-electron interaction term. Functional $F[\rho]$ includes all interelectron (kinetic and potential) interaction terms:

$$F[\rho] = T[\rho] + E_{ee}[\rho], \tag{2.72}$$

which is universal for all electronic systems (independent on the external potential) as it is only dependent of the ground state density $\rho(\mathbf{r})$. Let us now assume that ground state density $\rho^{'}(\mathbf{r})$ corresponds to external potential $V^{'}_{ext}(\mathbf{r})$. Total energy functional is equal to the expected value of the Hamiltonian in the ground state with a wavefunction $\Psi^{'}$:

$$E^{'} = E[\rho^{'}] = \langle \Psi^{'} \mid H \mid \Psi^{'} \rangle. \tag{2.73}$$

Now let us consider different ground state density $\rho^{''}(\mathbf{r})$ that leads to wavefunction $\Psi^{''}$. It follows:

$$E^{'} = \langle \Psi^{'} \mid H \mid \Psi^{'} \rangle < \langle \Psi^{''} \mid H \mid \Psi^{''} \rangle = E^{''}. \tag{2.74}$$

Therefore, the energy given by the functional Eq. 2.71 for the ground density $\rho^{'}(\mathbf{r})$ is the minimal energy. If one knows the functional $F[\rho]$, then the ground state and density can be obtained by minimizing the total energy functional [32–36]. The ground state charge density $\rho^{'}(\mathbf{r})$ should satisfy the variational principle given by:

$$\delta E[\rho^{'}] - \mu(\int \rho^{'}(\mathbf{r})d\mathbf{r} - N) = 0. \tag{2.75}$$

where $N = \int \rho^{'}(\mathbf{r})d\mathbf{r}$ and μ is the chemical potential. This leads to the Euler-Lagrange equation:

$$\mu = \frac{\delta E[\rho^{'}]}{\delta \rho^{'}(\mathbf{r})}. \tag{2.76}$$

2.2.2 Kohn-Sham equations

As explained in the previous section, ground state of the system minimizes the energy functional $E[\rho]$ and satisfies the Euler-Lagrange equation. First models used to obtain charge density were based on the explicit forms of $T[\rho]$ and $E_{ee}[\rho]$ functionals. Kohn and Sham introduced orbitals into the model in such a way that kinetic term can be calculated with good accuracy. Let us start with a exact formula for the kinetic term:

$$T = \sum_{i}^{N} n_i \langle \Psi_i \mid -\frac{1}{2}\nabla^2 \mid \Psi_i \rangle, \tag{2.77}$$

where Ψ_i and n_i are natural spin orbitals and their occupation numbers, respectively. According to the Pauli principle, $0 \leq n_i \leq 1$. Additionally:

$$\rho(\mathbf{r}) = \sum_{i}^{N} n_i \sum_{s} \mid \Psi(\mathbf{r}, s) \mid^2 . \tag{2.78}$$

For the given interacting system there can be infinite number of solutions to the last two equations. Kohn and Sham proposed simplified equations given by:

$$T_s[\rho] = \sum_{i}^{N} \langle \Psi_i \mid -\frac{1}{2}\nabla^2 \mid \Psi_i \rangle \tag{2.79}$$

and

$$\rho(\mathbf{r}) = \sum_{i}^{N} \sum_{s} \mid \Psi(\mathbf{r}, s) \mid^2 . \tag{2.80}$$

These two equations are the special cases of Eq. 2.77 and 2.78 for $n_i = 1$ for the first N orbitals and $n_i = 0$ for the other orbitals. Kohn and Sham proposed non-interacting reference system with a Hamiltonian:

$$H_s = \sum_{i}^{N} (-\frac{1}{2}\nabla_i^2) + \sum_{i}^{N} v_s(\mathbf{r}), \tag{2.81}$$

without electron-electron repulsion term. For this Hamiltonian ground state density is exactly ρ. The ground state wave function can be written as:

$$\Psi_s = \frac{1}{\sqrt{N!}} \det[\psi_1 ... \psi_N], \tag{2.82}$$

where ψ_i are first N lowest eigenstates of one-electron Hamiltonian h_s, given by:

$$h_s \psi_i = [-\frac{1}{2}\nabla^2 + v_s(\mathbf{r})]\psi_i = \varepsilon_i \psi_i. \tag{2.83}$$

Let us write interelectron interaction functional $F[\rho]$ in the form:

$$F[\rho] = T_s[\rho] + J[\rho] + E_{xc}[\rho], \tag{2.84}$$

where $J[\rho]$ is the classic part of electron-electron interaction and E_{xc} which contains the difference between exact kinetic term and $T_s[\rho]$ and the non-classical part of electron-electron interaction. Therefore, $E_{xc}[\rho]$ can be written as:

$$E_{xc}[\rho] = T[\rho] - T_s[\rho] + E_{ee}[\rho] - J[\rho]. \tag{2.85}$$

Euler-Lagrange equation now takes the form:

$$\mu = v_s(\mathbf{r}) + \frac{\delta T_s}{\delta \rho(\mathbf{r})}, \tag{2.86}$$

where $v_s(\mathbf{r})$ is the Kohn-Sham potential defined by:

$$v_s(\mathbf{r}) = v(\mathbf{r}) + \frac{\delta J[\rho]}{\delta \rho(\mathbf{r})} + \frac{\delta E_{xc}[\rho]}{\delta \rho(\mathbf{r})} = v(\mathbf{r}) + \int \frac{\rho(\mathbf{r}')}{\mid \mathbf{r} - \mathbf{r}' \mid} d\mathbf{r}' + v_{xc}(\mathbf{r}), \tag{2.87}$$

where $v(\mathbf{r})$ is ionic potential.

Set of Kohn-Sham equations is given by Eq. 2.80, 2.83 and 2.87. As can be seen from the equations, Kohn-Sham potential is dependent on charge density. On the other hand, charge density is dependent on wave functions, solutions to Hamiltonian problem. Hence, Kohn-Sham equations should be solved in a self-consistent manner. The algorithm of Kohn-Sham equations solving starts with a initial guess for charge density. Self-consistent loop begins with effective Kohn-Sham potential calculation followed by one-electron Hamiltonian h_s solving. New charge density is calculated using Eq. 2.80 and compared with old charge density (which is the initial guess in the first iteration of the loop). The loop stops if the difference between the new and the old charge density is smaller than a predefined accuracy. Described algorithm is the basic working principle of DFT calculations [33–37].

2.2.3 Local density approximation

Exchange-correlation term in Kohn-Sham equations is not given in an explicit form. There are several approximations that are used as expression for exchange-correlation

term. The basic one is the local density approximation (LDA). Within LDA, exchange-correlation energy is given by:

$$E_{xc}^{LDA}[\rho] = \int \rho(\mathbf{r})\varepsilon_{xc}(\rho)d\mathbf{r}, \tag{2.88}$$

where ε_{xc} is the exchange-correlation energy of a particle in uniform electron gas at density ρ. Corresponding potential becomes:

$$v_{xc}^{LDA}(\mathbf{r}) = \frac{\delta E_{xc}^{LDA}[\rho]}{\delta\rho(\mathbf{r})} = \varepsilon_{xc}(\rho(\mathbf{r})) + \rho(\mathbf{r})\frac{\delta\varepsilon_{xc}(\rho)}{\delta\rho}. \tag{2.89}$$

Kohn-Sham orbital equation now takes a form:

$$[-\frac{1}{2}\nabla^2 + v(\mathbf{r}) + \int \frac{\rho(\mathbf{r})}{\mid \mathbf{r} - \mathbf{r}' \mid}d\mathbf{r}' + v_{xc}^{LDA}(\mathbf{r})]\psi_i = \varepsilon_i\psi_i. \tag{2.90}$$

Exchange-correlation energy ε_{xc} can be divided into two terms: exchange and correlation terms. Exchange term is given by:

$$\varepsilon_x(\rho) = -C_x\rho(\mathbf{r})^{1/3}, \;\; C_x = \frac{3}{4}(\frac{3}{\pi})^{1/3}, \tag{2.91}$$

while the exact values for the correlation terms are known thanks to the work of Ceperley and Alder [38]. Other widely used expression for exchange-correlation term is generalized gradient approximation (GGA) [29, 33–35].

2.3 Charge patching method

Self-consistent calculation in DFT limits the size of the investigated system to around a thousand atoms due to its computational requirements. In order to calculate electronic structure for a large system, one should look for the alternatives to classical DFT approach. One possibility to make calculation feasible for larger system is to avoid self-consistent calculation. Charge patching method (CPM) [39] is the method which calculates charge densities for a small prototype system and sums them up to obtain charge density for a large system, avoiding self-consistent iterations. The main idea of CPM is the fact that local environment of an atom in a large system is similar to that in a small system. Consequently, atomic contributions to the overall charge density of large system can be extracted from calculations on a small

prototype system. Such contributions are called motifs. Motif charge density that corresponds to atom A at the position $\mathbf{R}_A$ is given by:

$$m_A(\mathbf{r}-\mathbf{R}_A) = \frac{w_A(\mathbf{r}-\mathbf{R}_A)}{\sum_B w_B(\mathbf{r}-\mathbf{R}_B)}\rho(\mathbf{r}). \tag{2.92}$$

where $\rho(\mathbf{r})$ is the charge density obtained by DFT calculations on small prototype system and w is the weight function. Overall charge density is then calculated as a sum of contributions of each atom in the system:

$$\rho_{patch}(\mathbf{r}) = \sum_A m_A(\mathbf{r}-\mathbf{R}_A). \tag{2.93}$$

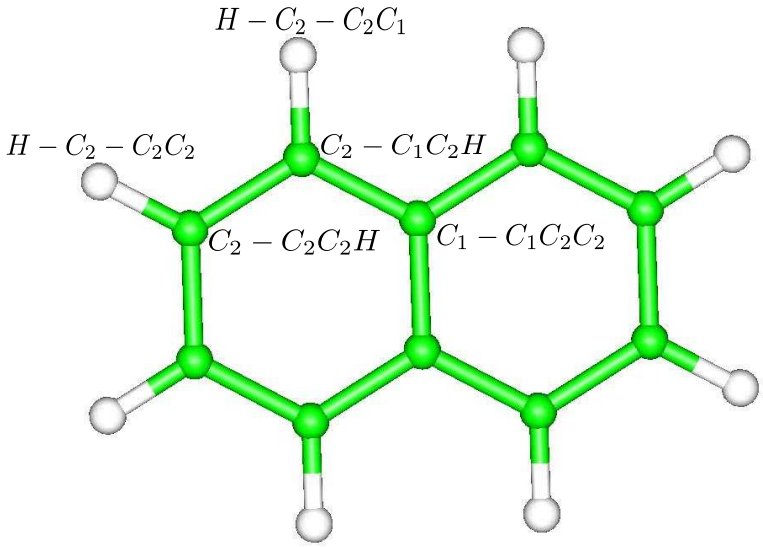

Figure 2.7: Motifs in a naphthalene molecule. C_1 denotes central carbon atoms that are not linked to hydrogen atoms, while C_2 denotes other carbon atoms.

To explain the concept of motifs, we take a single naphthalene molecule, which is the prototype system for simulations of naphthalene. Two atoms have the same motifs if the atoms are the same and their environments (neighboring atoms) are the same. Naphthalene molecule has 5 different motifs: $C_1-C_1C_2C_2$, $C_2-C_1C_2H$, $C_2-C_2C_2H$, $H-C_2-C_1C_2$ and $H-C_2-C_2C_2$, as shown in Fig. 2.7. In the used notation for motifs, first atom is the central and other atoms are neighbors.

CPM allows one to calculate electronic structure for a realistic system without losing much on accuracy. Average error for energies for acene molecules obtained by

CPM are around 10 meV with the reference to DFT. In the case of polythiophene, this error is even smaller (1.6 meV) [39].

2.4 Folded spectrum method

Having the charge density in hand, single particle potential can be constructed and solved. In the case of large number of particles, calculation of all occupied states is inefficient. Electronic and transport properties of semiconducting materials can be determined only with eigenstates in the vicinity of the band gap. Folded spectrum method (FSM) allows one to calculate eigenstates around the given reference energy E_{ref}. FSM replaces original problem (given by $H\Psi = E\Psi$) with the problem:

$$(H - E_{ref})^2\Psi = (E - E_{ref})^2\Psi. \tag{2.94}$$

In this way, energy spectrum from the original problem is folded into the spectrum of the problem given by Eq. 2.94. The lowest energy obtained by FSM is the energy closest to E_{ref}.

2.5 Overlapping fragments method

The important point that directly affects the complexity of electronic structure calculations in the choice of the basis set for wave functions representation. The most simple way, but the most computationally demanding approach is the representation in plane basis set, given by:

$$\Psi_i(\mathbf{r}) = \sum_{\mathbf{k}} c_{i,\mathbf{k}} e^{i\mathbf{k}\cdot\mathbf{r}}, \tag{2.95}$$

where $\mathbf{k}$ is the reciprocal space vector. The alternatives to the representation in plane basis set are representation in localized orbital basis set or approach based on the system division into small fragments. Overlapping fragments method (OFM) [40] combines these two approaches: it divides system into small fragments and uses the eigenvalues of the fragments as the basis set for the whole system. The output of OFM are transfer integrals $H_{ij} = \langle \phi_i^{(m)} \mid H \mid \phi_j^{(n)} \rangle$ and wave function overlaps

$S_{ij} = \langle \phi_i^{(m)} \mid \phi_j^{(n)} \rangle$ between the states $\phi_i^{(m)}$ and $\phi_j^{(n)}$, where $\phi_i^{(m)}$ is the i-th wave function of the fragment m and $\phi_j^{(n)}$ is the j-the wave function of the fragment n. Now, generalized eigenvalue problem can be formulated as:

$$\sum_{mn}(H_{ij,mn} - ES_{ij,mn})C_{mn} = 0. \tag{2.96}$$

OFM is highly suitable for the systems where division into fragments is intuitive, as in conjugated polymers. The illustration of the system division into the fragments is given in Fig. 2.8. To achieve sufficient accuracy, only few states per fragment are needed. Good representation of electronic states is obtained when fragments mutually overlap [40].

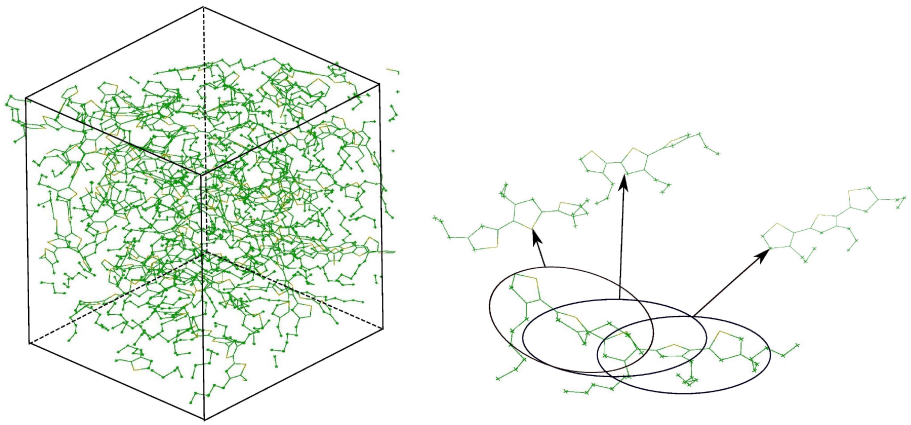

Figure 2.8: Illustration of the system division into the fragments in OFM.

2.6 Density functional tight-binding method

As discussed previously, classical DFT has its limitations due to its large computational cost. In this section we introduce density functional tight-binding method (DFTB). This method uses tight-binded local atomic orbitals as a basis set to represent Kohn-Sham Hamiltonian. It is based on tight-binding approach proposed by Slater and Koster in 1954 [41]. They proposed Hamiltonian expansion into an orthogonalized basis set of atomiclike orbitals. Later, Chadi proposed that energy functional can be written as:

$$E = E_{occ} + E_{rep}, \tag{2.97}$$

where E_{occ} is the sum over occupied orbital energies obtained from Hamiltonian diagonalization and E_{rep} is the short-ranged repulsive two-particle interaction term which contains ionic repulsion and correction to the approximations made in the first term [42].

To explain DFTB in a more formal way, we start from general Kohn-Sham energy functional for a system with M electrons and N nuclei:

$$E[\rho] = \sum_{i}^{occ} \langle \Psi_i \mid -\frac{\Delta}{2} + V_{ext} + \frac{1}{2}\int \frac{\rho(\mathbf{r}')}{\mid \mathbf{r} - \mathbf{r}' \mid} d\mathbf{r}' \mid \Psi_i \rangle + E_{XC}[\rho] + \frac{1}{2}\sum_{\alpha,\beta}^{N} \frac{Z_\alpha Z_\beta}{\mid \mathbf{R}_\alpha - \mathbf{R}_\beta \mid}, \tag{2.98}$$

where $\mathbf{R}_\alpha$ and $\mathbf{R}_\beta$ are positions of nuclei α and β. Let us write charge density as a sum of reference density $\rho_o(\mathbf{r}')$ and small fluctuation $\delta\rho(\mathbf{r}')$. If we substitute this sum into the energy functional, we obtain:

$$\begin{aligned} E = &\sum_{i}^{occ} \langle \Psi_i \mid -\frac{\Delta}{2} + V_{ext} + \int \frac{\rho_0(\mathbf{r}')}{\mid \mathbf{r} - \mathbf{r}' \mid} d\mathbf{r}' d\mathbf{r} + V_{XC}[\rho_0] \mid \Psi_i \rangle - \\ &\frac{1}{2}\int\int \frac{\rho_0(\mathbf{r}')(\rho_0(\mathbf{r}) + \delta\rho(\mathbf{r}))}{\mid \mathbf{r} - \mathbf{r}' \mid} d\mathbf{r}' d\mathbf{r} - \int V_{XC}[\rho_0](\rho_0(\mathbf{r}) + \delta\rho(\mathbf{r}))d\mathbf{r} + \\ &\frac{1}{2}\int\int \frac{\delta\rho(\mathbf{r}')(\rho_0(\mathbf{r}) + \delta\rho(\mathbf{r}))}{\mid \mathbf{r} - \mathbf{r}' \mid} d\mathbf{r}' d\mathbf{r} + E_{XC}[\rho_0 + \delta\rho] + E_{ii}, \end{aligned} \tag{2.99}$$

where E_{ii} is the ion-ion interaction term. The second term is the correction for double counting of Hartree term and the fourth term originates form Hartree term splitting into one related to ρ_0 and one related to $\delta\rho$. By expanding E_{XC} to second order in density fluctuations, we obtain:

$$\begin{aligned} E = &\sum_{i}^{occ} \langle \Psi_i \mid H_0 \mid \Psi_i \rangle - \frac{1}{2}\int\int \frac{\rho_0(\mathbf{r}')\rho_0(\mathbf{r})}{\mid \mathbf{r} - \mathbf{r}' \mid} d\mathbf{r}' d\mathbf{r} + E_{XC}[\rho] - \int V_{XC}[\rho_0]\rho_0 d\mathbf{r} + \\ &E_{ii} + \frac{1}{2}\int\int \left(\frac{1}{\mid \mathbf{r} - \mathbf{r}' \mid} + \frac{\delta^2 E_{XC}}{\delta\rho\delta\rho'} \mid_{\rho_0} \right) \delta\rho\delta\rho' d\mathbf{r}' d\mathbf{r}. \end{aligned} \tag{2.100}$$

One should note that linear terms in $\delta\rho$ have vanished. Hamiltonian H_0 is dependent only on reference charge density $\rho_0(\mathbf{r})$.

2.6.1 Zeroth-order DFTB

Zeroth-order non-self-consistent charge DFTB approach neglects the last term in the energy functional given by Eq. 2.100. In this case, energy functional can be

written as a sum of the part that depends only on input charge density and the repulsion term E_{rep}:

$$E^{TB} = \langle \Psi_i \mid H \mid \Psi_i \rangle + E_{rep}. \tag{2.101}$$

Single particles wave functions Ψ_i are expanded into a set of localized atomic orbitals φ_ν:

$$\Psi_i(\mathbf{r}) = \sum_\nu c^\alpha_{\nu i} \varphi_\nu(\mathbf{r} - \mathbf{R}_\alpha), \tag{2.102}$$

where $c^\alpha_{\nu i}$ are expansion coefficients. Atomic orbitals are given in Slater-type representation [43]. They are determined from a self-consistent LDA calculations on free neutral pseudoatoms. By applying variational principle to Eq. 2.101 we obtain DFTB Kohn-Sham equation, which are afterwards expanded into the set of equations:

$$\sum_\nu^M c_{\nu i}(H_{\mu\nu} - \varepsilon_i S_{\mu\nu}) = 0, \;\; \forall \mu, i, \tag{2.103}$$

where $H_{\mu\nu} = \langle \varphi_\mu \mid H \mid \varphi_\nu \rangle$, $S_{\mu\nu} = \langle \varphi_\mu \mid \varphi_\nu \rangle$ for $\forall \mu \in \alpha$ and $\forall \nu \in \beta$. Hamiltonian $H_{\mu\nu}$ has a form:

$$H_{\mu\nu} = \begin{cases} \varepsilon_\mu^{neutral\ free\ atom}, & \mu = \nu \\ \langle \varphi^\alpha_\mu \mid T + V_\alpha + V_\beta \mid \varphi^\beta_\nu \rangle, & \alpha \neq \beta \\ 0, & otherwise. \end{cases} \tag{2.104}$$

Here, α and β denotes atoms on which wave functions and potentials are centered, while V_α and V_β are atomic potentials. Therefore, only two-center matrix elements are explicitly calculated. As can be seen from the Hamiltonian, eigenvalues of free atoms serve as diagonal elements. By solving the Hamiltonian, Kohn-Sham orbitals ε_i (with occupation number n_i) are obtained, which defines the first term in Eq. 2.101. Second (repulsion) term is calculated as a function of distance by taking the difference between free neutral pseudoatoms energies $E^{SCF}_{LDA}(R)$ and tight-binding energy for a reference system:

$$E_{rep}(R) = E^{SCF}_{LDA}(R) - \sum_i^{occ} n_i \varepsilon_i(R). \tag{2.105}$$

2.6.2 Second-order DFTB

Zeroth-order DFTB gives accurate results when electron density can be approximated as sum of atomic densities. This is the case in homo-nuclear systems, where the charge transfer between atoms is negligible. However, for hetero-nuclear polar molecules the accuracy of the zeroth-order DFTB might not be sufficient. In these cases, second-order term in Eq. 2.100 should be included into the calculations, which defines second-order DFTB.

Firstly, we decompose $\delta\rho(\mathbf{r})$ into atom-centered contributions $\delta\rho_\alpha(\mathbf{r})$ and $\delta\rho_\beta(\mathbf{r}')$ that decay fast with the distance from atom center. Now, second-order term can be written as:

$$E_{2nd} = \frac{1}{2}\sum_{\alpha,\beta}^{N}\int\int\left(\frac{1}{\mid \mathbf{r}-\mathbf{r}' \mid} + \frac{\delta^2 E_{XC}}{\delta\rho_\alpha\delta\rho'_\beta}\mid_{\rho_0}\right)\delta\rho_\alpha\delta\rho'_\beta d\mathbf{r}' d\mathbf{r}. \tag{2.106}$$

Next, $\delta\rho_\alpha(\mathbf{r})$ can be expanded into a series of radial (K_{ml}) and angular (Y_{ml}) functions:

$$\delta\rho_\alpha(\mathbf{r}) = \sum_{lm} K_{ml}F^\alpha_{ml}(\mid \mathbf{r}-\mathbf{R}_\alpha \mid)Y_{lm}(\frac{\mathbf{r}-\mathbf{R}_\alpha}{\mid \mathbf{r}-\mathbf{R}_\alpha \mid}) \approx \Delta q_\alpha F^\alpha_{00}(\mid \mathbf{r}-\mathbf{R}_\alpha \mid)Y_{00}, \tag{2.107}$$

where F^α_{ml} denotes the normalized radial dependence of the density fluctuations on atom α on corresponding angular momentum and Δq_α is an atomic charge which satisfies $\sum_\alpha \Delta q_\alpha = \int \delta\rho(\mathbf{r})d\mathbf{r}$. By substituting Eq. 2.107 into Eq. 2.106 we obtain simplified expression for the second-order term:

$$E_{2nd} = \frac{1}{2}\sum_{\alpha,\beta}^{N}\Delta q_\alpha\Delta q_\beta\gamma_{\alpha,\beta}, \tag{2.108}$$

where:

$$\gamma_{\alpha,\beta} = \int\int\left(\frac{1}{\mid \mathbf{r}-\mathbf{r}' \mid} + \frac{\delta^2 E_{XC}}{\delta\rho_\alpha\delta\rho'_\beta}\mid_{\rho_0}\right)\frac{F^\alpha_{00}(\mid \mathbf{r}-\mathbf{R}_\alpha \mid)F^\beta_{00}(\mid \mathbf{r}'-\mathbf{R}_\beta \mid)}{4\pi}d\mathbf{r}' d\mathbf{r}. \tag{2.109}$$

There are two limiting cases under which expression for second-order term can be simplified: (1) large interatomic distance limit and (2) vanishing interatomic distance limit. In the case of large interatomic distance ($R_{\alpha,\beta} =\mid \mathbf{R}_\alpha - \mathbf{R}_\beta \mid \rightarrow \infty$), exchange-correlation term vanishes and second-order term is given only by Coulomb

interaction between charges Δq_α and Δq_β:

$$E_{2nd} = \frac{1}{2}\sum_{\alpha,\beta}^{N} \frac{\Delta q_\alpha \Delta q_\beta}{R_{\alpha\beta}}. \tag{2.110}$$

On the other hand, when charges are residing on the same atom (($R_{\alpha,\beta} =\mid \mathbf{R}_\alpha - \mathbf{R}_\beta \mid\rightarrow 0$)), rigorous calculation of $\gamma_{\alpha,\beta}$ would require the known charge distribution. Here, a simple approximation to $\gamma_{\alpha\alpha}$ is made: it can be written as a difference of the ionization potential I_α and the electron affinity A_α:

$$\gamma_{\alpha,\alpha} \approx I_\alpha - A_\alpha \approx U_\alpha, \tag{2.111}$$

which can be approximated by the Hubbard parameter U_α. Therefore, $\gamma_{\alpha\beta}$ depends only on the distance between α and β and parameters U_α and U_β.

Now, we want to obtain expression for γ which is valid for all system scales and that is consistent with approximations for two limits discussed above. In accordance with Slater-type orbitals used as the basis set for Kohn-Sham equations, let us assume exponential decay of charge densities:

$$\delta\rho_\alpha(\mathbf{r}) = \frac{\tau_\alpha^3}{8\pi} e^{-\tau_\alpha|\mathbf{r}-\mathbf{R}_\alpha|}. \tag{2.112}$$

Let us neglect for a moment exchange-correlation term in Eq. 2.106. The second-order term now reads:

$$\gamma_{\alpha\beta} = \int\int \frac{1}{\mid \mathbf{r}-\mathbf{r}^{'} \mid} \frac{\tau_\alpha^3}{8\pi} e^{-\tau_\alpha|\mathbf{r}^{'}-\mathbf{R}_\alpha|} \frac{\tau_\beta^3}{8\pi} e^{-\tau_\beta|\mathbf{r}-\mathbf{R}_\beta|} d\mathbf{r}^{'} d\mathbf{r}. \tag{2.113}$$

Integration over $\mathbf{r}^{'}$ leads to:

$$\gamma_{\alpha\beta} = \int \left[\frac{1}{\mid \mathbf{r}-\mathbf{R}_\alpha \mid} - (\frac{\tau_\alpha}{2} + \frac{1}{\mid \mathbf{r}-\mathbf{R}_\alpha \mid}) e^{-\tau_\alpha|\mathbf{r}-\mathbf{R}_\alpha|}\right] \times \frac{\tau_\beta^3}{8\pi} e^{-\tau_\beta|\mathbf{r}-\mathbf{R}_\beta|}. \tag{2.114}$$

After some coordinate transformations (for more detail see Appendix of Ref. 44), we can write $\gamma_{\alpha,\beta}$ in a form:

$$\gamma_{\alpha\beta} = \frac{1}{R} - S(\tau_\alpha, \tau_\beta, R), \tag{2.115}$$

where $R =\mid R_\alpha - R_\beta \mid$ and S is an exponentially decaying short-range function given by:

$$S(\tau_\alpha, \tau_\alpha, R) = \frac{5}{16}\tau_\alpha + \frac{1}{R}, \quad R \rightarrow 0. \tag{2.116}$$

If we take $R \rightarrow 0$, we are residing in the vanishing interatomic distance limit. Consequently, we can approximate $\gamma_{\alpha,\alpha}$ with the Hubbard parameter U_α and we easily obtain:

$$\tau_\alpha = \frac{16}{3} U_\alpha. \tag{2.117}$$

Hubbard parameter can be calculated by self-consistent *ab-initio* approach which includes the second-order exchange-correlation term important for small distances. In high distance limit, exchange-correlation terms vanishes and Coulomb interaction becomes dominant.

Finally, we can write tight-binding energy functional with second-order term as:

$$E^{TB} = \sum_{i}^{occ} \langle \Psi_i \mid H \mid \Psi_i \rangle + \frac{1}{2} \sum_{\alpha,\beta}^{N} \gamma_{\alpha,\beta} + E_{rep}, \tag{2.118}$$

where $\gamma_{\alpha,\beta} = \gamma_{\alpha,\beta}(U_\alpha, U_\beta, \mid \mathbf{R}_\alpha - \mathbf{R}_\beta \mid)$. As in the case of zeroth-order DFTB, Hamiltonian H depends only on the reference charge density $\rho_0(\mathbf{r})$. However, self-consistent procedure is needed to calculate wave functions Ψ_i. Wave functions are expanded into a set of localized atomic orbitals φ_ν with expansion coefficients $c_{\nu i}$. Again, Slater-type atomic orbitals are used, determined by free atom self-consistent LDA calculations. For the charge fluctuations $\Delta q_\alpha = q_\alpha - q_\alpha^0$ calculation, Mulliken charge analysis [45] is apllied. For q_α we obtain:

$$q_\alpha = \frac{1}{2} \sum_{i}^{occ} n_i \sum_{\mu \in \alpha} \sum_{\nu}^{N} (c_{\mu i}^* c_{\nu i} S_{\mu\nu} + c_{\nu i}^* c_{\mu i} S_{\nu\mu}). \tag{2.119}$$

Generalized eigenvalue problem is now formulated as:

$$\sum_{\nu}^{M} (H_{\mu\nu} - \varepsilon_i S_{\mu\nu}) = 0, \quad \forall \mu, i, \tag{2.120}$$

with

$$\begin{aligned} H_{\mu\nu} &= \langle \varphi_\mu \mid H \mid \varphi_\nu \rangle + \frac{1}{2} S_{\mu\nu} \sum_{\xi}^{N} (\gamma_{\alpha\xi} + \gamma_{\beta\xi}) \Delta q_\xi = H_{\mu\nu}^0 + H_{\mu\nu}^1, \\ S_{\mu\nu} &= \langle \varphi_\mu \mid \varphi_\nu \rangle, \quad \forall \mu \in \alpha, \ \nu \in \beta. \end{aligned} \tag{2.121}$$

As in zeroth-order DFTB, repulsive term E_{rep} is calculated by taking the difference between LDA pseudoatom energy and corresponding DFTB electronic energy [43, 44, 46].

2.7 Modern polarization theory

Macroscopic polarization is the key concept in the description of dielectric materials. It quantifies the material response to applied external electric field. Material can possess permanent polarization even in the absence of external electric filed. Such polarization is called spontaneous and materials that have this feature are called pyroelectrics. Ferroelectrics are subgroup of pyroelectrics where spontaneous polarization vector changes its orientation upon the change of electric field vector orientation [47].

Formal definition of polarization was a subject of scientific polemics through decades. First definition, which had been serving for a long time as valid, defines polarization as a dipole moment per unit of volume. Dipole moment d is given by the spatial charge distrubition $\rho(\mathbf{r})$:

$$d = \int \rho(\mathbf{r})\mathbf{r}d\mathbf{r}. \tag{2.122}$$

Then, polarization can be defined as:

$$\mathbf{P} = \frac{1}{\Omega}\int \rho(\mathbf{r})\mathbf{r}d\mathbf{r}, \tag{2.123}$$

where Ω is the unit cell volume. This definition gives the unique value for an isolated system (e.g. isolated molecule). However, in most cases, bulk polarization is the quantity of interest. Polarization calculated by Eq. 2.123 is sensitive to unit cell shift, which leads to polarization indeterminacy. Therefore, definition given by Eq. 2.123 does not apply for bulk polarization.

The new definition of polarization was driven by experimental measurements which often use electric current to determine some property of a material. Instead of using charge distribltion, charge flow (electric current) can be used to calculate polarization difference between two states. This definition is formulated as:

$$\Delta\mathbf{P} = \mathbf{P}(\Delta T) - \mathbf{P}(0) = \int_0^{\Delta T} \mathbf{j}(t)dt, \tag{2.124}$$

where $\mathbf{j}(t)$ is the current density given by fundamental equation:

$$\frac{d\mathbf{P}(t)}{dt} = \mathbf{j}(t). \tag{2.125}$$

Time that appears in Eq. 2.124 can be interpreted as a dimensionless adiabatic time. Hence, we replace t with λ which varies continuously from the initial state 0 to the final state 1. Now, Eq. 2.124 is written in the form:

$$\Delta\mathbf{P} = \int_0^1 d\lambda \frac{d\mathbf{P}}{d\lambda}. \tag{2.126}$$

To explain the meaning of this definition, let us assume an insulator with centrosymmetric unit cell. In the unit cell with the center of inversion symmetry, spontaneous polarization is 0 in each direction [47]. If insulator adopts a new structure that does not possess the center of inversion symmetry, spontaneous polarization of this configuration can be calculated as polarization difference between the new (non-centrosymmeric) and the old (centrosymmetric) structure. This difference is actually the effective spontaneous polarization of the new structure.

The modern polarization theory, based on idea explained above, was founded in the early 1990s by works of Resta [48,49], King-Smith [50,51] and Vanderbilt [50–52]. It known as Berry-phase theory of polarization, as polarization is expressed by the quantum phase known as Berry phase. Now we give the formal description of the modern polarization theory. Let us assume a periodic crystalline system with wave function given by Bloch functions: $\psi_{n\mathbf{k}}(\mathbf{r}) = e^{i\mathbf{k}\cdot\mathbf{r}}u_{n\mathbf{k}}(\mathbf{r})$, where $\mathbf{k}$ is the unit cell vector in the reciprocal space. Eigenvalue problem of the periodic system can be expressed as $H_{\mathbf{k}} \mid u_{n\mathbf{k}}\rangle = E_{n\mathbf{k}} \mid u_{n\mathbf{k}}\rangle$ where:

$$H_{\mathbf{k}} = \frac{(\mathbf{p} + \hbar\mathbf{k})^2}{2m} + V. \tag{2.127}$$

Eigenvalues depend on the parameter λ (introduced in the previous paragraph), which changes slowly in the time. Therefore, we can use first-order perturbation theory to calculate corrections $\delta\psi_{n\mathbf{k}}$:

$$\delta\psi_{n\mathbf{k}} = -i\hbar\frac{d\lambda}{dt}\sum_{m\neq n}\frac{\langle\psi_{m\mathbf{k}} \mid \partial_\lambda\psi_{n\mathbf{k}}\rangle}{E_{n\mathbf{k}} - E_{m\mathbf{k}}} \mid \psi_{m\mathbf{k}}\rangle, \tag{2.128}$$

where ∂_λ is the first derivative with respect to λ. First-order current arising from all n occupied states is given by:

$$\mathbf{j}_n = \frac{d\mathbf{P}_n}{dt} = \frac{i\hbar e\frac{d\lambda}{dt}}{(2\pi)^3 m}\sum_{m\neq n}\int\frac{\langle\psi_{n\mathbf{k}} \mid \mathbf{p} \mid \psi_{m\mathbf{k}}\rangle\langle\psi_{m\mathbf{k}} \mid \partial_\lambda\psi_{n\mathbf{k}}\rangle}{E_{n\mathbf{k}} - E_{m\mathbf{k}}} + c.c. \tag{2.129}$$

where "c.c." stands for complex conjugate. Again, we replace t with λ. After some manipulation, we obtain:

$$\frac{d\mathbf{P}}{d\lambda} = \frac{ie}{(2\pi)^3}\int \langle \nabla_{\mathbf{k}} u_{n\mathbf{k}} \mid \partial_\lambda u_{n\mathbf{k}} \rangle d\mathbf{k} + c.c \tag{2.130}$$

One should note that summation over m unoccupied states has disappeared from the formula as the polarization is a ground-state property. After the integration with respect to λ we obtain:

$$\mathbf{P}_{el} = \frac{e}{(2\pi)^3} Im \sum_n \int \langle u_{n\mathbf{k}} \mid \nabla_{\mathbf{k}} \mid u_{n\mathbf{k}} \rangle, \tag{2.131}$$

This polarization is the electronic part of the polarization. To obtain total polarization, ionic part should be added to electronic ($\mathbf{P} = \mathbf{P}_{el} + \mathbf{P}_{ion}$). Ionic polarization is simply defined as:

$$\mathbf{P}_{ion} = \frac{e}{\Omega}\sum_s q_s \mathbf{r}_s, \tag{2.132}$$

where q_s are charges of ions. One might note that term $\langle u_{n\mathbf{k}} \mid \nabla_{\mathbf{k}} \mid u_{n\mathbf{k}} \rangle$ also appears in the Berry phase definition and that is the reason why is the modern polarization theory called Berry phase. Polarization defined in such a way is multivalued, modulo $\frac{e}{\Omega}\mathbf{R}_i$, where $\mathbf{R}_i$ is the unit cell vector along i-th direction. To obtain single value total polarization, it should be calculated in reference to the centrosymmetric structure [49–51, 53].

2.8 The algorithm of atomic and electronic structure calculations

In previous sections we have explained the methods used to calculate atomic and electronic structure. The algorithm of the whole procedure is schematically described in Fig. 2.9. The calculation starts with an initial structure witch can be ideal crystalline or amorphous structure, depending on the particular case. Then, MC simulation is performed to obtain equilibrium structure, which is subsequently used as input for electronic structure calculations. The first step in electronic structure calculations is CPM which gives charge density spatial distribution. To start the

CPM calculation, motifs (contributions to overall charge density) are needed. They are extracted form DFT calculations on small prototype system (single molecule or few monomers of a polymer). When charge density is calculated, single particle potential can be obtained by solving Poisson equation and using LDA expression for exchange-correlation term. To obtain final electronic structure (wave functions and energies) FSM and OFM can be used. For small molecules FSM provides relatively quick solution. For conjugated polymers, OFM is more convenient choice due to the intuitive division of polymers into fragments. In some cases, effects of charge transfer on electronic structure are important. Then, DFTB+ code, which includes charge transfer into calculation, is used instead of OFM.

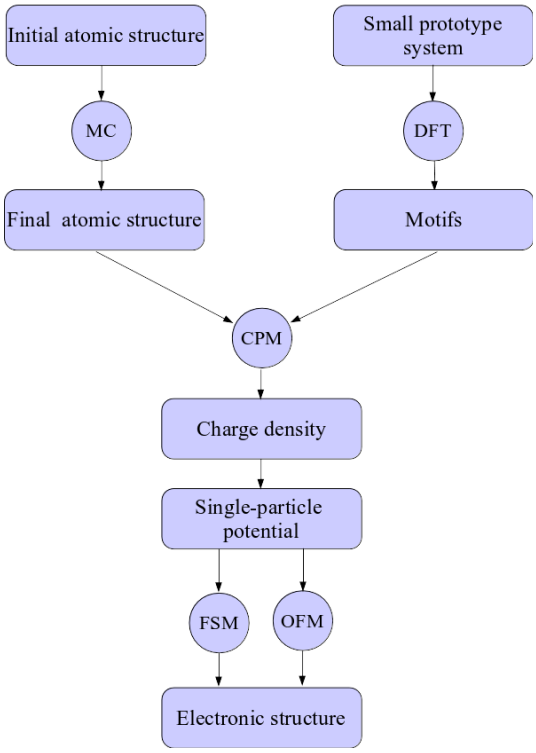

Figure 2.9: Schematic representation of the algorithm for atomic and electronic structure calculations.

Chapter 3

Electronic states at low-angle grain boundaries in polycrystalline small-molecule organic semiconductors

3.1 Introduction

Thin films of crystalline organic semiconductors have a polycrystalline form, which is composed of many different crystalline grains. It has been shown that the transport in a single grain boundary device is limited by the grain boundary [9]. A pronounced dependence of transistor characteristics on the grain size was also established [12, 15, 16, 54], as well as a strong difference between the characteristics of single crystal and polycrystalline transistors based on the same material [11]. It was also shown that grain boundary orientation has a large influence on the charge carrier mobility [18]. All these results indicate that grain boundaries are the most limiting intrinsic factor for efficient charge transport in small-molecule based polycrystalline organic semiconductors.

However, there is still a lack of understanding of the specific mechanism by which grain boundaries affect the charge transport. It is typically assumed that

they introduce trap states localized at the grain boundary, with energies of these states within the band gap of the material [9, 11, 12, 54–56]. The charges in the trap states do not contribute to transport and therefore the presence of traps reduces the effective charge carrier mobility. On the other hand, there are some suggestions that grain boundaries act as barriers and that charge carriers are trapped in the grains [21]. Calculations of electrostatic potential at molecules near the grain boundary formed from two misaligned grains indicate the presence of trapping centers at the boundary [57]. Other theoretical and computational studies are primarily focused on the properties of single crystals [58–69].

In this chapter we shed light on the nature of electronic states at grain boundaries in organic crystalline semiconductors. We directly calculate the wave functions of electronic states and gain microscopic insight into the origin of these states. Using these insights, we develop a simple model for density of trap states prediction. We firstly use naphthalene as a representative of crystalline organic semiconductors based on small molecules. We find that grain boundaries produce trap states in the band gap, where the highest states are localized on pairs of molecules at the grain boundary, whose mutual distance is much smaller than the corresponding distance in the monocrystal. Strong correlation between the mutual distance between these molecules and the energies of these states was found. Such a correlation enables one to calculate the electronic density of states at the grain boundary directly from mutual distances between molecules. Finally, we do similar calculations for benzothieno[3,2-b]benzothiophene (BTBT) and 2,7-di-tert-butylBTBT (ditBu-BTBT) molecules [70]. While results for BTBT are similar to those obtained for naphthalene, results for ditBu-BTBT are qualitatively different as we find no trap states at grain boundary, which is explained by the presence of side groups that prevent molecules from close packing.

3.2 Electronic states at low-angle grain boundaries in polycrystalline naphthalene

The atomic structure of polycrystalline naphthalene is obtained from a relaxation procedure based on the MC method, and is subsequently used to calculate the electronic states using the DFT-based based CPM. Initial configuration for MC relaxation are two monocrystals with different crystalline orientations joined at their common boundary. Potential energy of a system is calculated using Transferable potentials for phase equilibria (TraPPE). [71,72] The validity of the empirical potentials used in the MC simulation was verified by comparing the naphthalene crystal lattice constants obtained from these empirical potentials to the values from the literature. The obtained lattice constants are: $a = 8.325$ Å, $b = 5.92$ Å and $c = 7.77$ Å, which are in good agreement with the values given in Refs. 73–75. Naphthalene molecules are considered as rigid bodies, hence only interactions between carbon atoms from different molecules described by the weak Van der Waals interaction are taken into account. Carbon - hydrogen (CH) groups are treated as one atom with a center of mass at carbon atoms. TraPPE parameters for interactions between CH groups are: $\sigma = 3.695$ Å, $\epsilon/k_B = 50.5$ K and for interaction between C atoms: $\sigma = 3.7$ Å, $\epsilon/k_B = 30$ K. A MC algorithm was then used to minimize the energy of the system. Simulation is performed at a temperature of 300 K. After the thermal equilibrium is reached, the system is gradually cooled down to 0 K. In this way, dynamic disorder (crystal disorder induced by thermal motion) effects [58] are excluded. Both the effects of dynamic disorder and grain boundaries can in principle induce localized states and it would be very difficult to distinguish between these if the electronic structure calculations were performed for a structure obtained from a snapshot of MC simulations at 300 K. To check that the choice of the temperature of 300 K has only a small effect on the final atomic structure obtained from a MC procedure, we repeated the simulations using the temperatures of 100 K, 200 K and 400 K, as well. Atomic structures obtained from these simulations were nearly identical as the atomic structure obtained from the simulation at 300 K. Therefore, MC simulation procedure is robust in the sense that the final structure is weakly dependent on the

details of the procedure.

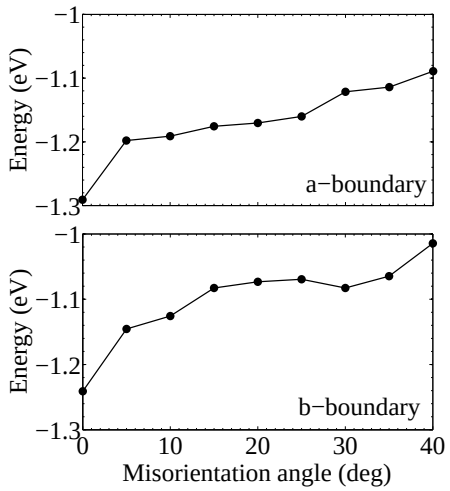

Figure 3.1: The dependence of potential energy of the system per molecule on the misorientation angle between monocrystal grains for a-boundary systems (top) and b-boundary systems (bottom). Each system consists of 1000 molecules.

Now, we present the results for the wave functions of states at grain boundaries in polycrystalline naphthalene. We consider the system consisting of 1000 molecules (500 at each side of the boundary) arranged in 10 layers which are parallel to the ab plane [73] of the unit cell. Electronic structure calculations are performed for a single layer of molecules, which is sufficient to describe the electronic properties of the material, because the electronic coupling in the c direction is much weaker than in the ab plane. Calculations are performed for several misorientation angles between the grains: 5°, 10°, 15° and 20° and for 2 types of grain boundaries: (1) perpendicular to the a direction (a-boundary) and (2) perpendicular to the b direction (b-boundary) of the unit cell. Only small angles are considered, because total energy of the system increases as the angle of misorientation increases, as demonstrated in Fig. 4.3. For each system, the energies of the 10 highest occupied states in the valence band and their wave functions are calculated.

Results of electronic structure calculations for the a-boundary system with misorientation angle of 10° are presented in Fig. 3.2. These results indicate that there are several states in the band gap which energies are significantly higher than the

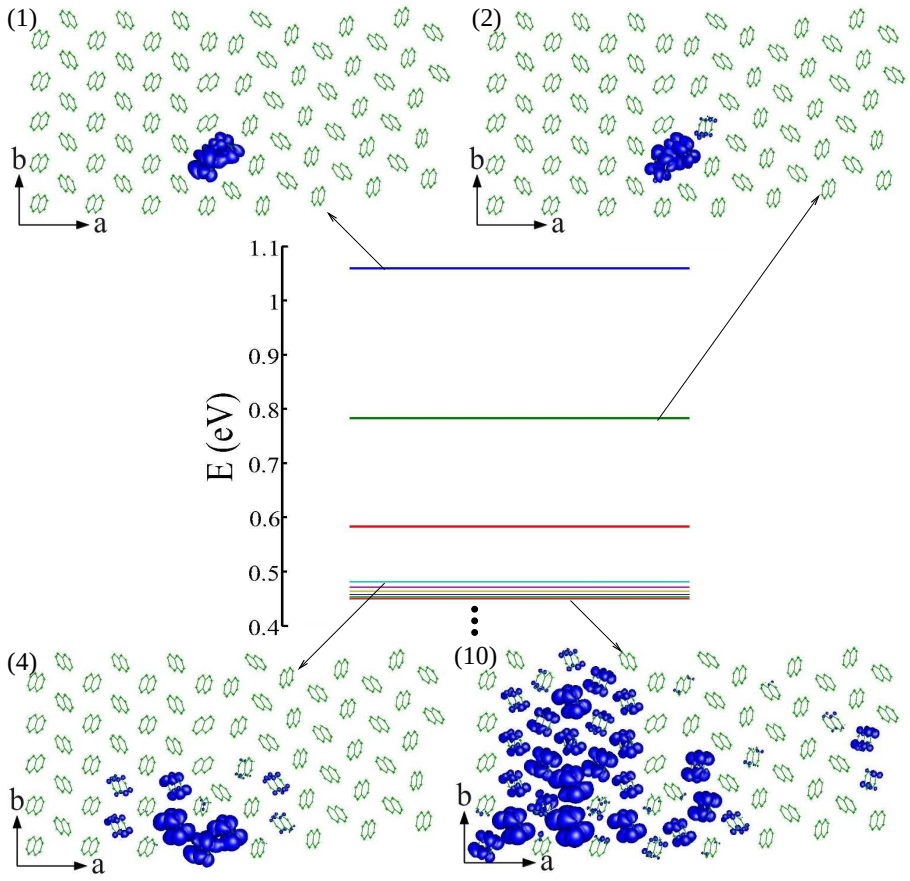

Figure 3.2: Energies of the states at the top of the valence band and the isosurfaces of their wave function moduli for the system with the misorientation angle of 10° and the grain boundary perpendicular to the a direction. Isosurfaces correspond to the probability of finding a hole inside the surface of 90%.

energies of the other states. These states are trap states for charge carriers and could strongly affect transport properties of the material. Wave functions of the first and the second highest occupied state are localized on the two molecules at the grain boundary. Distance between these two molecules (defined hereafter as the distance between their centers of mass) is 3.45 Å, while the distance between two nearest molecules in the monocrystal is about 5 Å. Highest occupied states in organic semiconductors originate from electronic coupling of HOMO (highest occupied molecular orbital) levels of different molecules. Electronic coupling that results from the overlap of HOMO orbitals is strongest for closely spaced molecules. As a consequence, the highest state in Fig. 3.2 is localized on two molecules with smallest mutual distance. It is the bonding states of HOMO orbitals of the two molecules, while the second state in Fig. 3.2 is the antibonding state. At certain energies the spectrum becomes nearly continuous and the states which are completely delocalized start to appear, such as the 10th calculated state, see Fig. 3.2. States like this originate from delocalized Bloch states of the monocrystal and therefore are not induced by grain boundaries.

Electronic calculations for other misorientation angles and boundary directions show similar results. In Fig. 3.3, the results for *b*-boundary system and misorientation angle of 10° are presented. In this case, there is only one molecule pair at the grain boundary with small mutual distance and consequently one trap state deep in the band gap. Other states are delocalized.

The presented results indicate that grain boundaries introduce electronic states within the band gap of the material. Hereafter, the states localized at the boundaries will be called trap states, while delocalized states will be called valence band states. Some trap states are very deep in the band gap, even more than 1 eV above the valence band. As a reference, experimentally measured band gap of naphthalene is about 5.2 eV [74]. The traps with energies significantly above the top of the valence band (more than 0.1 eV) are always localized on two molecules belonging to different grains with mutual distance less than the distance between two nearest molecules in the monocrystal. Such pairs of molecules will be hereafter called trapping pairs. Other localized states at the grain boundary have energies very close to the energies

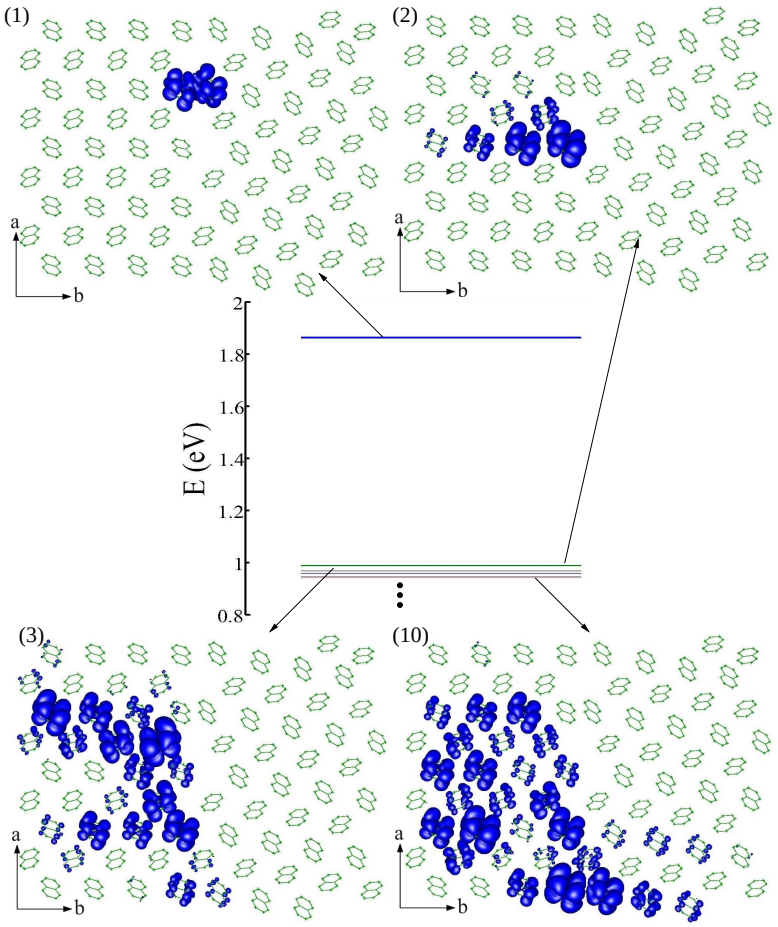

Figure 3.3: Energies of the states at the top of the valence band and the isosurfaces of their wave function moduli for the system with the misorientation angle of 10° and the grain boundary perpendicular to the b direction. Isosurfaces correspond to the probability of finding a hole inside the surface of 90%.

of the top of the valence band (second state in Fig. 3.3, for example). Consequently, only pairs of molecules (trapping pairs) will be taken into account. We find that there is a strong correlation between the distance between the molecules in trapping pairs and the energy of the trap electronic states. This dependence is shown in Fig. 3.4. The best fit of this dependence is given by an exponential function $\Delta E = Ae^{B(R-R_0)}$, where $A = 1.4064\,\text{eV}$, $B = -4.181\,\text{Å}^{-1}$ and $R_0 = 3.2\,\text{Å}$.

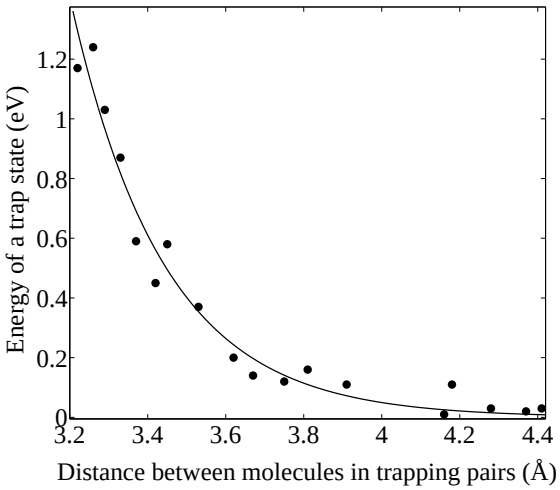

Figure 3.4: The dependence of the energy of the grain boundary induced trap states on the distance between molecules in trapping pairs. The data obtained from all simulated systems are presented in the figure. Energies of the trapping states are defined with the top of the valence band as a reference level.

Electronic structure calculations can be performed for relatively small boundaries only. While such calculations were highly valuable for understanding the origin and the degree of wave function localization at the boundary, they do not provide sufficient statistics to reliably calculate the density of trap states. On the other hand, the remarkable dependence, presented in Fig. 3.4 can be used to predict the energy of a trap at a given boundary without any electronic calculation, solely based on the distances between the molecules. This allows us to calculate the energies of all trap states for very large grain boundaries and consequently calculate the electronic density of trap states. Based on the degree of scattering of the data from the fit in Fig. 3.4, we estimate that this method produces an error in the trap energy

calculation of up to 0.1 eV.

Consequently, we have demonstrated that computationally demanding electronic structure calculations can be avoided using the aforementioned approach. Next, we show that even the MC relaxation step can be avoided without significantly compromising the accuracy of electronic density of trap states. By inspecting the atomic structure near the boundaries in Fig. 3.2, one can notice that it stays nearly unchanged after the relaxation. Only molecules in the vicinity of the boundary slightly change their positions and orientations. The difference in the distance between two molecules in trapping pairs, before and after the relaxation is below 0.1 Å, as demonstrated in Fig. 3.5. Consequently, both MC relaxation and electronic structure calculations can be avoided in the calculation of electronic density of trap states.

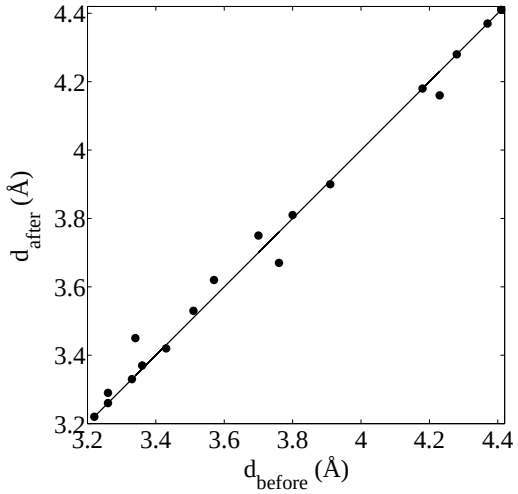

Figure 3.5: Dependence of the distance between trapping molecule pairs after MC relaxation (d_{after}) on the distance between them before MC relaxation (d_{before}).

The electronic density of trap states was extracted from the calculations of grain boundaries that contain 100 000 molecules arranged in 100 layers. In the construction of grain boundary atomic structure, there is an ambiguity related to the width of the void between the two monocrystals that form the boundary. This issue was overcome by shifting one of the crystals in the direction perpendicular to the boundary and selecting the void width in such a way that the potential energy of the system is minimal. The distribution of distances between trapping pairs of

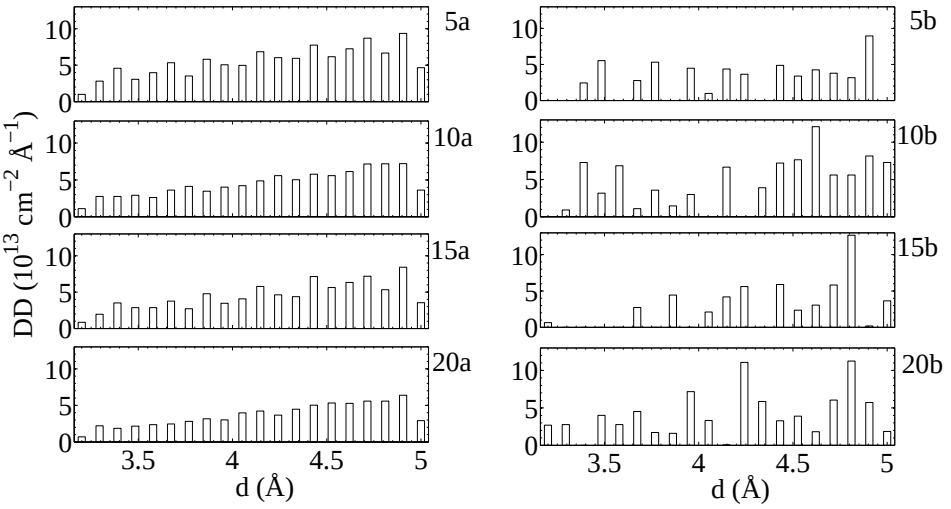

Figure 3.6: Trapping pair distance (d) distributions (DD) at different grain boundaries. The boundaries are denoted as Xy, where X is the angle between monocrystal grains and y is the direction perpendicular to the boundary surface.

molecules is calculated then. Next, using the previously introduced exponential fitting function, the electronic density of trap states is obtained. The results are presented for 4 different angles: 5°, 10°, 15° and 20° and for 2 orientations of grain boundaries: a-boundary and b-boundary. As can be seen from Fig. 3.4, trapping pairs with mutual distances below 4 Å are responsible for traps which are deep in the band gap. Other trapping pairs produce shallow traps which are close to the top of the valence band. The distribution of distances between molecules in trapping pairs at the grain boundaries is shown in Fig. 3.6. One should note that molecule pairs with distances below 3.2 Å can also exist. However, these were not present in small systems the we considered, hence their energy can not be reliably calculated using the fitting function. Nevertheless, such states are rather rare and we neglect their surface density.

By inspecting Fig. 3.6, one can notice that trapping pairs distance distributions for a-boundary systems are similar for all angles. All of them are increasing functions with similar shapes. On the other hand, the distributions for b-boundary systems largely depend on misorientation angle. In addition, the distribution is not continu-

ous as it is for a-boundary and some distances are preferred. This difference can be explained by the geometry of the naphthalene unit cell. Only a and c directions of the unit cell are not perpendicular. Therefore, the c direction is not parallel to the a-boundary surface. For this reason, in the case of a-boundary, different ab planes give different contribution to trapping pair distance distribution. By adding the contribution from different ab planes, one obtains a continuous function. In the case of b-boundary, c direction is parallel to the grain boundary surface. Consequently, molecule pairs from one ab plane have their copies in other ab planes and each ab plane gives the same contribution to trapping pair densities. This produces discrete trapping pair distance distributions. Difference between a- and b-boundary is illustrated in Fig. 3.7, where spatial distribution of trapping pair distance is given. Each filled circle in Fig. 3.7 represents a molecule in the layer at the grain boundary. The color of the circle indicates the distance between that molecule and the nearest molecule from the opposite side of the boundary. As one can notice, in the case of a-boundary, distributions for different ab planes are different (as evidenced by the non-periodicity of the pattern shown in the top part in Fig. 3.7), while distributions for different ab planes in the case of b-boundary are equal (as evidenced by the periodic pattern in the bottom part in Fig. 3.7).

With trapping pairs distance distributions at hand, the electronic density of trap states can be straightforwardly calculated as explained. Densities of trap states for 8 aforementioned boundaries are given in Fig. 3.8. Since the focus of this work is on trap states that are significantly above the top of the valence band, only trapping pairs with mutual distances below 4 Å are included in the distribution shown in Fig. 3.8. In addition, we have assumed that each trapping pair introduces one trap state, although in some cases it can introduce two trap states, as demonstrated in Fig. 3.2. For a-boundary systems, density of trap states weakly depends on angle. Going deeper in the band gap, density of trap states monotonously decreases which is a consequence of the monotonously decreasing density of trapping pairs at the grain boundary. For b-boundaries, density of trap states is discrete with some distances preferred as a consequence of discrete density of trapping pairs at the grain boundary.

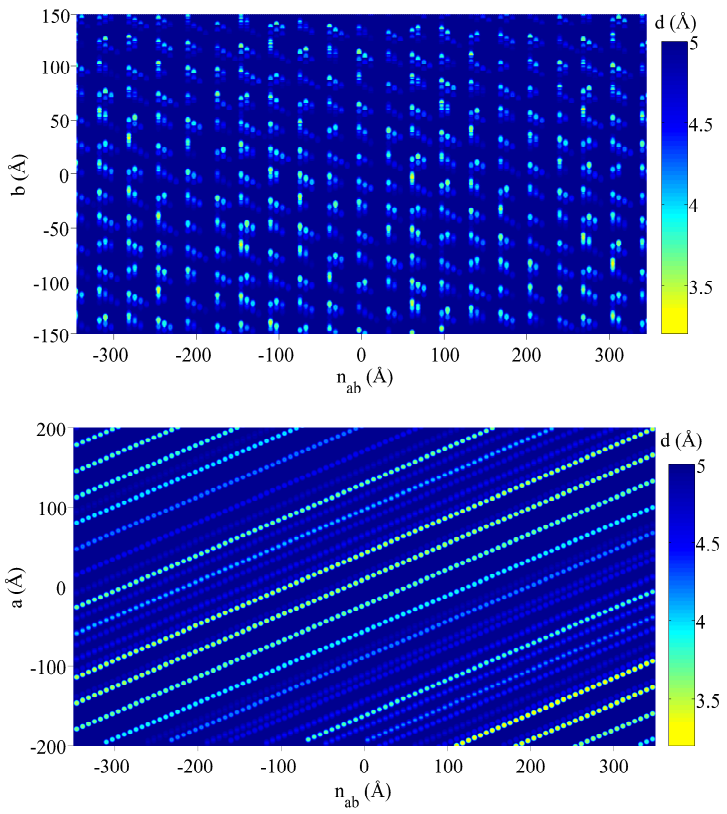

Figure 3.7: Spatial trapping pair distance distribution for a-boundary (left) and b-boundary (right) system with the misorientation angle of 10°. Axis perpendicular to the ab plane is denoted as n_{ab}. Spatial trapping pair distance distribution is calculated using radial symmetric function [76] calculated at position of molecular center of mass with cut-off radius of 14.8 Å.

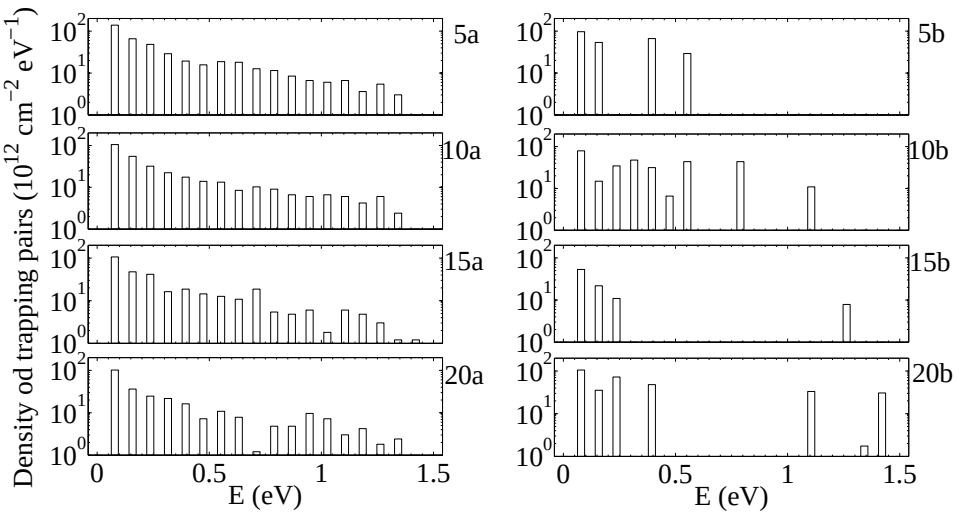

Figure 3.8: Electronic density of trap states at different grain boundaries. The boundaries are denoted as Xy, where X is the angle between monocrystal grains and y is the direction perpendicular to the boundary surface. Densities of trap states are given in a logarithmic scale. Energies of the trapping states are defined with the top of the valence band as a reference level.

Our results clearly demonstrate the presence of trap states at the positions in the grain boundary where two molecules from opposite sides of the boundary are closely spaced and hence the electronic coupling of their HOMO orbitals is rather strong. In Ref. 21 it was argued that grain boundaries act as barriers for charge carriers rather than traps. Such an argument was drawn from an assumption that electronic coupling between molecules is weaker at the grain boundary than in the bulk. Our results show that such an assumption is not appropriate; strong electronic coupling at certain positions at the boundary creates trap states within the band gap of the material. However, one should also note that electronic coupling between neighboring molecules from opposite sides of the boundary can be weak at certain positions. At these positions, grain boundary acts as a barrier and tends to confine the wave function to one side of the boundary. This effect can be seen from state (10) in Fig. 3.2 and states (3) and (10) in Fig. 3.3. Positions of strong electronic coupling and trap states will be absent only in the case of a grain boundary void when two grains with same orientation are separated by empty space. Consequently, a void (micro-crack) within an organic crystal [77] is expected to act as a barrier.

On the other hand, various numerical simulations of organic crystal FETs were based on a model that considers the transport at the boundary as thermoionic jump over the barrier or tunneling through the barrier [12,16,55,56]. One should note that FETs typically operate at high charge densities. Therefore, the traps become filled with carriers, that in turn create an electrostatic potential that acts as a barrier for the transport of other charges. Such "trap charging induced barriers" should be distinguished from the barriers discussed in the previous paragraph.

Using the obtained results, the density of trap states for naphthalene polycrystals can be estimated. The calculated number of trap states per unit of boundary surface of two misoriented grains is $3 \times 10^{13}\,\mathrm{cm}^{-2}$ in the case of misorientation angle of 5° and a-boundary, and takes similar values for other boundaries. Only trapping pairs with mutual distances below 4 Å were considered in the calculation. In the work of Chwang and Frisbie [9], the density of trap states was estimated from activation energies for charge transport in a single grain boundary FET based on sexithiophene. It was found that trap densities at acceptor-like levels take values

from 7.0×10^{11} cm^{-2} to 2.1×10^{13} cm^{-2}, depending on the grain boundary length and the angle of misorientation. Therefore, our results are of the same order of magnitude as the experimentally based estimate for the material belonging to the same class of materials as naphthalene.

Next, we estimate the number of grain boundary induced trap states per unit of volume and compare it to other relevant material parameters. Typical size of experimentally evidenced monocrystal grains [8, 9, 54, 78] is of the order of 1 μm, which translates into volume trap density of $N_{\rm t} = 9 \times 10^{17}$ cm^{-3} assuming grains of cubical shape. On the other hand, the number of energy states per unit of volume in the valence band of a bulk naphthalene monocrystal is $N_{\rm v} = 6.1 \times 10^{21}$ cm^{-3}. Although $N_{\rm t}$ is much lower than $N_{\rm v}$, it can still be significant to affect the charge transport and optical properties of naphthalene. In Ref. 78, grain boundary defects were identified as the most pronounced and the most stable defects. The density of point bulk defects was (over)estimated [78] to be in the $N_{\rm p} = 10^{14}$-10^{16} cm^{-3} range. Since our calculated value of $N_{\rm t}$ is larger than $N_{\rm p}$, our results confirm the conclusion that grain boundary defects are the most pronounced defects [78]. A compilation of the estimates of the density of trap states from FET characteristics was reported in Ref. 11. The estimated density of states at 0.2 eV above the valence band is in the range $(0.7 - 3) \times 10^{19}$ cm^{-3}eV^{-1}, while at 0.3 eV above the valence band it is in the $(1.5 - 4) \times 10^{18}$ cm^{-3}eV^{-1} range (see Fig. 6 in Ref. 11). On the basis of these values one can roughly estimate that the density of trap states with energies higher than 0.2 eV above the valence band to be in the $(10^{17} - 10^{18})$ cm^{-3} range, which is of the same order of magnitude as our calculated $N_{\rm t}$.

Finally, we discuss the implications of our findings on properties of electronic and optoelectronic devices based on this class of materials. Since our results show that hole traps are located at the positions of strongest electronic coupling between orbitals of the two molecules from opposite sides of the boundary, one expects that there will be an electronic trap at the same position. We have verified this expectation by performing explicit calculation of electron states at the boundary. As a consequence, traps at grain boundaries will not prevent radiative recombination of electrons and holes in LED devices or light absorption in the case of solar cells.

Nevertheless, the traps will certainly broaden the absorption or emission spectrum of the material. Furthermore, the estimated number of traps per unit of volume is comparable to typical charge carrier densities in operating LED and solar cell devices. As a consequence, charge carrier transport will certainly be strongly affected by the traps. On the other hand, FETs typically operate at charge carrier densities much larger than the trap densities. As a consequence, the traps are filled with carriers and affect the charge carrier transport only through electrostatic barriers created by the trapped charges, as discussed previously.

3.3 Electronic states at low-angle grain boundaries in polycrystalline BTBT and ditBu-BTBT

To check the results obtained for naphthelene and to broaden the understanding of grain boundaries in organic semiconductors, we have additionally investigated the electronic structure of low-angle grain boundaries in BTBT and ditBu-BTBT (Fig. 3.9). To obtain the atomic structures of the boundaries, Monte Carlo (MC) simulations are again applied. The simulation procedure is similar to that applied for grain boundaries in naphthalene. Initial configuration consists of two misaligned grains mutually shifted by some distance which minimizes the energy of the system. Temperature is set to 300 K and MC simulation is performed until the system reaches equilibrium. After that, system is cooled down to 0 K in order to exclude the effects of thermal disorder. OPLS - AA [31] parameter set is used to model the interaction between atoms. Unit cell parameters are taken from the crystallographic data files for these two molecules. In the case of BTBT these parameters are: $a = 11.80$ Å, $b = 5.85$ Å and $c = 7.96$ Å and all angles are 90° except one between a and c vectors that is 105.9°. For ditBu-BTBT these parameters are: $a = 14.02$ Å, $b = 6.04$ Å and $c = 10.55$ Å and all angles are 90° except one between a and c vectors that is 91.5°. Compatibility of the unit cell parameters with interaction parameters is checked by performing NPT MC simulations. Electronic structure is obtained using charge patching method and folded spectrum method.

We have performed calculations for several angles of misorientation (1°, 5°, 7.5°

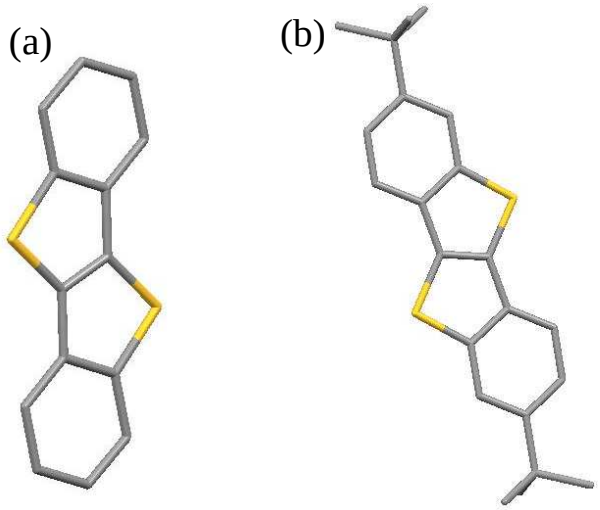

Figure 3.9: Graphical formula of (a) BTBT and (b) ditBu-BTBT molecules. Sulfur atoms are yellow, carbon atoms are gray, while hydrogen atoms are omitted.

and 10°) and two 2 different types of the boundary: $c-$boundary (boundary surface is perpendicular to the c direction of the unit cell) and $b-$boundary (analogously). Each boundary contains 10 unit cells in b and c direction and 1 in a direction (electronic coupling is weak in a direction).

Results for the electronic structure of grain boundaries in BTBT are similar to those obtained for naphthalene. Highest states in the valence band are localized on molecule pairs at the boundary where the distance between molecules is significantly smaller than in single crystal (Fig. 3.10 a). There are other localized states at the boundary (Fig. 3.10 b) which cannot be easily explained by some geometric parameter. These states generally have lower energies than states localized on molecule pairs. Finally, delocalized states start to appear at certain energies. As can be seen in Fig. 3.10c, they are mostly confined at one side of the boundary. Therefore, boundary can be interpreted as a barrier for delocalized states.

Energies of the states trapped at the molecule pairs correlate with the distance between molecules which form a trap. This dependence and exponential fit of the dependence are shown in Fig. 3.11. One can use this dependence to predict the number and the depth of trap states for larger system, only having the distribution of distances between molecules in hand. We have calculated the number of trap states

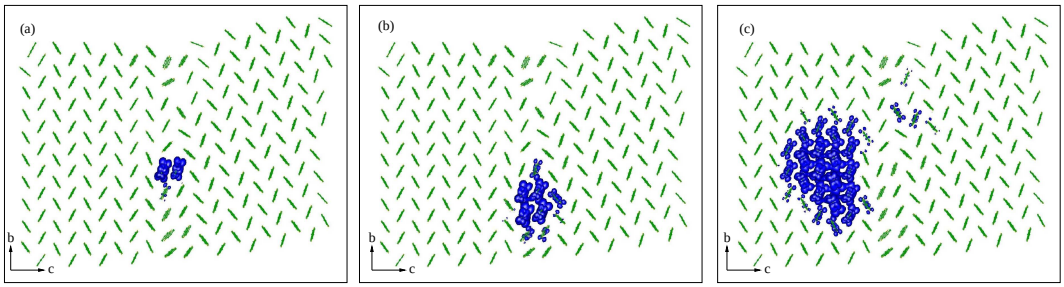

Figure 3.10: Wave function moduli squared of the: (a) highest electronic state in the valence band, (b) second highest electronic state in the valence band (c) highest delocalized electronic state in the valence band of the grain boundary that consist of two misaligned BTBT grains with angle of misorientation of 10°. Isosurfaces correspond to the probability of finding a hole inside the surface of 75%.

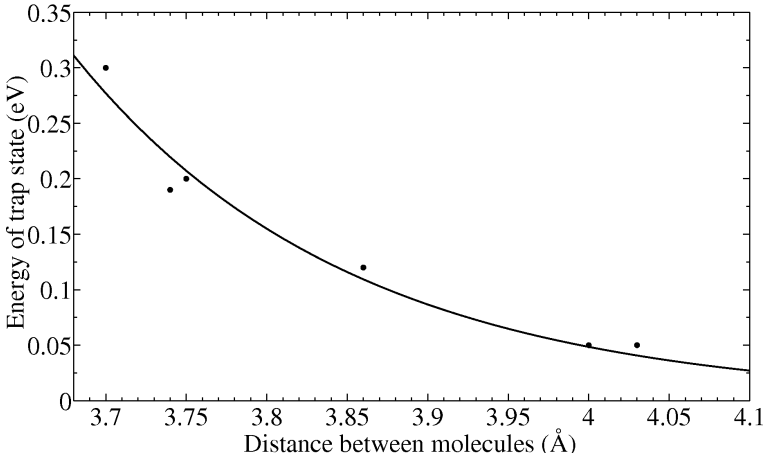

Figure 3.11: Dependence of the energies of trap states relative to the energies of the highest delocalized states on the distance between molecules that form a trap . Data is obtained for different angles of misorientation and for *c*- and *b*-boundaries in BTBT. Exponential fit is given by $E = a \exp^{b(R-R_0)}$, where a = 1.582 eV, b = -5.808 Å^{-1} and R_0 = 3.4 Å.

per boundary surface for the non-relaxed BTBT $c-$boundary with misorientation angle of 10° that contains 16000 molecules arranged in 20 layers. Distribution of distances for this system is given in Fig. 3.12. Peak at around 4.8 Å corresponds to the minimal distance between adjacent molecules in a single crystal. Number of molecule pairs per boundary surface (and the corresponding number of trap states) that have mutual distance below 4 Å is $6.2 \times 10^{12}\ cm^{-2}$, which is comparable to the same number obtained for naphthalene. Having in mind that number of trap states is obtained for non-relaxed structure (without performing MC simulations), this number can be somewhat different for relaxed structures, but general conclusions would remain the same.

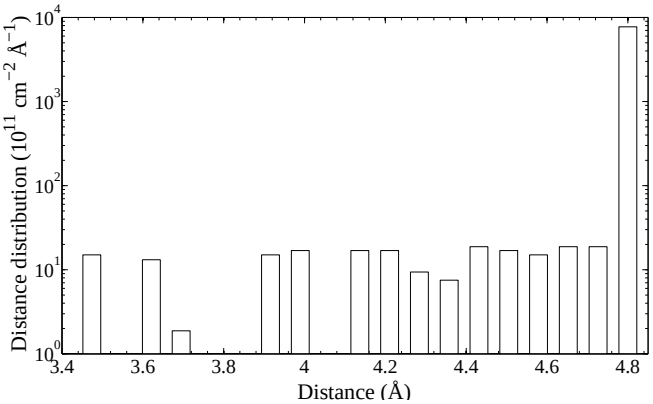

Figure 3.12: Distribution of distances between molecules at the grain boundary that consist of two misaligned BTBT grains with angle of misorientation of 10°.

Results for electronic structure of low-angle grain boundaries in ditBu-BTBT are significantly different. Here we do not find any trap states at the boundary. Highest states at the valence band are delocalized and mostly belonging to one grain, as shown in Fig. 3.13. The absence of trap states is the consequence of the absence of closely spaced molecules at the boundaries. This can be evidenced form the distribution of distances between molecules at the boundary which consists of 16000 molecules arranged in 20 layers, shown in Fig. 3.14. Minimal distance is around 5.5 Å, which is not enough small to create a trap. Such a big difference between BTBT and ditBu-BTBT is the consequence of bulky side groups in ditBu-BTBT that prevent molecules from close packing. Therefore, side groups play an important

role in molecule design. They determine the minimal distance between molecules and consequently the existence of trap states (and their number and depth if exist) that arise from close packing present at grain boundaries.

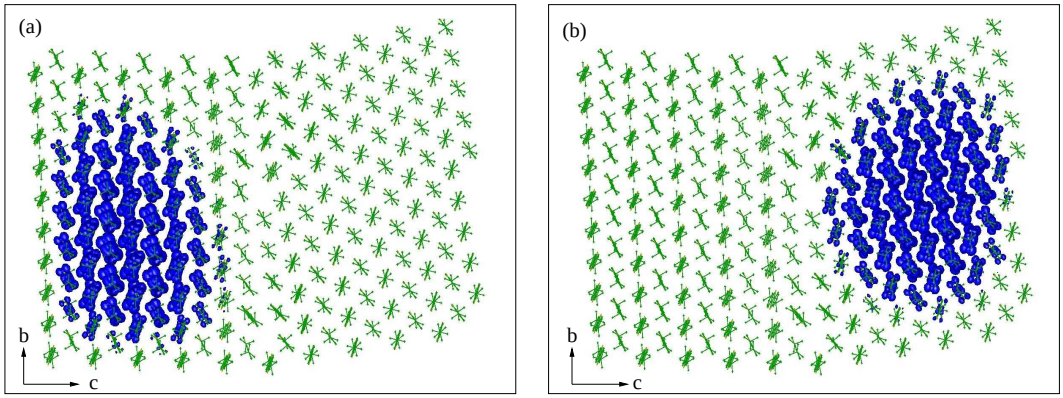

Figure 3.13: Wave function moduli squared of the: (a) highest electronic state in the valence band, (b) second highest electronic state in the valence band of the grain boundary that consist of two misaligned ditBu-BTBT grains with angle of misorientation of 10°. Isosurfaces correspond to the probability of finding a hole inside the surface of 75%.

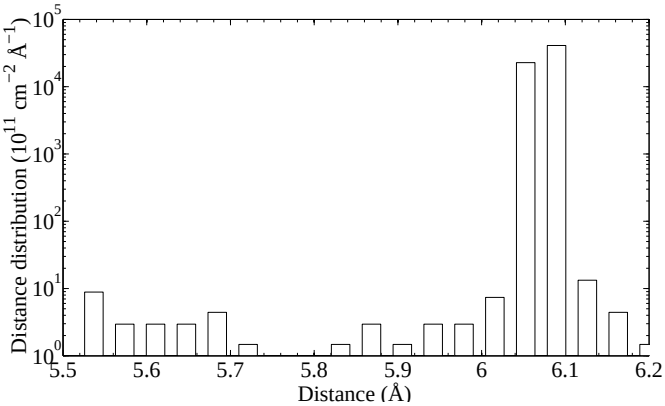

Figure 3.14: Distribution of distances between molecules at the grain boundary that consist of two misaligned ditBu-BTBT grains with angle of misorientation of 10°.

Chapter 4

Effects of thermal disorder on electronic properties of ordered polymers

4.1 Introduction

Conjugated polymers contain both crystalline and amorphous regions and consequently their electronic properties strongly depend on their morphology. In crystalline regions of the material, thiophene rings are connected into main (backbone) polymer chains, which then form two dimensional lamellar structures separated by insulating side chains.

Crystalline polymer regions exhibit better transport characteristics than amorphous regions. At first, one may expect that the electronic states in crystalline regions are fully delocalized due to the effect of periodicity. On the other hand, wave functions of electronic states in amorphous regions are well localized due to the effects of disorder. Calculations of the electronic structure of amorphous polymers show that wave functions of the highest states in the valence band are localized on few rings only [24,79]. The electronic states in crystalline regions may also exhibit localization due to the effects of thermal disorder; at finite temperature the atoms are displaced from their equilibrium positions in a random manner and the atomic positions no longer exhibit periodicity. The importance of the effects of thermal (or

dynamic, which is an alternative expression often used in the literature) disorder in small molecule based organic crystals is now widely recognized [80–86]. On the other hand, the effects of thermal disorder in polymers are less well understood. Currently available simulation results [87–89] suggest that the highest valence band states in ordered polymer materials at room temperature are localized. However, most of these calculations either consider a single polymer chain or do not include the effects of side chains.

The aim of this chapter is to investigate in detail the effects of thermal disorder on electronic properties of ordered polymer materials and to identify relative importance of various sources of thermal disorder. For concreteness, we choose poly(3-hexylthiophene) (P3HT) polymer for our study. We calculate the electronic density of states (DOS) and the localization of hole wave functions. Atomic configurations at finite temperature are obtained using MC [30] simulations, while CPM [20, 24, 39, 79, 90] and OFM [40, 79, 90] are used for electronic structure calculations.

The disorder in the structure at finite temperature comes both from the disorder in the shape of the flexible alkyl side chains (that will be referred to as side chain disorder from now on) and from the disorder due to variations of torsion angles between thiophene rings in the main chains and the position of main chains (that will be referred to as main chain disorder from now on) [91]. One should note that disorder of main or side chains does not imply an amorphous material. While it is well known that the wave functions in conjugated polymers are localized on the main chain, side chains with a disordered shape still affect the electronic structure as they create a disordered electrostatic potential on the main chain. Disorder in the shape of the main chain mostly affects the electronic structure through variations in electronic coupling between the rings. To isolate the effects of main and side chain disorder we investigate three types of structures: (1) the structures with straight main chains and disordered alkyl side chains; (2) the structures with disordered main chains in the absence of side chains; (3) the structures with both main and side chains disordered.

We find that the effects of disorder are least pronounced in the structures with

disordered side chains. Strong wave function localization of highest valence band states occurs in structures with main chains disordered, both with and without side chains. Such a localization is most likely the origin of thermally activated transport observed in all reported P3HT mobility measurements.

4.2 Methodology

The initial structure for MC simulations is the ideal crystalline structure of P3HT. Atomic structure of crystalline P3HT was extensively studied and different possible configurations were found [92–101]. Two different stable crystalline structures are simulated at 300 K: aligned and shifted, which are shown in Fig 4.1. In the aligned structure, thiophene rings from two adjacent main chains in the π-π stacking direction are aligned. On the other hand, in the shifted structure, thiophene rings from two adjacent chains in the π-π stacking direction are mutually shifted by the half of the unit cell in the main chain direction. Parameters of the unit cells are found using NPT (constant pressure and temperature) MC simulation at 300 K and 101.325 kPa. During the simulation, the size of the box in the main chain direction is kept constant, while two other dimensions are changed. The energy of the system is modeled as a sum of the long-range (Van der Waals and Coulomb) interactions between atoms from different chains. The unit cell parameters are determined as the parameters obtained when the system reaches thermal equilibrium. For the aligned structure these are: $a/2 = 15.7$ Å, $b = 8.2$ Å and $c = 7.77$ Å , while for the shifted structure these are: $a/2 = 15.7$ Å, $b = 8.1$ Å and $c = 7.77$ Å. All unit cell angles are taken to be 90°. These parameters are in very good agreement with previous computational results for the same structures of P3HT. For example, the unit cell parameters obtained for the aligned structure in Ref. 93 are: $a/2 = 16$ Å, $b = 8.2$ Å and $c = 7.81$ Å, while for the shifted these are: $a/2 = 16$ Å, $b = 7.85$ Å and $c = 7.81$ Å. On the other hand, experimental results based on the X-ray diffraction measurements suggest somewhat higher value for the side chains stacking direction of 16.8 Å [98]. This difference might originate from the assumption of the ideal crystal structure without disorder made in the calculations, which is not the case

in reality. Interdiggitation between side chains from different lamellas is weaker in more disordered structures, and consequently, the unit cell parameter for the side chains stacking direction is higher. We find that the shifted structure is more stable at 300 K, since its potential energy per number of rings is 0.38 eV lower than the corresponding energy in the aligned structure, confirming the result given in Ref. 93 that the shifted structure is more energetically favorable.

With the initial structure at hand, MC simulations are performed to obtain the snapshots of the atomic structure at room temperature. During the MC simulations bond lengths and bond angles are kept constant, while some or all torsion angles are changed. Variations of torsion angles affect electronic coupling between orbitals more strongly than variations of bond lengths and bond angles. For example, the thermal energy at room temperature $k_BT = 25$ meV leads to displacement of an atom due to bond stretching on the order of 0.02 Å , while the same energy leads to interring torsion angle change on the order of 45°, which yields the atomic displacements of more than 1 Å. For this reason, it is reasonable to keep bond angles and bond lengths constant. In each step of the MC simulation a new configuration is generated by changing the torsion angles and moving the whole polymer chain. The new configuration is accepted if it satisfies the Metropolis condition [30]. The energy of the system is calculated as a sum of torsion potentials and long range Van der Waals and Coulomb interactions. Thiophene - thiophene torsion potential is taken from Ref. 24, while thiophene - side chain torsion potential is taken from Ref. 93. The parameters for long range interactions are taken from the OPLS parameters set [31], which was previously successfully applied for the simulations of the same material [87]. This parameter set is also used for the torsion potentials within side chains. Periodic boundary conditions are applied in each direction of the unit cell for the systems with disorder in side chains. Boundary conditions are open in the main chain direction for the systems with disorder in main chains. The final atomic structure is taken after the system is thermally equilibrated at 300 K, which is evidenced from the saturation in the dependence of potential energy on the number of MC steps. Afterwards, electronic structure is obtained as explained in Sec. 2.8.

In this work, the effect of polarons was not included. Previous DFT calculations

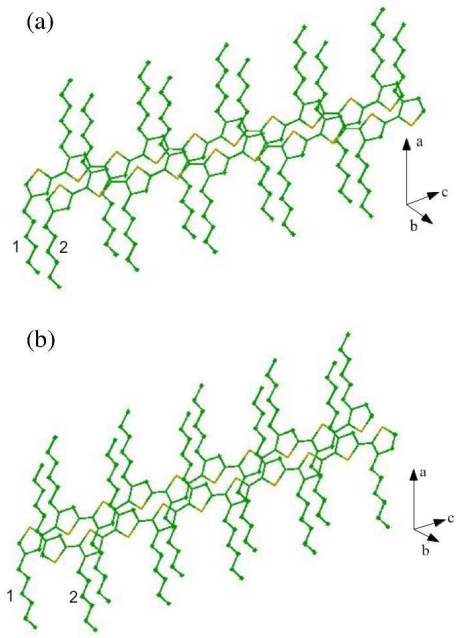

Figure 4.1: Two stable configurations of crystalline P3HT: (a) aligned and (b) shifted. The main chain direction is denoted by c, the π-π stacking direction by b and the side chains direction by a.

of long straight polythiophene chains at zero temperature indicate that polaron binding energy is on the order of few meVs only and that it can be ignored [102,103]. However, it is more difficult to assess the role of polarons at finite temperature when thermal disorder is present in the material. Since the main goal of this work is to understand the effect of thermal disorder on wave function localization and DOS, as well as the contributions from main and side chains to thermal disorder, polaronic effects were not considered.

Next, we discuss the appropriateness of LDA for the description of the localization effects. The localization effects that we observe essentially come from two effects: (i) variations of on-site energies of rings; (ii) variations in electronic coupling between the rings. The effect (i) comes mainly from disordered long range electrostatic potential that side chains, the rest of the main chain and other main chains produce on a certain ring. Within DFT, electrostatic potential is taken into account through the Hartree term in the Kohn-Sham equation, which is an exact term. Therefore, for the effect (i), the use of LDA in our calculation is not an is-

sue. To check if LDA gives reliable values of electronic coupling (the effect (ii)), we have performed the calculation of electronic energy levels of ten units long straight thiophene oligomer using either LDA or B3LYP functional for the same atomic configuration. We find that the spacing between energy levels calculated using these two functionals differs typically by 15 %. Since the spacing between energy levels of straight oligomers is proportional to electronic coupling between the rings, we conclude that possible uncertainties in electronic coupling calculated using LDA are on the order of 10-20% and such uncertainties are not expected to significantly affect the localization lengths.

4.3 Results

The effects of thermal disorder in crystalline P3HT are investigated by examining 3 different types of structures: the structures with disorder in side chains, the structures with disorder in main chains and the structures with disorder in both side and main chains. In the first case, main chains are kept rigid during the MC simulation, while side chains are allowed to move freely. In the second case, side chains are removed (more precisely, replaced with a hydrogen atom) before the electronic structure calculations start, in order to isolate the effects of main chains disorder. In the case of structures with the presence of disorder in both main and side chains, the same atomic configurations are used as for the second case, but side chains are not removed in this case. To get sufficiently large statistics, for each of the investigated cases and for both aligned and shifted structures, 100 different realizations are generated. Each configuration contains 10 polymer chains stacked in the π-π direction, while each chain contains 10 rings. The total number of atoms in each configuration is 2520. For subsequent analysis only 10 highest states from each configuration are taken into account, since they cover a spectral range of about 0.5 eV below the HOMO level, which is the range of interest for the electrical transport properties. To analyze the effects of disorder, we calculate the density of electronic states and the localization length of hole states.

Densities of states obtained from the calculations are shown in Fig. 4.2. In

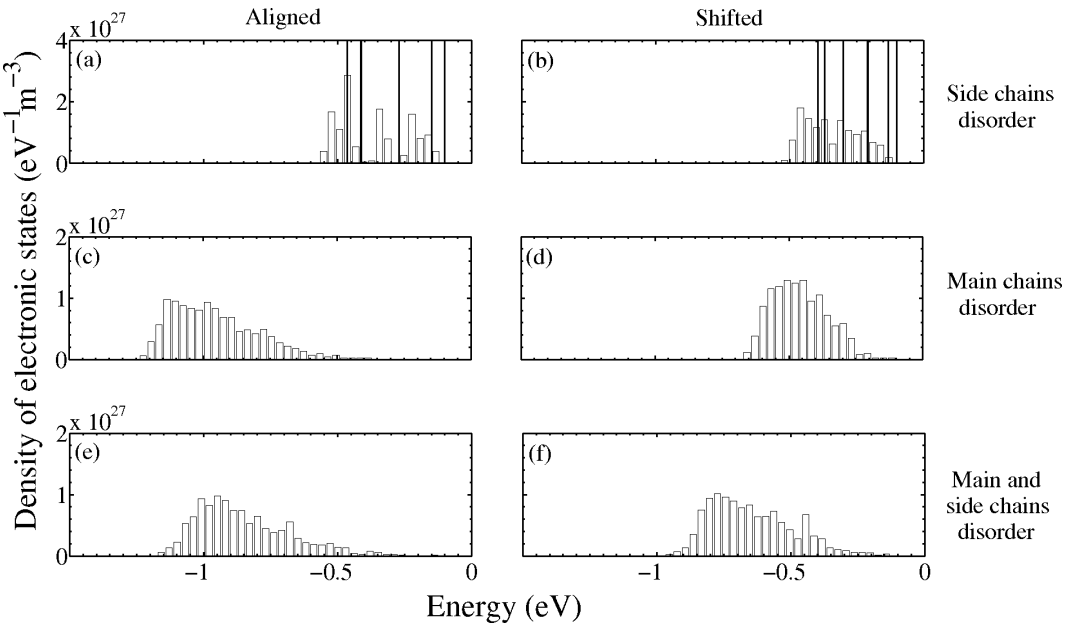

Figure 4.2: DOS in the case of: (a) aligned structure with disorder in the side chains (bins) and ideal crystalline aligned structure (vertical lines); (b) shifted structure with disorder in the side chains (bins) and ideal crystalline aligned structure (vertical lines); (c) aligned structure with disorder in main chains and side chains omitted; (d) shifted structure with disorder in main chains and side chains omitted; (e) aligned structure with disorder in both side and main chains (f) shifted structure with disorder in both side and main chains.

the case of disorder in side chains in the aligned structure, DOS is nearly discrete, composed of several peaks (Fig. 4.2a and Fig. 4.2b). These peaks correspond to the peaks in the DOS of the ideal crystalline structure without any disorder. In the shifted structure, peaks are broader and overlap more than in the aligned structure, making DOS continuous. Thus, the effects of side chains disorder on DOS are more pronounced in the shifted structure than in the aligned. The difference in DOS for shifted and aligned structures can be explained by the difference in the spatial distribution of side chains in these two structures. In the aligned structure, side chains connected to the aligned thiophene rings from neighboring chains in the π - π direction are at the same side of the main chains (chains denoted by 1 and 2 in Fig. 4.1a). On the other hand, in the shifted structure these side chains are at the opposite sides. The distance between nearest side chains in the shifted structure (chains denoted by 1 and 2 in Fig. 4.1b) is greater than in the aligned. Therefore, side chains in the shifted structure have more conformational freedom than in the aligned. This is evidenced by the distributions of the thiophene-side chain torsion angle for both structures, given in Fig. 4.3a and Fig. 4.3b. The distribution of thiophene-side chains torsion angles is significantly wider in the shifted structure, which results in higher degree of side chains disorder. This difference in morphology leads to the difference in the electronic structure.

In the structures with disordered main chains, DOS is continuous (Fig. 4.2c and Fig. 4.2d). In the case of aligned structures distribution of energies is significantly wider than in the shifted structure. Distributions of thiophene - thiophene torsion angles for the aligned and shifted structures are similar (Fig. 4.3c and Fig. 4.3d) and agree well with the results of Ref. 88. Therefore, the difference in the distribution of the energies is not caused by the shape of the chains. Electronic coupling between different chains is 0.11 eV in the ideal aligned structure and 0.07 eV in the ideal shifted structure. This substantial difference leads to the wider distribution of the energies in the aligned structure. When both main and side chains are disordered, the DOS is continuous (Fig. 4.2e and Fig. 4.2f) without any apparent difference between structures. This similarity in DOS can be explained by the effect of compensation between wider energy distribution in the shifted structure when only side

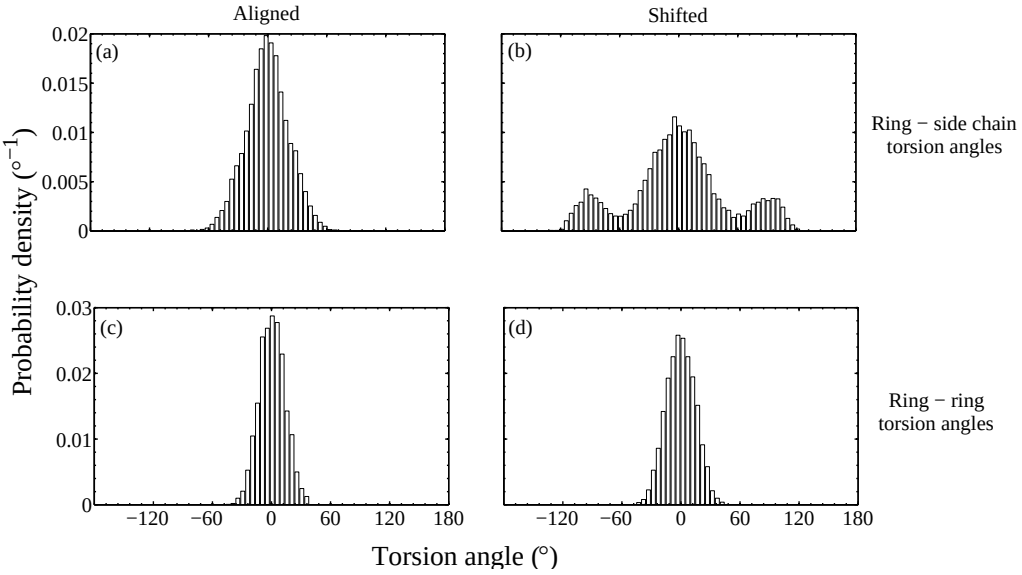

Figure 4.3: Distribution of the: (a) thiophene-side chains torsion angles in the aligned structure; (b) thiophene-side chains torsion angles in the shifted structure; (c) thiophene-thiophene torsion angles in the aligned structure; (d) thiophene-thiophene torsion angles in the shifted structure. In panels (c) and (d) the angles are shifted by 180° for clarity. To exclude the effects of finite box dimension in the main chain direction, in (c), (d), (e) and (f) only torsion angles between rings in the middle of the chains are taken into account.

chains are disordered and wider energy distribution in the aligned structure when only main chains are disordered.

Suitable measure of disorder in the system is the distribution of diagonal Hamiltonian elements given by $H_{ii} = \langle i \mid H \mid i \rangle$, where $\mid i \rangle$ are wave functions of trimers and H is the Hamiltonian of the system. Wave functions of the trimers are localized on the main chain and on the carbon atoms in the side chains closest to the thiophene rings. Consequently, if main chains of trimers are rigid, their wave functions and energies of HOMO levels will be equal. When only disorder in side chains is applied, difference between diagonal Hamiltonian elements arises only from variations in H, due to the variations in the electrostatics potential caused by side chains disorder. On the other hand, when disorder in main chains is present, variations in H_{ii} arises both form H and $\mid i \rangle$, since wave functions of trimers now differ signifi-

cantly. Distributions of diagonal elements of the Hamiltonian are given in Fig. 4.4. As expected, distributions are widest in the case when both disorders are present (Fig. 4.4e and Fig. 4.4f). Having in mind the results for DOS presented above which suggest that disorder in main chains has more impact on the electronic structure of P3HT than disorder in side chains, one may find unexpected that distributions given in Fig. 4.4c and Fig. 4.4d are similar to the distributions given in Fig. 4.4a and Fig. 4.4b. Side chains have more conformational freedom than main chains, especially in the shifted structure. Therefore, their disorder affects the electrostatical potential more than disorder in main chains. When effects of disorder in main chains are isolated, side chains are removed and, consequently, variations of electrostatic potential are weaker than in the case of disorder in side chains, which leads to the weaker variations in H.

Wave functions of HOMO levels for 6 different cases are shown in Fig. 4.5. In the ideal crystalline structure the wave function of HOMO level (and any other level) is completely delocalized, as Bloch theory predicts. When the side chains disorder is partially applied, wave functions remain delocalized (Fig. 4.5a and Fig. 4.5b). They are not delocalized along the whole structure, as in the ideal structure. Delocalization is broken both in the π-π stacking direction and in the main chain direction. On the other hand, wave functions of HOMO levels in the case of disorder in main chains are localized, both with and without side chains included (Fig. 4.5c - f). They are localized on 5 - 15 rings, usually on 2 neighboring chains (as in Fig. 4.5c and Fig. 4.5e). Therefore, thermal disorder in the crystalline P3HT localizes the wave function of HOMO level, as in the amorphous phase [24, 79].

To investigate the effects of disorder on the wave functions localization more precisely, we calculate two localization lengths for each state: localization in the π-π stacking direction L_b and localization in the main chain direction L_c. If the wave functions are represented in the orthonormal basis set of well localized orbitals, the localization length can be generally defined as $L = 1/\sum_m |d_m|^4$, where d_m are expansion coefficients of the wave functions in the orthonormal basis $|m\rangle$ [79]. The basis set used in the OFM calculations is not orthonormal. The orthonormal basis set is constructed by transformation $|m\rangle = \sum_m T_{mi} |i\rangle$ with transformation matrix

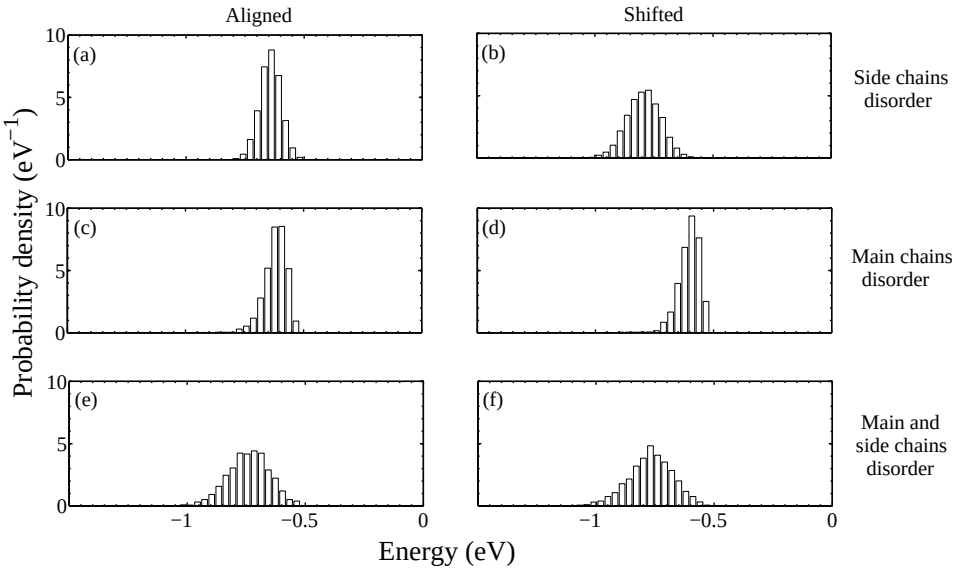

Figure 4.4: Distribution of the diagonal elements of the Hamiltonian in: (a) aligned structure with disorder in side chains; (b) shifted structure with disorder in side chains; (c) aligned structure with disorder in main chains and side chains omitted; (d) shifted structure with disorder in main chains and side chains omitted; (e) aligned structure with disorder in both main and side chains and (f) shifted structure with disorder in both main and side chains. To exclude the effects of finite box dimension in the main chain direction, in (c), (d), (e) and (f) only trimers in the middle of the chains are taken into account.

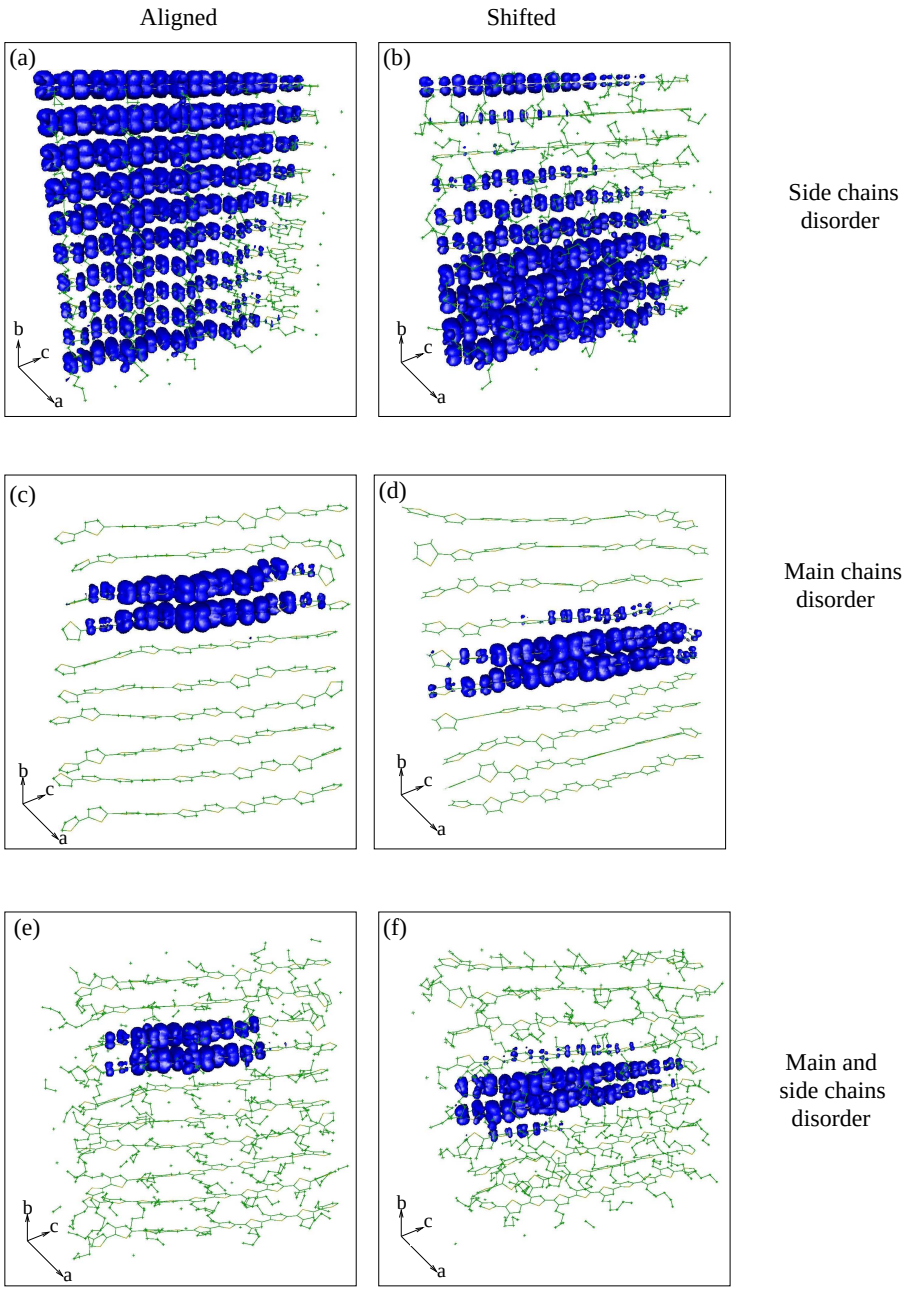

Figure 4.5: Wave function moduli of the HOMO level of crystalline P3HT in the case of: aligned structure with disorder in side chains; (b) shifted structure with disorder in side chains; (c) aligned structure with disorder in main chains and side chains omitted; (d) shifted structure with disorder in main chains and side chains omitted; (e) aligned structure with disorder in both side and main chains (f) shifted structure with disorder in both side and main chains. Isosurfaces correspond to the probability of finding a hole inside the surface of 90%.

$T = (S^{-1/2})^*$, where S is the original overlap matrix and $|i\rangle$ are original basis wave functions. Expansion coefficients of the orthonormal basis set are related to the original coefficients c_i via $d_m = \sum_i (S^{1/2})_{mi} c_i$. For the orthonormal basis set the condition $\sum_m |d_m|^2 = 1$ is satisfied. In our case, this sum can be divided into two sums, one over different chains and other over rings in one chain: $\sum_{i=1}^{N_c} \sum_{j=1}^{N_m} |\beta_{ij}|^2 = 1$, where N_c and N_m are the number of chains and the number of rings within one chain, respectively. Following the general definition of the localization length, L_b is defined as $L_b = 1/\sum_i \left|\beta_i'\right|^4$, where $\left|\beta_i'\right|^2 = \sum_{j=1}^{N_m} |\beta_{ij}|^2$. Similarly, L_c is defined as $L_c = 1/\sum_j \left|\beta_j''\right|^4$, where $\left|\beta_j''\right|^2 = \sum_{i=1}^{N_c} |\beta_{ij}|^2$.

Plots of the dependence of L_b on energy of the electronic states are shown in Fig. 4.6. In the ideal crystalline structure (both aligned and shifted), L_b of the HOMO level is equal to the number of chains, which is 10 in this case. Lower states in the ideal structure have L_b either 6.67 or 10. In the case of the aligned structure with disordered side chains (Fig. 4.6a), the values of L_b for HOMO level vary from 4 to 10. Other states have L_b which is around the value of L_b in the ideal structure. In the case of the shifted structure, distribution of the energies of states is wider then in the aligned. Consequently, it is difficult to isolate the values of L_b for HOMO levels from Fig. 4.6b. Looking into the range of 0.2 eV below the highest energy, value of L_b is between 3 and 6, which is lower than the values of L_b in aligned structures. Therefore, wave functions of HOMO levels are more localized in the shifted structure than in the aligned. In all remaining cases (Fig. 4.6c-f) we get qualitatively similar results. Values of L_b for the highest occupied states are low, they take values from 2 to 4 chains. States with lower energies have wider distributions of L_b, suggesting that delocalized states exist. Shape of the plot of L_b is similar to the plot of the hole localization length of the amorphous P3HT, given in Ref. 79.

Results for L_c are similar to the results for L_b. Minimal value for L_c when both side and main chains are disordered is 3. Electronic coupling is stronger in the main chain direction than in the π-π stacking direction and therefore localization in the π-π stacking direction is stronger than in the chain direction. It is interesting to note that the highest states in the valence band are typically localized on 2 neighboring chains. State will be localized on two chains if the electronic coupling

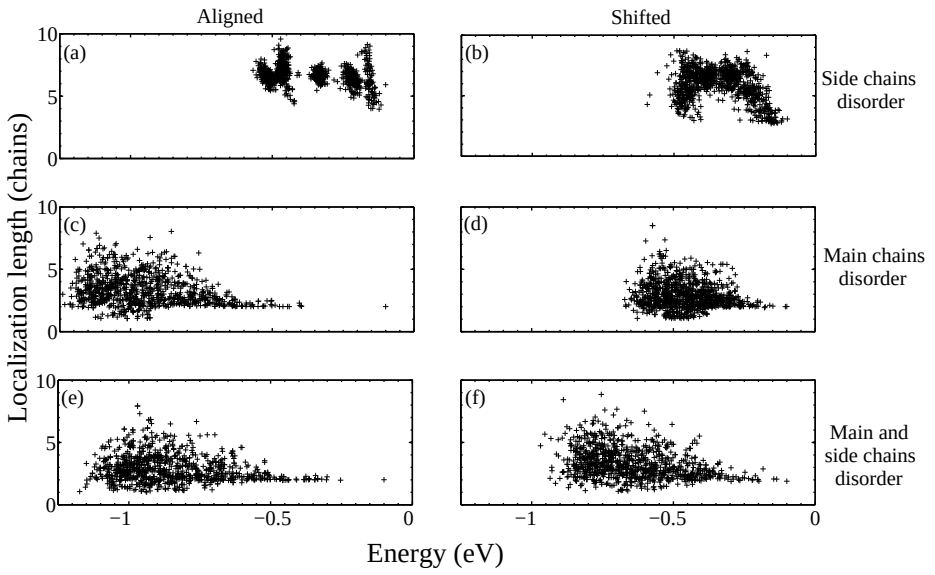

Figure 4.6: Dependence of L_b on the energy of the electronic state in the case of: aligned structure with disorder in the side chains; (b) shifted structure with disorder in the side chains; (c) aligned structure with disorder in main chains and side chains omitted; (d) shifted structure with disorder in main chains and side chains omitted; (e) aligned structure with disorder in both side and main chains (f) shifted structure with disorder in both side and main chains.

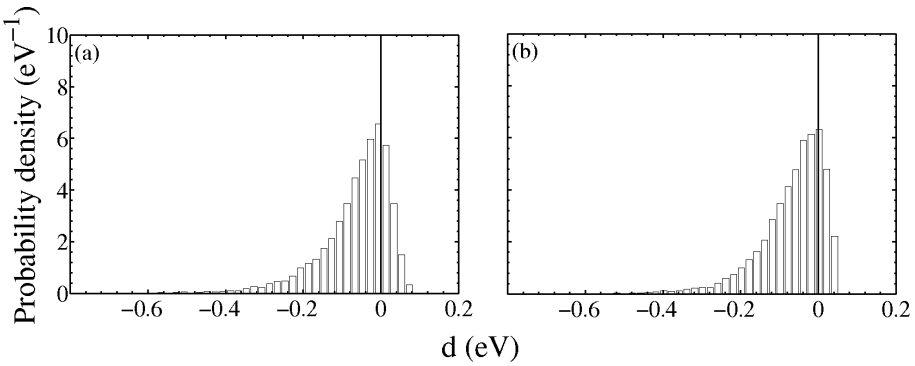

Figure 4.7: Distribution of difference between electronic coupling between chains and variations of diagonal Hamiltonian elements in the case of: (a) aligned and (b) shifted structure.

$t_{mn} = \langle m| H |n\rangle$ between orbitals m and n from different chains is greater then variations of the diagonal Hamiltonian elements. The distributions of the quanitity $d = t_{mn} - |H_{mm} - H_{nn}|$ are given in Fig. 4.7. Since d takes positive values as well, existence of strong coupling between chains is confirmed, which explains localization on two neighboring chains.

Total localization length can be found using general definition previously given. Plots of its dependence on energy of the states is given in Fig. 4.8. For the highest states, when main chains are disordered, it takes values from 5 to 15 rings (Fig. 4.8c-f). These values are slightly higher then the values of the localization length of highest states in the valence band of amorphous P3HT, which is around 5 [79]. This difference is expected, since crystalline P3HT, despite high degree of disorder, is still more ordered than amorphous. In the sense of the hole localization length, effects of disorder in crystalline and amorphous P3HT are similar. Delocalized states (localized on more than 10 rings) start to appear only few hundreds of meV below the top of the valence band. This is in agreement with findings presented in Ref. 89 where DOS and localization length in PBTTT are calculated. Results for the carrier localization orbital density of HOMO levels of crystalline P3HT at 300 K, given in Ref. 87, indicate the presence of both localized (4-10 rings) and weakly (more than 10 rings) localized states. These calculations were performed without alkyl side chains and for isolated main chains. We obtain qualitatively the same results for L_c, since

we find states localized on few rings within a chain and states that are extended over the entire chain. To conclude, our findings agree with previous that wave functions of the highest states in the valence band are localized and that delocalized (or weakly localized) states also exist below these states.

Results for total localization length and L_b are qualitatively similar for the structures with isolated disorder in main chains and with both disorder in main and side chains. Nevertheless, side chains have a significant quantitative effect on electronic properties. This can be seen by comparing the DOS (Fig. 3.8c vs. Fig. 3.8e and Fig. 3.8d vs. Fig. 3.8f), localization length (Fig. 4.8c vs. Fig. 4.8e and Fig. 4.8d vs. Fig. 4.8f) and on-site Hamiltonian elements (Fig. 4.4c vs. Fig. 4.4e and Fig. 4.4d vs. Fig. 4.4f). By comparing the figures one can also see that the effect of side chains disorder is stronger in the shifted than in the aligned structure which happens due to their larger conformation freedom in the shifted structure, as previously discussed. If disorder of side chains is stronger, which is the case on the higher temperatures, it will contribute more to the electronic structure. Therefore, to obtain reliable results, side chains should be included into the calculations.

4.4 Discussion

We now discuss the consequences of our findings about thermal disorder on electrical properties of the material. In small-molecule based organic crystals (SMOCs) the effects of thermal disorder [86] were used to explain the temperature dependence of the mobility where the mobility that decreases with increasing temperature is typically observed. On the other hand, all mobility measurements of P3HT, even for highest quality ordered samples, yield a thermally activated temperature dependence.

Our results suggest that in ordered P3HT there is a spectral region within first 200 meV below the top of the valence band with electronic states localized to just a few rings. In a combined molecular dynamics - electronic structure study in Ref. 87 such states were found to be persistently localized in the sense that their position does not vary over the time on the order of few nanoseconds. Below the spectral region with localized states, there is a region where both localized and delocalized

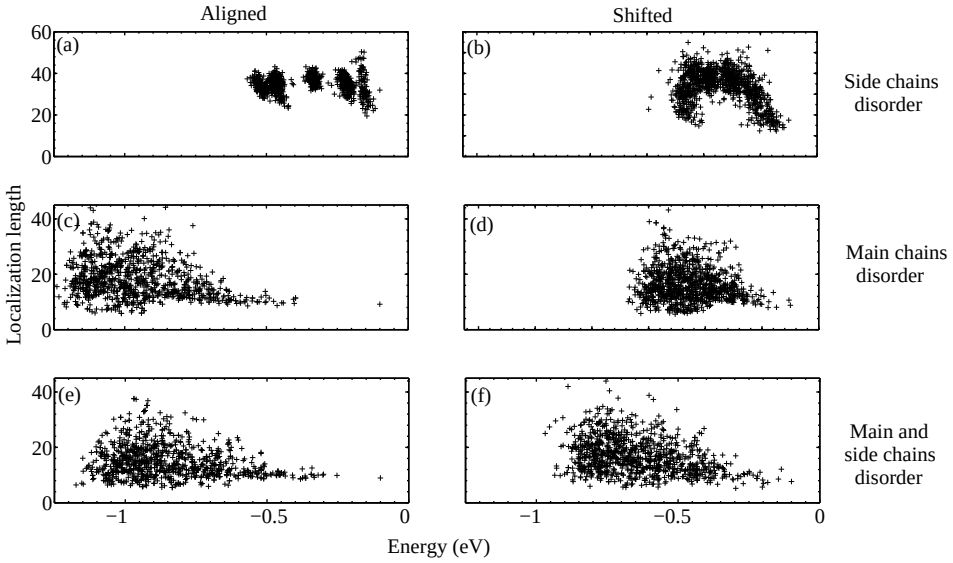

Figure 4.8: Dependence of the total localization length on the energy of the electronic state in the case of: aligned structure with disorder in the side chains; (b) shifted structure with disorder in the side chains; (c) aligned structure with disorder in main chains and side chains omitted; (d) shifted structure with disorder in main chains and side chains omitted; (e) aligned structure with disorder in both side and main chains (f) shifted structure with disorder in both side and main chains.

states exist. It is well understood that the spatial and energetic distribution of electronic states that we obtained leads to thermally-activated transport; at low temperature most carriers populate localized states at the top of the valence band which yield low mobility, while at higher temperatures less localized or delocalized states become more populated and the transport is much better then [104].

However, what is the main difference between polymers and SMOCs where a different temperature dependence of mobility is observed? In SMOCs, thermal disorder leads to localized electronic states, as well. However, the spectral region where these states exist is much narrower. For example, in Ref. 85 the spectral region with strongly localized states has the width of approximately $0.2t$, where t is the electronic coupling transfer integral between two neighboring molecules (which is typically on the order of 100 meV in SMOCs). In Ref. 82 this range is equally narrow and is comparable to or even smaller than thermal energy k_BT at room temperature. For this reason, thermally activated behavior is not observed in SMOCs.

The comparison between the effects of thermal disorder in ordered polymers and SMOCs illustrates the dual role of temperature when thermal disorder and transport properties are concerned. The temperature acts on the one hand to create well localized states and on the other hand to promote the carriers from such localized states to delocalized states with better transport. In SMOCs higher temperatures lead to better localization of the states and consequently to a smaller mobility. On the other hand, in ordered P3HT polymers, in the range of temperatures from 100K to 300K, the temperature has a weak effect on the electronic density of states and on the dependence of localization length on energy. This conclusion was obtained from the comparison of these two quantities at 100K and 300K, presented in Fig. 4.9. A weak effect of temperature on the degree of localization was also shown in Ref. 87 (Table I). Therefore, the temperature dependence of mobility in ordered polymers originates from thermal activation of carriers from localized states to delocalized or less localized states with better transport.

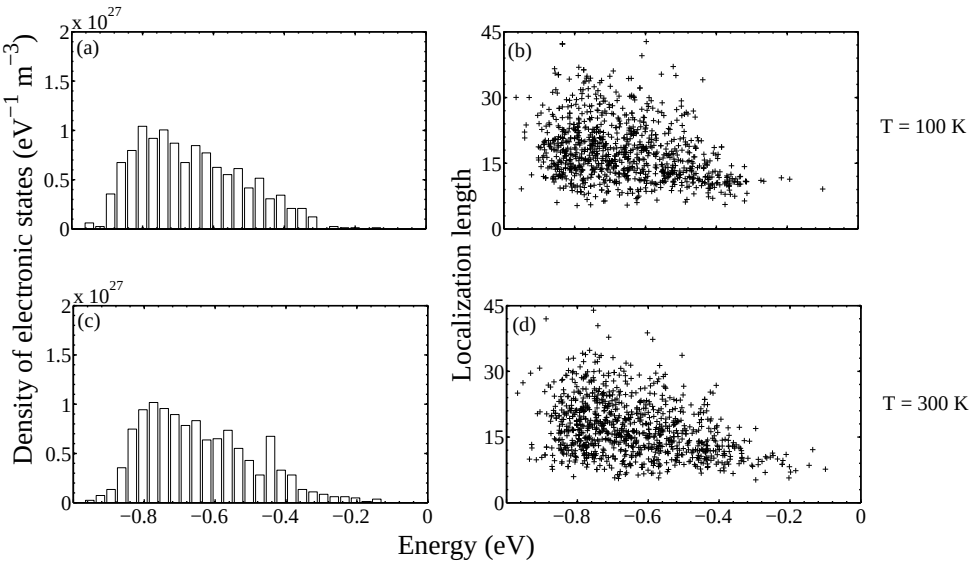

Figure 4.9: (a) DOS of the shifted structure with disorder in main and side chains at 100 K. (b) Dependence of the total localization length on the energy of the electronic state of the shifted structure with disorder in main and side chains at 100 K. (c) DOS of the shifted structure with disorder in main and side chains at 300 K. (d) Dependence of the total localization length on the energy of the electronic state of the shifted structure with disorder in main and side chains at 300 K.

Chapter 5

Electronic states at the interfaces between crystalline and amorphous domains in conjugated polymers

5.1 Introduction

Understanding the electronic and transport properties of conjugated polymers is the precondition for the enhancement of their performance. On the other hand, electronic structure of a material is strongly affected by its atomic structure. Conjugated polymers exhibit complex structure: they contain both crystalline (ordered) and amorphous (disordered) domains [22,23]. While the electronic structures of single crystalline and single amorphous domains are well understood, there is a lack of knowledge about the electronic structure of the interface between these two regions.

In real conjugated polymers, amorphous and crystalline domains are interlaced. According to previous works [22, 23, 105, 106], it is believed that a single polymer chain typically spreads across both amorphous and crystalline domains. There are three types of such chains: bridge chains, which connect different crystalline regions through an amorphous region; folded chains, which connect different parts

of the same crystalline domain and extended chains, which are extended out from crystalline and have their end in the amorphous domain [22, 23]. However, chains can also be entirely localized in the crystalline or amorphous domain. Amorphous domains have larger band gap than crystalline due to reduced electronic coupling between monomer units [22–25]. Differences in band gaps produce band offsets in the valence and conduction band between crystalline and amorphous domains. Offset in the valence band acts as a barrier for a hole to jump from crystalline domain into amorphous [21, 22, 25, 107]. In all previous works, amorphous and crystalline domains in conjugated polymers were investigated separately and the effects of the interface between these two domains were not explicitly taken into account.

To fully understand electronic properties of conjugated polymers, calculations which include both crystalline and amorphous domains are needed. In this chapter we perform such calculations and obtain microscopic insights into the electronic states at the interface between crystalline and amorphous regions in P3HT. We consider two types of interface that we call type A and type B. Type A interface is a sharp interface between an amorphous and an ordered domain where P3HT chains belong exclusively to one of these regions, as shown in Fig. 5.1a. Such type of interface is an idealization that is highly suitable to investigate the difference between ordered and disordered regions. On the other hand, it is unlikely that a realistic interface is that sharp. Therefore, we additionally consider type A' interface where an intermediate region exists between the ordered and amorphous region (Fig. 5.1b). Type B interface consists of two ordered domains whose chains extend into the region between them and form an amorphous region (Fig. 5.1c). It is believed that this type of interface is a reasonably good representation of interfaces that exist in real materials [22, 23].

In this chapter, we mainly investigate the energy level alignment between the states in the two regions and the possibility of having interface trap states within the band gap of the material. For all interface types we model the ordered region as an ideal crystal. Realistic ordered regions are not perfect crystals and exhibit the effects of thermal (dynamical) disorder and paracrystallinity. In the prevous chapter, we showed that the effects of thermal disorder produce variations of the

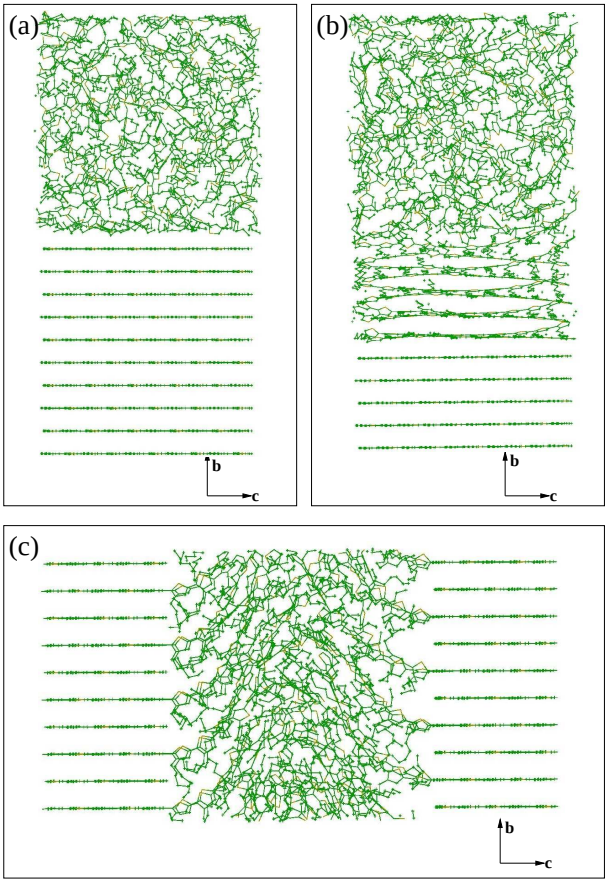

Figure 5.1: Atomic structures of interfaces considered in this work: (a) type A; (b) type A' and (c) type B.

energy levels in the valence band on the order 0.1 - 0.2 eV and therefore we do not include them in this work. Along the same line, we do not expect that the effect of paracrystallinity, when it is reasonably small, will change the main conclusions of our work.

Our results indicate that wave functions of HOMO states are delocalized and belong to ordered domains, regardless of the interface type. Localized states in disordered domains start to appear at the energies few hundreds meV below HOMO in the case of realistic type B interface. In the case of sharp type A interface, difference between HOMO levels in crystalline and amorphous domains is even larger. Additionally, there is no evidence of the existence of states belonging to both domains. Therefore, disordered regions present barriers for hole transport which consequently dominantly goes through crystalline regions.

5.2 Methodology

Atomic structure of the interface between ordered and disordered region was generated using in-house developed MC simulations [30], while electronic structure was calculated using CPM [39] and OFM [40]. These methods were described in detail in Chapter 2. Therefore, in this section we focus on the description of the procedure for generating the atomic structure, which is significantly different to that used for thermally disordered P3HT, considered in the previous chapter.

During MC simulations crystalline domains were kept rigid. There are several types of crystalline structures reported in the literature [93, 95, 108]. We chose the shifted structure (neighboring chains in the π - π stacking direction mutually shifted by a half of the unit cell in the main chain direction) with interdigitated side chains as representative, since it was shown that this structure is energetically favorable [93, 108]. Lattice constants were obtained from NPT (constant pressure and temperature) MC simulations at zero temperature and pressure of 101.325 kPa, using the OPLS parameters set [31, 87] for non-bonded interactions. These lattice constants are: $a/2 = 15.55$ Å, $b = 8.1$ Å and $c = 7.77$ Å.

The procedure for generation of amorphous domains is different for type A and

B interfaces. In the case of type A interface, at the beginning, P3HT chains were randomly placed in the simulation box which was significantly larger than the final. The box was gradually compressed until the density of amorphous P3HT reached its experimental value of around 1.1 g/cm^3 [109]. Type A' interface was generated using the same atomic configuration as for the type A interface, with a difference that several chains in the crystalline domain closest to the amorphous region were allowed to move freely. For type B interface two different starting configurations were used: one with interdigitated backbone chains and the other where backbone chains were separated by a predefined distance in the backbone direction (denoted as c-direction in figures). In this case, simulation box was compressed only in the backbone direction until the density in the amorphous region between crystalline domains reached its experimental value. For all types of interfaces, the temperature of 1000K was used in MC simulations. At the end, when the final density of the amorphous region is reached, the system was cooled down to 0 K. By keeping crystalline structure rigid and by cooling the amorphous structure, effects of thermal disorder [108] were excluded, to keep focus on the difference between crystalline and amorphous region. Energy of the system in MC simulations was modeled as a sum of non-bonded van der Waals and Coloumb interactions and interring torsion potentials. OPLS parameter set was used for non-bonded interactions and torsion potentials of dihedrals within side chains, while thiophene-thiophene torsion potential was taken from Ref. 24. Periodic boundary conditions were applied in all directions. Each of the obtained interface atomic structures contains around 10000 atoms.

5.3 Results

As explained, type A interface is a sharp interface between crystalline and amorphous region where each chain belongs to one of these regions. Both regions in the structures that we simulated contain 20 P3HT chains, each 10 thiophene rings long. In the crystalline region, the chains are arranged in 2 lamellas, where one lamella contains 10 chains stacked in the π-π direction (denoted as b-direction in

figures). We have calculated energies and wave functions of the electronic states in the valence band for 4 different random realizations of the system. The results that were obtained are similar for all realizations and indicate that 3 different types of electronic states exist: (1) delocalized states in the crystalline domain (Fig. 5.2a), (2) localized states at the edge of the crystalline domain (Fig 5.2b) and (3) localized states in the amorphous domain (Fig. 5.2c). Highest states are delocalized and belong to the crystalline domain. These states have highest energies due to the strongest electronic coupling between thiophene rings (both inter- and intra-chain coupling). Localized states in the crystalline domain start to appear at energies of around 0.4 eV below HOMO. These states are localized at P3HT chains which are nearest to the amorphous region. Diagonal Hamiltonian elements of the rings nearest to the interface are smaller than diagonal Hamiltonian elements of the rings far from the interface, which can be clearly seen from the distribution of the diagonal Hamiltonian elements across b-direction, given in inset of Fig. 5.2c. Values of the elements are obtained by averaging the diagonal Hamiltonian elements of the rings that have the same b-coordinate. Consequently, such states have lower energies than the energy of delocalized HOMO state. Localized states are not possible in ideal crystalline domains which are periodic in all crystallographic directions. Therefore, localized states in the crystalline domain near the interface are induced by the interface. Finally, localized states in the amorphous domain start to appear at the energies around 1 eV below HOMO. These states fully resemble the states in purely amorphous P3HT [24, 79].

Band offsets of HOMO and LUMO levels between amorphous and crystalline domains were estimated from local density of states (DOS), given in Fig. 5.3 for one realization of the structure for each interface type. Values of offsets can vary up to 0.2 eV depending on the structure. According to Fig. 5.3a, HOMO band offset for type interface A is around 1 eV. On the other hand, LUMO in the amorphous domain has similar energy as LUMO in the crystalline domain. It is usually assumed that HOMO and LUMO offsets are equal to the half of the band gap difference between crystalline and amorphous domain. According to previously reported results, this offset is expected to be in the range of 0.1 - 0.3 eV [22, 24, 25, 107]. Our results

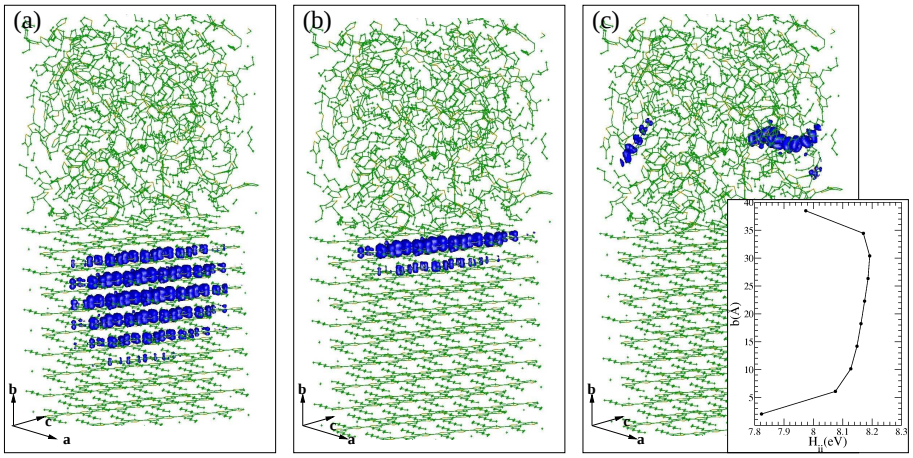

Figure 5.2: Wave function moduli squared of the (a) highest electronic state in the valence band in the crystalline domain, (b) localized electronic state in the valence band in the crystalline domain and (c) highest electronic state in the valence band in the amorphous domain in the case of type A interface. The inset shows the distribution of the averaged diagonal Hamiltonian elements in the crystalline domain along b-direction. Isosurfaces correspond to the probability of finding a hole inside the surface of 75%.

indicate that the presence of disordered domain affects the energy levels in crystalline domains. This can be clearly seen from the distribution of diagonal Hamiltonian elements from different chains in crystalline region (inset of Fig. 5.2c). Difference between the diagonal Hamiltonian elements of the rings furthest from the interface and the rings closest to the interface is around 0.3 eV. Therefore, energy levels in the crystalline domain far from the interface are shifted by approximately 0.3 eV toward higher energies. This shift leads to an increase in HOMO band offset and a decrease in LUMO band offset in comparison to the offsets estimated as half of the band gap difference. The shift may originate from uneven charge distribution at the interface between ordered and disordered chains.

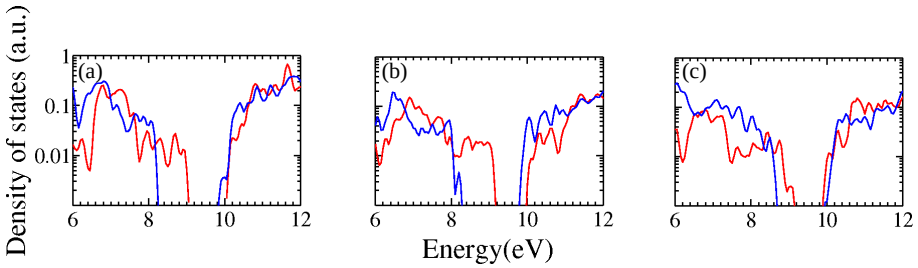

Figure 5.3: Density of electronic states (arbitrary units, logarithmic scale) of crystalline (red) and amorphous (blue) region in the case of (a) type A interface; (b) type A' interface and (c) type B interface.

Intermediate region between amorphous and crystalline region (type A' interface) presents a more realistic interface model than the sharp interface. In our simulation it consists of 5 P3HT chains and there is the same number of chains in crystalline region. As expected, chains closer to the crystalline region are well-ordered and chains closer to the amorphous region are more disordered (Fig. 5.1b). The main difference between electronic structures of type A and A' interfaces is in the localization lengths of the states in the ordered domains. Wave function of HOMO state of the type A' interface is delocalized (Fig. 5.4a), but with significantly lower localization length than HOMO state of the interface type A due to disorder in the intermediate domain. Highest states in the perfectly ordered domains (Fig. 5.4b) have energies only few meV below HOMO. Difference between HOMO state and highest localized

states in the amorphous domain (Fig. 5.4c) is around 1 eV (Fig. 5.3b), similar as in the case of sharp interface.

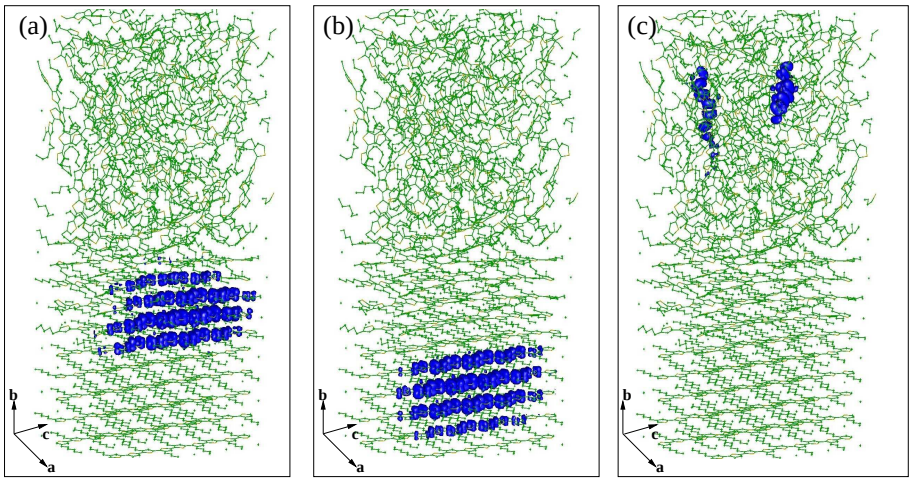

Figure 5.4: Wave function moduli squared of the (a) highest electronic state in the valence band in the intermediate domain, (b) highest electronic state in the valence band in the crystalline domain and (c) highest electronic state in the valence band in the amorphous domain in the case of type A' interface. Isosurfaces correspond to the probability of finding a hole inside the surface of 75%.

Type B interface is composed of 20 chains, where each chain contains 20 thiophene rings. Half of the rings in each chain belong to the amorphous, other half to the crystalline region. Results for the hole wave functions and energies were extracted from 8 different realizations (4 for each starting structure). We have found that in such structure two types of states exist: (1) delocalized states in crystalline domain (Fig. 5.5a) and (2) localized states in amorphous domain (Fig. 5.5b). HOMO state is completely delocalized in the ordered domain. Localized states start to appear at the energies around 0.4 eV below HOMO (Fig. 5.3c). This result is more in-line with previous expectations due to the fact that this interface type is more realistic, contrary to the sharp type A interface. Wave functions of the states can leak slightly from crystalline domain to amorphous and vice versa, but they are dominantly localized in one of them. Interestingly, states in the amorphous domain can be localized on two chains, which can be explained by the presence of some degree of ordering between disordered chains.

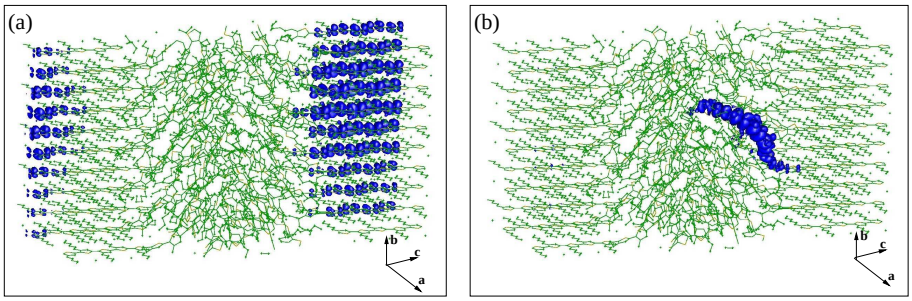

Figure 5.5: Wave function moduli squared of the (a) highest electronic state in the valence band in the crystalline domain and (b) highest electronic state in the valence band in the amorphous domain in the case of type B interface. Isosurface correspond to the probability of finding a hole inside the surface of 75%.

5.4 Discussion

Our results indicate that the interface between amorphous and crystalline domain does not introduce trap states in the band gap of crystalline domain. This is a generally positive feature, having in mind that the presence of such trap centers would deteriorate charge mobility. Moreover, there are no states which belong to both domains. These results are qualitatively different from the results for the electronic structure of grain boundaries between misaligned naphthalene crystals, given in Chapter 3. At the grain boundaries in polycrystalline naphthalene there are points of both stronger and reduced electronic coupling between molecules. States localized at the points of strong electronic coupling act as traps. On the other hand, electronic coupling between chains in amorphous and crystalline domains in P3HT is always smaller than the coupling between chains in crystalline domains. This coupling is even not able to form the states which belong to both domains. The only type of states which are in some way induced by the interface are localized states at the edge of crystalline domains in type A interface. In type B interface similar states do not exist, because the drop in the electronic coupling between the rings in the direction perpendicular to the plane of the interface is not that high. In the next chapter we consider type C interface, where interface surface between single crystalline and single amorphous domains is perpendicular to the backbone

direction. For such kind of interface, spontaneous polarization in P3HT, the subject of the next chapter, has significant effect on electronic structure.

Chapter 6

Spontaneous polarization in ordered poly(3-hexylthiophene) induced by side chains

6.1 Introduction

As pointed out in the previous chapter, conjugated polymers have complex structure composed of mixed amorphous and crystalline domains. Therefore, it is important to take into account all significant effects that take place at the interfaces between different materials or between different domains of the same material. At the interfaces, the effects of spontaneous polarization in materials can play an important role.

Spontaneous polarization is an intrinsic property of a material that it exhibits in the absence of external electric field and occurs in crystals that do not have a center of inversion symmetry, as explained in Sec. 2.7. There are many materials that are known to have high values of spontaneous polarization, such as some oxides, nitrides, etc [47,48,52,110]. Within the class of conjugated polymers, polyvinylidene fluoride (PVDF) is reported to have the highest spontaneous polarization of 0.1-0.2 C/m^2 [111].

Despite the fact that P3HT serves as a model conjugated polymer and that it has been widely investigated, the effects of spontaneous polarization in this material

have not been discussed before. In this chapter, the importance of spontaneous polarization in ordered regioregular poly(3-hexylthiophene) (P3HT) is pointed out. We show that this effect arises from head-to-tail side chain arrangement which breaks the symmetry along the backbone chain. Firstly, we have calculated spontaneous polarization of ideally crystalline P3HT using density functional theory (DFT) [35] and modern theory of polarization. Next, we demonstrate that the effects of thermal disorder reduce this polarization but still keep it at significantly large value. Finally, we discuss the effects of spontaneous polarization in crystalline P3HT on electronic properties of the interface between crystalline and amorphous P3HT where the interface is perpendicular to the backbone direction of P3HT chain.

6.2 Methodology

Spontaneous polarization of an ideal crystal can be calculated using modern polarization theory as implemented in several DFT-based computer codes. To calculate the effective polarization in a thermally disordered structure, calculations of systems involving a large number of atoms are required. Standard DFT-based codes are limited to several hundreds of atoms and cannot be used for such systems. Alternative way to extract the polarization of the material is from the calculation of electric fields in the system consisting of alternating layers of the material and vacuum. Let us consider such a system consisting of a material with spontaneous polarization P_s along x-direction and vacuum, as shown in Fig. 6.1. Polarization in dielectric medium is given by formula:

$$\mathbf{P} = \mathbf{P_s} + \epsilon_o \chi \mathbf{E}, \tag{6.1}$$

where ϵ_o is the electric permittivity of vacuum, χ is the electric susceptibility of material and $\mathbf{E}$ is the electric field in material. From the definition of the electric displacement vector, it follows that:

$$\mathbf{D} = \epsilon_o \mathbf{E} + \mathbf{P}, \tag{6.2}$$

while the Maxwell equation for **D** reads

$$\oint_S \mathbf{D} \cdot \mathbf{dS} = \rho. \tag{6.3}$$

If we assume that there is no free charge at the interface between material and vacuum ($\rho = 0$), we obtain the equation $D_1 = D_2$ for the x-projections of the electric displacement vector in material and vacuum, respectively. Using Eq. 6.1 and 6.2, we then obtain:

$$P_s = \epsilon_o E_2 - \epsilon_o \epsilon_r E_1, \tag{6.4}$$

where ϵ_r is the relative permittivity of material. Hence, spontaneous polarization can be easily obtained with known electric fields in material and vacuum, which can be calculated as electrostatic potential derivatives.

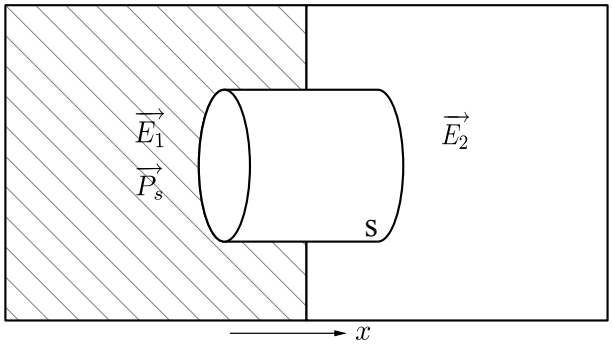

Figure 6.1: Sketch of the interface between a material with spontaneous polarization and vacuum.

6.3 Spontaneous polarization of ideally crystalline P3HT

Spontaneous polarization of ideally crystalline P3HT was calculated using DFT as implemented in ABINIT [49–51, 112] and Quantum ESPRESSO packages [50, 113]. We used norm-conserving pseudopotentials with LDA expression for the exchange-correlation term. There are several crystalline structures of P3HT reported in the literature [92–101, 114]. We have considered the aligned structure (Fig. 6.2a), where

chains are mutually aligned in the π - π stacking direction (b-direction, not shown in Fig. 6.2). Unit cell parameters for this structure at 0 K, obtained from energy minimization calculated using classical potentials [31], are: $a = 15.55$ Å, $b = 4.1$ Å , $c = 7.77$ Å and all angles are 90° [108]. The obtained value for the spontaneous polarization in the backbone direction from both calculations is $6.0 \cdot 10^{-3}$ C/m^2. In the other two directions spontaneous polarization is 0. We have additionally checked that the value of spontaneous polarization in the backbone direction remains almost the same upon the structure relaxation. For comparison, spontaneous polarization in nitrides (GaN, InN, AlN) takes values from 2.9 to $8.1 \cdot 10^{-2}$ C/m^2 [52], while $BaTiO_3$ has one of the highest reported spontaneous polarization of around 0.9 C/m^2 [110].

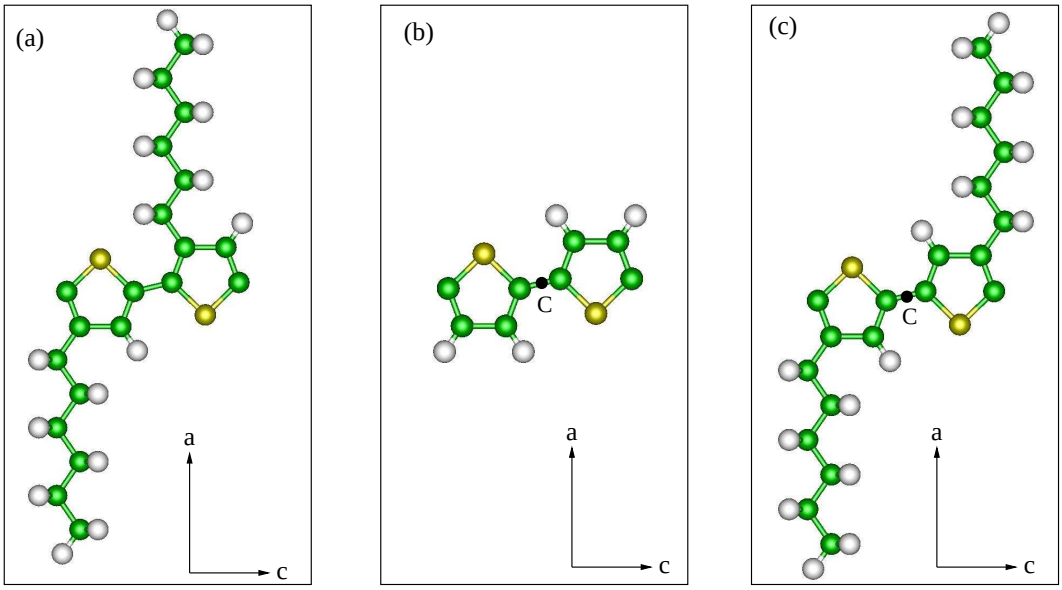

Figure 6.2: (a) P3HT unit cell with head-to-tail side chains arrangement, (b) PT unit cell, (c) P3HT unit cell with tail-to-tail side chains arrangement.

To understand the origin of the spontaneous polarization in the backbone direction, we have calculated the polarization in that direction for the structure without side chains, which is actually polythiophene (PT), shown in Fig. 6.2b. This structure does not have spontaneous polarization in the backbone direction. Additionally, we considered the P3HT unit cell with tail-to-tail side chains arrangement (Fig. 6.2c). This structure does not show pyroelectric properties as well. Therefore, we have concluded that spontaneous polarization in the first unit cell arises from head-to-

tail arrangement of side chains. Atoms in side chains do not have their inversion symmetry pairs, which breaks the symmetry. On the other hand, structures shown in Fig. 6.2b and Fig. 6.2c exhibit inversion symmetry where each atom has its corresponding pair.

Structures with head-to-head and tail-to-tail side chains arrangement are not regioregular and they are not able to form well-ordered crystalline structure. Therefore, crystalline structure with head-to-tail arrangement of side chains is more representative. Regarding different types of P3HT unit cells, we expect that each unit cell with the lack of the inversion symmetry would have nonzero spontaneous polarization. To check this, we have calculated spontaneous polarization in the shifted structure of P3HT that we considered in previous chapters. The calculated spontaneous polarization in the backbone direction is $6.2 \cdot 10^{-3}\ C/m^2$, which is nearly the same to that for aligned structure. Therefore, we conclude that spontaneous polarization is robust upon the structure change if the asymmetric arrangement of side chains is preserved. Recently, P3HT unit cell with $P2_1/c$ symmetry group was proposed [114]. This symmetry group is centrosymmetric and spontaneous polarization in this structure is not expected to occur.

To check the reliability of the alternative method for spontaneous polarization calculation described in the previous section, we have calculated the electrostatic potential along the backbone direction in the supercell that consists of 10 thiophene rings long rigid P3HT chain and a vacuum region of the same length as P3HT chain. This potential is shown in Fig. 6.3. Within the material, potential is periodic with additional linear trend arising from the electric filed caused by spontaneous polarization. The peaks of this potential correspond to atom positions. Electric field in P3HT was calculated as a negative derivative of the envelope that connects the peaks. In vacuum, the potential is linear and electric field is calculated as its negative derivative. The relative permittivity of P3HT is taken to be 4.0 [115]. Using Eq. 6.4 calculated polarization is $5.6 \cdot 10^{-3}\ C/m^2$, which is very close to the value obtained using DFT-based codes and modern theory of polarization.

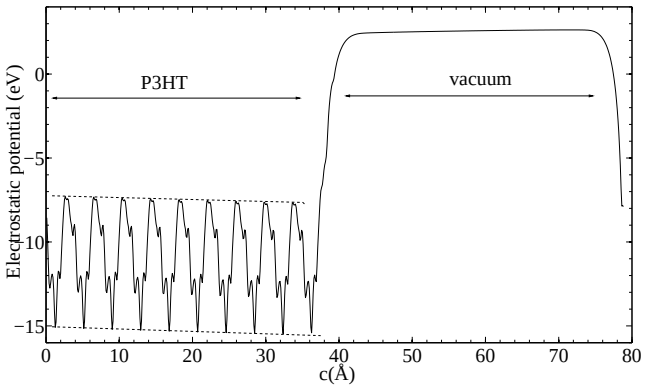

Figure 6.3: Electrostatic potential along rigid P3HT chain and vacuum. This potential is one-dimensional, obtained from three-dimensional potential by averaging in other two dimensions.

6.4 Spontaneous polarization of thermally disordered P3HT

Next, we consider the effects of temperature on polarization of P3HT. At non-zero temperature the atoms are displaced from their equilibrium positions and periodicity of the structure is broken. This effect is known as thermal or dynamic disorder and is significant in conjugated polymers [22, 87, 90, 91, 108]. Side chains of P3HT are more disordered than backbone chains. It is expected that spontaneous polarization induced by side chains is lower at finite temperature than in perfectly ordered chain. We used the structures that we produced to investigate the effects of thermal disorder in P3HT [90,108]. Each of the structures contains 2520 atoms arranged in 10 chains. Due to high number of atoms, electrostatic potential cannot be extracted from DFT-based codes. We instead applied the DFTB+ code [116], which is based on DFTB method [44], explained in Sec. 2.6. To check if DFTB+ gives the same results as ABINIT or Quantum ESPRESSO, we have calculated electrostatic potential for the structure we used to test the method for the spontaneous polarization calculation. This potential (shown in Fig. 6.4 with dashed line) was calculated as Coulomb potential from the point charges at atom positions, where the charge of an atom is a sum of its ion and electron charges. Obtained potential differs from the potential

obtained by DFT-based codes in two ways: (1) it does not contain the exchange-correlation term and (2) atoms are modeled as point charges which is not the case in DFT-based codes. These two differences result in the potential shift and its amplitude oscillations reduction in the P3HT domain. However, potential shape and electric fields in P3HT and vacuum remained almost the same, which resulted in the spontaneous polarization of $6.3 \cdot 10^{-3}\ C/m^2$. Therefore, DFT-based codes can be replaced by the DFTB+ code to calculate the spontaneous polarization for large systems.

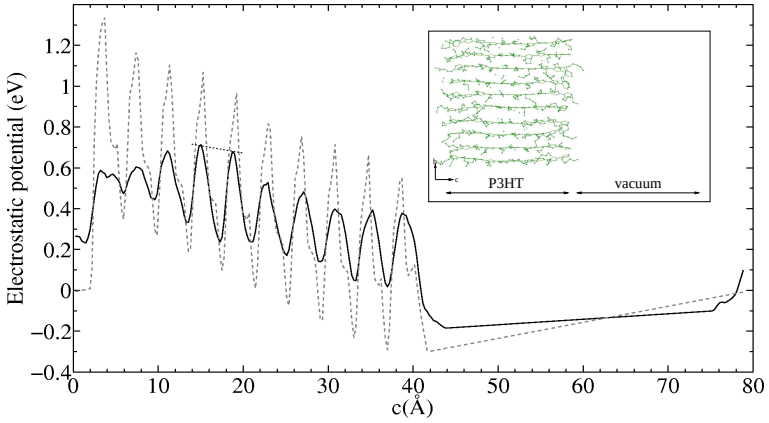

Figure 6.4: Averaged electrostatic potential along the interface of disordered P3HT chain and vacuum at 300K (solid line) and at 0K (dashed line). The inset shows the structure used to calculate the potential along the interface of thermally disordered P3HT and vacuum.

Averaged electrostatic potential along backbone direction of P3HT at 300K for one structure is shown in Fig. 6.4. Potential envelope within P3HT domain is not unique as for rigid chains. Consequently, the choice of the envelope would affect the obtained value for electric field and spontaneous polarization. To avoid this issue, we took several different structures and calculated averaged electric field. The electric field is calculated in the middle of chains in order to exclude the effects of higher disorder present at the chain edges. The calculated value of polarization is $3.6 \cdot 10^{-3}$ C/m^2, which is lower than for rigid chain. However, this value is significant and shows the important feature that spontaneous polarization in ordered P3HT exists even at room temperature. Spontaneous polarization is expected to vanish only for

completely disordered chains, as in amorphous domains.

Electrostatic potential in vacuum is linear and there is no uncertainty of the value for corresponding electric field. It would be interesting to compare the values for the electric field for structures with rigid and thermally disordered chains since the spontaneous polarization is linearly dependent on the electric field in vacuum (Eq. 6.4). The value for the electric field in vacuum for the structure with the rigid chain is $8.0 \cdot 10^7 V/m$, while the corresponding value for thermally disordered chains (averaged over different structures) is $3.4 \cdot 10^7 V/m$. The ratio between these electric fields is close to the ratio between spontaneous polarizations for corresponding structures. Therefore, electric field in vacuum can be used as a good measure for the estimation of the effect of thermal disorder on the spontaneous polarization in conjugated polymers.

Next, we estimate possible effect of spontaneous polarization in P3HT on characteristics of P3HT/fullerene blends relevant for solar cell applications. In P3HT/fullerene based heterojunctions characteristic length of each domain is on the order of 10 nm. If we assume that layers of P3HT and C60 are arranged in an ideal superlattice where each domain is 10 nm long and that P3HT polarization is perpendicular to the domain interface, we obtain potential drop in C60 domain of around 0.9 V at low temperature and around 0.5 V at room temperature (relative permittivity of C60 is taken to be 3.6 [117]). These are significant values of potential drop that should strongly affect the performance of bulk heterojunction - based devices. While the superlattice model is certainly a simplification of real bulk heterojunction, it demonstrates the importance of the effect of spontaneous polarization and one should expect potential drop of the same order of magnitude in real bulk heterojunctions.

6.5 Effects of spontaneous polarization on electronic states at the interface between crystalline and amorphous P3HT

Realistic conjugated polymers contain both crystalline and amorphous domains. Average spontaneous polarization in an amorphous domain is 0 due to random orientation of dipoles. If spontaneous polarization exists in a crystalline domain, there is a discontinuity of the polarization at the interface between crystalline and amorphous domain, analogously to the interface between material with spontaneous polarization and vacuum shown in Fig. 6.1. Hence, there is a surface charge density at the end of the crystalline domain induced by spontaneous polarization, which affects the energy levels in both domains.

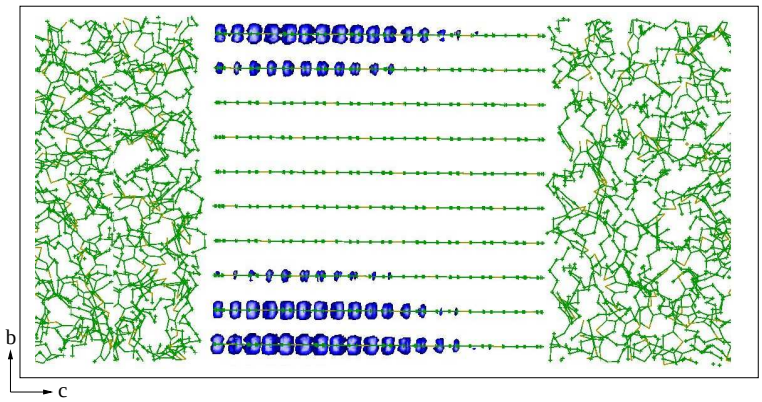

Figure 6.5: Wave function moduli squared of the highest electronic state in the valence band of the type C interface. Isosurfaces correspond to the probability of finding a hole inside the surface of 75%.

In the previous chapter we have investigated the electronic states at the interface between crystalline and amorphous domains in P3HT where we found that highest states in the valence band were delocalized and belonged to crystalline domain. We have investigated two interface types: (1) sharp interface between crystalline and amorphous domain where interface surface is perpendicular to the π-π stacking direction (type A interface) and (2) more realistic interface composed of chains

extended from crystalline into amorphous domain in the backbone direction (type B interface). In the case of type A interface, spontaneous polarization in P3HT does not have any influence on electronic states as there is no spontaneous polarization along the π-π stacking direction. On the other hand, in the case of type B interface, spontaneous polarization effects exist but they are relatively weak as the consequence of soft transition from ordered to disordered chains. Such transition corresponds to slow spontaneous polarization decline form P_s to 0. Now, we investigate the effects of spontaneous polarization in the backbone direction on the electronic states at the interface between crystalline and amorphous domains where the interface surface is perpendicular to the backbone direction (type C interface). Following the same procedure as in the previous chapter, the amorphous structure was generated by Monte Carlo simulation by compressing the large box until the density of amorphous domain reached experimental value of 1.1 g/cm^3. To calculate the electronic structure for obtained atomic structure, DFTB+ code was used. As expected, wave function of the highest state in the valence band (Fig. 6.5) is delocalized and belongs to the crystalline domain. However, due to spontaneous polarization in the backbone direction, the state is confined at one side of the crystalline domain. As one may notice, this interface type is sharp and hence not very realistic. To build a more realistic interface model, effects of thermal disorder and disorder at the crystalline domain edges should be included. We have shown above that spontaneous polarization does not vanish with thermal disorder. Additionally, we have shown in the previous chapter that the introduction of intermediate region between ideal crystalline and amorphous regions (referred to interface type A') does not qualitatively change the results. Based on these two conclusions, we expect that localization of the wave function at one side of the crystalline domain would be present even in the realistic model. This effect will be completely absent only in the case of centrosymmetric P3HT structure, as that proposed in Ref. 114. Therefore, spontaneous polarization can significantly affect electronic properties of conjugated polymers.

Chapter 7

Summary

The aim of this work was to elucidate the electronic properties of the interfaces in realistic organic semiconductors from the theoretical point of view. The main results can be summarized as follows:

(1) Grain boundaries in polycrystalline small-molecules organic semiconductors introduce localized trap states at the points of strong electronic coupling. However, they can act as barriers for delocalized states.

(2) Thermal disorder has a significant effect on the electronic states of conjugated polymers: the disorder of main chains localizes charge carriers on few, mostly two neighboring chains.

(3) Highest states in the valence band of conjugated polymers belong to crystalline domains, making the amorphous domains barriers for charge transport.

(4) Spontaneous polarization in P3HT arising from head-to tail side chains arrangement is significant. This effect is pronounced at the interfaces between crystalline and amorphous domains in P3HT or between P3HT and other materials.

Now let us review the results in more detail. Chapter 1 was an introductory to organic semiconductors, providing an overview of transport models and putting special attention on electronic coupling, which is important for electronic properties of organic semiconductors. In Chapter 2 we explained the methods used for atomic and electronic structure calculation. Firstly, MC method was explained in detail, making the references with fundamentals of statistical physics. Then, the overview of DFT method and related extensions (CPM, OFM, DFTB) was given. Finally,

modern polarization theory was introduced.

In Chapter 3 we have introduced the methodology for the calculation of electronic states at grain boundaries in small-molecule based organic semiconductors. We focused our study on low-angle grain boundaries, since our results indicated that they have lower energies than high-angle grain boundaries. The results indicate that grain boundaries introduce trap states within the band gap of the material. Wave functions of these states are localized on pairs of molecules from opposite sides of the boundary whose mutual distance is smaller than the distance between two adjacent molecules in a monocrystal. Strong electronic coupling between the orbitals of the two molecules is responsible for the creation of trap state. While naphthalene, BTBT and ditBu-BTBT molecules were used in our study, we expect that the origin of trap states will be the same in any other small molecule based organic semiconductor since electronic coupling as a mechanism of trap state creation is present in any other material from this class. The energy of the trap state was found to correlate to the distance between two molecules which create the trap. This correlation was then used to calculate the electronic density of trap states solely based on geometrical arrangement of molecules near the boundary. This approach was exploited to calculate the density of trap states for different boundaries and estimate the number of trap states per unit of volume in a real polycrystal. This number is significant and may consequently reduce the carrier mobility and deteriorate the performance of devices based on polycrystalline organic semiconductors. The next step in the understanding of grain boundaries in small-molecule organic semiconductors would be the calculation of transport properties across grain boundary.

In Chapter 4 the effects of thermal disorder on the electronic structure of crystalline P3HT were investigated. The influence of side chains and main chains on the thermal disorder were investigated separately for the first time. The main conclusions from the obtained results can be summarized as follows. The disorder in side chains has a relatively weak effect on the electronic structure of P3HT. The effect is more pronounced in the shifted structure than in the aligned, due to higher conformational freedom of side chains. The disorder in main chains has a stronger effect on the electronic structure than the disorder in side chains, where the effect is

equally pronounced in aligned and shifted structures. The disorder in main chains is sufficient to cause localization of HOMO levels wave functions to few rings only. Such a degree of localization is similar to the localization in amorphous P3HT and it is likely the cause of thermally activated mobility that is typically observed in ordered polymers.

In Chapter 5 electronic states at the interface between crystalline and amorphous domains in P3HT were investigated. We have considered two different interface types: sharp interface and more realistic interface that consists of extended chains. Results can be summarized as follows. Highest states in the valence band are delocalized in the crystalline domains for both interface types. Highest states in the amorphous domains are localized on one or two chains, as in the case of single amorphous domain. Amorphous domain presents a barrier for hole transport due to high energetic offset between highest states in the crystalline and in the amorphous domain. This offset is comparable to other reported results in the case of interface that consists of extended chains. In the case of sharp interface, this offset is larger due to the energy levels shift in the crystalline domain. Importantly, we find that none of the investigated interfaces leads to formation of trap states at the interface. These results indicate that in conjugated polymer materials charge transport takes place through crystalline domains. While our results indicate that amorphous domains present barriers for charge transport, we note that paths for fast charge transport through the amorphous domain could exist if well-ordered bridging chains connect the crystalline domains through the amorphous domain, as proposed in Ref. 22. Future directions in this topic are transport calculations of the interface between crystalline and amorphous domains and the construction of macroscopic model of realistic conjugated polymers.

Finally, in Chapter 6 we have shown the existence of spontaneous polarization along the backbone chain in ordered P3HT. This effect is caused by inversion symmetry breaking arising from head-to-tail arrangement of side chains. We proposed the method to calculate spontaneous polarization in large and realistic systems. Then, we applied the method to calculate spontaneous polarization for disordered crystalline P3HT at 300K and showed that spontaneous polarization is still signif-

icant at room temperature. Effects of spontaneous polarization are important at the interfaces between materials with different spontaneous polarization. We have demonstrated that spontaneous polarization confines the hole states at one side of crystalline domain of P3HT in the presence of the interface between crystalline and amorphous domain. In organic solar cells at the interfaces between different materials electric field caused by spontaneous polarization can assist or hinder charge separation, depending on the relative orientations of polarization vectors. The procedure for calculating the spontaneous polarization in P3HT can be applied for any organic semiconductor and for difference interfaces that occur in realistic organic semiconductors.

Bibliography

[1] D. L. Cheung and A. Troisi, "Modelling charge transport in organic semiconductors: From quantum dynamics to soft matter," *Phys. Chem. Chem. Phys.*, vol. 10, pp. 5941–5952, 2008.

[2] R. H. Friend, R. W. Gymer, A. B. Holmes, J. H. Burroughes, R. N. Marks, C. Taliani, D. D. C. Bradley, D. A. D. Santos, J. L. Bredás, and M. Logdlund, "Electroluminescence in conjugated polymers," *Nature*, vol. 397, pp. 121–128, 1999.

[3] J. H. Burroughes, D. D. C. Bradley, A. R. Brown, R. N. Marks, K. Mackay, R. H. Friend, P. L. Burns, and A. B. Holmes, "Light-emitting diodes based on conjugated polymers," *Nature*, vol. 347, pp. 539–541, 1990.

[4] V. L. Colvin, M. C. Schlamp, and A. P. Alivisatos, "Light-emitting diodes made from cadmium selenide nanocrystals and a semiconducting polymer," *Nature*, vol. 370, pp. 354–357, 1994.

[5] A. Dodabalapur, L. Torsi, and H. E. Katz, "Organic transistors - 2-dimensional transport and improved electrical characteristics," *Science*, vol. 268, pp. 270–271, 1995.

[6] G. Li, V. Shrotriya, J. S. Huang, Y. Yao, T. Moriarty, K. Emery, and Y. Yang, "High-efficiency solution processable polymer photovoltaic cells by self-organization of polymer blends," *Nat. Mater.*, vol. 4, pp. 864–868, 2005.

[7] A. Troisi, "Charge transport in high mobility molecular semiconductors: classical models and new theories," *Chem. Soc. Rev.*, vol. 40, pp. 2347–2358, 2011.

[8] V. Kalihari, E. B. Tadmor, G. Haugstad, and C. D. Frisbie, "Grain orientation mapping of polycrystalline organic semiconductor films by transverse shear microscopy," *Adv. Mater.*, vol. 20, no. 21, pp. 4033–4039, 2008.

[9] A. B. Chwang and C. D. Frisbie, "Temperature and gate voltage dependent transport across a single organic semiconductor grain boundary," *J. Appl. Phys*, vol. 90, no. 3, pp. 1342–1349, 2001.

[10] B. Chapman, A. Checco, R. Pindak, T. Siegrist, and C. Kloc, "Dislocations and grain boundaries in semiconducting rubrene single-crystals," *J. Cryst. Growth*, vol. 290, no. 2, pp. 479 – 484, 2006.

[11] W. L. Kalb, S. Haas, C. Krellner, T. Mathis, and B. Batlogg, "Trap density of states in small-molecule organic semiconductors: A quantitative comparison of thin-film transistors with single crystals," *Phys. Rev. B*, vol. 81, p. 155315, 2010.

[12] G. Horowitz and M. E. Hajlaoui, "Mobility in polycrystalline oligothiophene field-effect transistors dependent on grain size," *Adv. Mater.*, vol. 12, no. 14, pp. 1046–1050, 2000.

[13] S. F. Nelson, Y.-Y. Lin, D. J. Gundlach, and T. N. Jackson, "Temperature-independent transport in high-mobility pentacene transistors," *Appl. Phys. Lett.*, vol. 72, no. 15, pp. 1854–1856, 1998.

[14] T. Sakanoue and H. Sirringhaus, "Band-like temperature dependence of mobility in a solution-processed organic semiconductor," *Nat. Mater.*, vol. 9, pp. 736–740, 2010.

[15] S. S. Lee, C. S. Kim, E. D. Gomez, B. Purushothaman, M. F. Toney, C. Wang, A. Hexemer, J. E. Anthony, and Y.-L. Loo, "Controlling nucleation and crystallization in solution-processed organic semiconductors for thin-film transistors," *Adv. Mater.*, vol. 21, no. 35, pp. 3605–3609, 2009.

[16] J. Chen, C. K. Tee, M. Shtein, J. Anthony, and D. C. Martin, "Grain-boundary-limited charge transport in solution-processed 6,13 bis(tri-

isopropylsilylethynyl) pentacene thin film transistors," *J. Appl. Phys.*, vol. 103, no. 11, p. 114513, 2008.

[17] D. J. Gundlach, J. E. Royer, S. K. Park, S. Subramanian, and O. D. Jurchescu, "Contact-induced crystallinity for high-performance soluble acene-based transistors and circuits," *Nat. Mater.*, vol. 7, pp. 216–221, 2008.

[18] J. Rivnay, L. H. Jimison, J. E. Northrup, M. F. Toney, R. Noriega, S. Lu, T. J. Marks, A. Facchetti, and A. Salleo, "Large modulation of carrier transport by grain-boundary molecular packing and microstructure in organic thin films," *Nat. Mater.*, vol. 8, pp. 952–958, 2009.

[19] K. Dickey, J. Anthony, and Y.-L. Loo, "Improving organic thin-film transistor performance through solvent-vapor annealing of solution-processable triethylsilylethynyl anthradithiophene," *Adv. Mater.*, vol. 21, p. 392, 1976.

[20] M. Mladenović, N. Vukmirović, and I. Stanković, "Electronic states at low-angle grain boundaries in polycrystalline naphthalene," *J. Phys. Chem. C*, vol. 117, no. 30, pp. 15741–15748, 2013.

[21] L. G. Kaake, P. F. Barbara, and X.-Y. Zhu, "Intrinsic charge trapping in organic and polymeric semiconductors: A physical chemistry perspective," *J. Phys. Chem. Lett.*, vol. 1, no. 3, pp. 628–635, 2010.

[22] R. Noriega, J. Rivnay, K. Vandewal, F. P. Koch, N. Stingelin, P. Smith, M. F. Toney, and A. Salleo, "A general relationship between disorder, aggregation and charge transport in conjugated polymers," *Nat. Mater.*, vol. 12, no. 11, pp. 1038–1044, 2013.

[23] Y.-K. Lan and C.-I. Huang, "Charge mobility and transport behavior in the ordered and disordered states of the regioregular poly(3-hexylthiophene)," *J. Phys. Chem. B*, vol. 113, no. 44, pp. 14555–14564, 2009.

[24] N. Vukmirović and L. W. Wang, "Electronic structure of disordered conjugated polymers: Polythiophenes," *J. Phys. Chem. B*, vol. 113, no. 2, pp. 409–415, 2009.

[25] W. C. Tsoi, S. J. Spencer, L. Yang, A. M. Ballantyne, P. G. Nicholson, A. Turnbull, A. G. Shard, C. E. Murphy, D. D. C. Bradley, and J. Nelson, "Effect of crystallization on the electronic energy levels and thin film morphology of P3HT:PCBM blends," *Macromolecules*, vol. 44, no. 8, pp. 2944–2952, 2011.

[26] V. Coropceanu, J. Cornil, D. A. da Silva Filho, Y. Olivier, R. Silbey, and J.-L. Brédas, "Charge transport in organic semiconductors," *Chem. Rev.*, vol. 107, no. 4, pp. 926–952, 2007.

[27] N. Vukmirović, C. Bruder, and V. M. Stojanović, "Electron-phonon coupling in crystalline organic semiconductors: Microscopic evidence for nonpolaronic charge carriers," *Phys. Rev. Lett.*, vol. 109, p. 126407, 2012.

[28] W. L. Jorgensen and J. Tirado-Rives, "Monte Carlo vs molecular dynamics for conformational sampling," *J. Phys. Chem.*, vol. 100, no. 34, pp. 14508–14513, 1996.

[29] D. Frenkel and B. Smit, *Understanding Molecular Simulations*. San Diego, USA: Academic Press, 2002.

[30] M. Allen and D. J. Tildesley, *Computer Simulation of Liquids*. New York, USA: Clarendon Press, Oxford Science Publications, 1987.

[31] W. L. Jorgensen, D. S. Maxwell, and J. Tirado-Rives, "Development and testing of the OPLS all-atom force field on conformational energetics and properties of organic liquids," *J. Am. Chem. Soc.*, vol. 118, no. 45, pp. 11225–11236, 1996.

[32] P. Hohenberg and W. Kohn, "Inhomogeneous electron gas," *Phys. Rev.*, vol. 136, pp. B864–B871, 1964.

[33] W. Kohn, "Nobel lecture: Electronic structure of matter¯wave functions and density functionals," *Rev. Mod. Phys.*, vol. 71, pp. 1253–1266, 1999.

[34] R. O. Jones, "Density functional theory: Its origins, rise to prominence, and future," *Rev. Mod. Phys.*, vol. 87, pp. 897–923, 2015.

[35] R. G. Parr and W. Yang, *Density-Functional Theory of Atoms and Molecules*. New York, USA: Oxford University Press, 1989.

[36] R. M. Martin, *Electronic structure: Basic Theory and Practical Methods*. Cambridge, UK: Cambridge Press, 2004.

[37] W. Kohn and L. J. Sham, "Self-consistent equations including exchange and correlation effects," *Phys. Rev.*, vol. 140, pp. A1133–A1138, 1965.

[38] D. M. Ceperley and B. J. Alder, "Ground state of the electron gas by a stochastic method," *Phys. Rev. Lett.*, vol. 45, pp. 566–569, 1980.

[39] N. Vukmirović and L. W. Wang, "Charge patching method for electronic structure of organic systems," *J. Chem. Phys.*, vol. 128, p. 121102, 2008.

[40] N. Vukmirović and L.-W. Wang, "Overlapping fragments method for electronic structure calculation of large systems," *J. Chem. Phys.*, vol. 134, no. 9, p. 094119, 2011.

[41] J. C. Slater and G. F. Koster, "Simplified LCAO method for the periodic potential problem," *Phys. Rev.*, vol. 94, pp. 1498–1524, 1954.

[42] D. J. Chadi, "Atomic and electronic structures of reconstructed Si(100) surfaces," *Phys. Rev. Lett.*, vol. 43, pp. 43–47, 1979.

[43] P. Koskinen and V. M "Density-functional tight-binding for beginners," *Comput. Mater. Sci.*, vol. 47, no. 1, pp. 237 – 253, 2009.

[44] M. Elstner, D. Porezag, G. Jungnickel, J. Elsner, M. Haugk, T. Frauenheim, S. Suhai, and G. Seifert, "Self-consistent-charge density-functional tight-binding method for simulations of complex materials properties," *Phys. Rev. B*, vol. 58, pp. 7260–7268, 1998.

[45] R. S. Mulliken, "Electronic population analysis on LCAOMO molecular wave functions. I," *Jour. Chem. Phys*, vol. 23, no. 10, 1955.

[46] G. Seifert, "Tight-binding density functional theory: an approximate Kohn-Sham DFT scheme," *Jour. Phys. Chem. A*, vol. 111, no. 26, pp. 5609–5613, 2007.

[47] C. Wood and D. Jena, *Polarization Effects in Semiconductors: From Ab Initio Theory to Device Applications*. New York, USA: Springer, 2008.

[48] M. Posternak, A. Baldereschi, A. Catellani, and R. Resta, "*Ab initio* study of the spontaneous polarization of pyroelectric BeO," *Phys. Rev. Lett.*, vol. 64, pp. 1777–1780, 1990.

[49] R. Resta, "Macroscopic polarization in crystalline dielectrics: the geometric phase approach," *Rev. Mod. Phys.*, vol. 66, pp. 899–915, 1994.

[50] R. D. King-Smith and D. Vanderbilt, "Theory of polarization of crystalline solids," *Phys. Rev. B*, vol. 47, pp. 1651–1654, 1993.

[51] D. Vanderbilt and R. D. King-Smith, "Electric polarization as a bulk quantity and its relation to surface charge," *Phys. Rev. B*, vol. 48, pp. 4442–4455, 1993.

[52] F. Bernardini, V. Fiorentini, and D. Vanderbilt, "Spontaneous polarization and piezoelectric constants of III-V nitrides," *Phys. Rev. B*, vol. 56, pp. 10024–10027, 1997.

[53] N. A. Spaldin, "A beginner's guide to the modern theory of polarization," *J. Solid State Chem.*, vol. 195, pp. 2 – 10, 2012.

[54] A. D. Carlo, F. Piacenza, A. Bolognesi, B. Stadlober, and H. Maresch, "Influence of grain sizes on the mobility of organic thin-film transistors," *Appl. Phys. Lett.*, vol. 86, no. 26, p. 263501, 2005.

[55] S. Verlaak, V. Arkhipov, and P. Heremans, "Modeling of transport in polycrystalline organic semiconductor films," *Appl. Phys. Lett.*, vol. 82, no. 5, pp. 745–747, 2003.

[56] G. Horowitz, "Tunneling current in polycrystalline organic thin-film transistors," *Adv. Funct. Mater.*, vol. 13, no. 1, pp. 53–60, 2003.

[57] S. Verlaak and P. Heremans, "Molecular micromolecular view on electronic states near pentacene grain boundaries," *Phys. Rev. B*, vol. 75, p. 115127, 2007.

[58] A. Troisi and G. Orlandi, "Charge-transport regime of crystalline organic semiconductors: Diffusion limited by thermal off-diagonal electronic disorder," *Phys. Rev. Lett.*, vol. 96, p. 086601, 2006.

[59] G. Nan, X. Yang, L. Wang, Z. Shuai, and Y. Zhao, "Nuclear tunneling effects of charge transport in rubrene, tetracene, and pentacene," *Phys. Rev. B*, vol. 79, no. 11, p. 115203, 2009.

[60] Z. Shuai, L. Wang, and Q. Li, "Evaluation of charge mobility in organic materials: From localized to delocalized descriptions at a first-principles level," *Adv. Mater.*, vol. 23, no. 9, pp. 1145–1153, 2011.

[61] R. S. Sánchez-Carrera, S. Atahan, J. Schrier, and A. Aspuru-Guzik, "Theoretical characterization of the air-stable, high-mobility dinaphtho[2,3-b:2´ 3´-f]thieno[3,2-b]-thiophene organic semiconductor," *J. Phys. Chem. C*, vol. 114, no. 5, pp. 2334–2340, 2010.

[62] K. Hannewald, V. M. Stojanović, J. M. T. Schellekens, P. A. Bobbert, G. Kresse, and J. Hafner, "Theory of polaron bandwidth narrowing in organic molecular crystals," *Phys. Rev. B*, vol. 69, no. 7, p. 075211, 2004.

[63] F. Ortmann, F. Bechstedt, and K. Hannewald, "Theory of charge transport in organic crystals: Beyond Holstein's small-polaron model," *Phys. Rev. B*, vol. 79, p. 235206, 2009.

[64] N. G. Martinelli, Y. Olivier, S. Athanasopoulos, M.-C. Ruiz Delgado, K. R. Pigg, D. A. da Silva Filho, R. S. Sánchez-Carrera, E. Venuti, R. G. Della Valle, and J.-L. e. Brédas, "Influence of intermolecular vibrations on the electronic coupling in organic semiconductors: The case of anthracene and perfluoropentacene," *Chem. Phys. Chem.*, vol. 10, pp. 2265–2273, 2009.

[65] S. Ciuchi and S. Fratini, "Electronic transport and quantum localization effects in organic semiconductors," *Phys. Rev. B*, vol. 86, p. 245201, 2012.

[66] S. Ciuchi, S. Fratini, and D. Mayou, "Transient localization in crystalline organic semiconductors," *Phys. Rev. B*, vol. 83, p. 081202, 2011.

[67] S. Ciuchi and S. Fratini, "Band dispersion and electronic lifetimes in crystalline organic semiconductors," *Phys. Rev. Lett.*, vol. 106, p. 166403, 2011.

[68] C. A. Perroni, V. Marigliano Ramaglia, and V. Cataudella, "Effects of electron coupling to intramolecular and intermolecular vibrational modes on the transport properties of single-crystal organic semiconductors," *Phys. Rev. B*, vol. 84, p. 014303, 2011.

[69] N. Vukmirović, C. Bruder, and V. M. Stojanović, "Electron-phonon coupling in crystalline organic semiconductors: Microscopic evidence for nonpolaronic charge carriers," *Phys. Rev. Lett.*, vol. 109, p. 126407, 2012.

[70] G. Schweicher, V. Lemaur, C. Niebel, C. Ruzi, Y. Diao, O. Goto, W.-Y. Lee, Y. Kim, J.-B. Arlin, and t. . B. j. . A. v. . . n. . . i. . . u. . h. d. . a. p. . . k. . h. y. . . Karpinska, Jolanta, et al

[71] M. G. Martin and J. I. Siepmann, "Transferable potentials for phase equilibria. 1. united-atom description of n-alkanes," *J. Phys. Chem. B*, vol. 102, pp. 2569–2577, 1998.

[72] C. D. Wick, M. G. Martin, and J. I. Siepmann, "Transferable potentials for phase equilibria. 4. united-atom description of linear and branched alkenes and alkylbenzenes," *J. Phys Chem. B*, vol. 104, no. 33, pp. 8008–8016, 2000.

[73] M. Schwoerer and H. C. Wolf, *Organic Molecular Solids*. Wienheim, Germany: WILEY-VCH Verlag, 2008.

[74] K. Hummer and C. Ambrosch-Draxl, "Electronic properties of oligoacenes from first principles," *Phys. Rev. B*, vol. 72, p. 205205, 2005.

[75] R. S. Sánchez-Carrera, P. Paramonov, G. M. Day, V. Coropceanu, and J.-L. Brédas, "Interaction of charge carriers with lattice vibrations in oligoacene crystals from naphthalene to pentacene," *J. Am. Chem. Soc.*, vol. 132, no. 41, pp. 14437–14446, 2010.

[76] I. Stankovic, S. Hess, and M. Kröger, "Structural changes and viscoplastic behavior of a generic embedded-atom model metal in steady shear flow," *Phys. Rev. E*, vol. 69, p. 021509, 2004.

[77] J. Chen, C. K. Tee, J. Yang, C. Shaw, M. Shtein, J. Anthony, and D. C. Martin, "Thermal and mechanical cracking in bis (triisopropylsilylethnyl) pentacene thin films," *J. Polym. Sci. Pt. B-Polym. Phys.*, vol. 44, no. 24, pp. 3631–3641, 2006.

[78] S. Verlaak, C. Rolin, and P. Heremans, "Microscopic description of elementary growth processes and classification of structural defects in pentacene thin films," *J. Phys. Chem. B*, vol. 111, no. 1, pp. 139–150, 2007.

[79] N. Vukmirović and L.-W. Wang, "Density of states and wave function localization in disordered conjugated polymers: A large scale computational study," *J. Phys. Chem. B*, vol. 115, no. 8, pp. 1792–1797, 2011.

[80] T. Vehoff, B. Baumeier, A. Troisi, and D. Andrienko, "Charge transport in organic crystals: Role of disorder and topological connectivity," *J. Am. Chem. Soc.*, vol. 132, no. 33, pp. 11702–11708, 2010.

[81] A. Troisi and D. L. Cheung, "Transition from dynamic to static disorder in one-dimensional organic semiconductors," *J. Chem. Phys.*, vol. 131, no. 1, p. 014703, 2009.

[82] A. Troisi, "Dynamic disorder in molecular semiconductors: Charge transport in two dimensions," *J. Chem. Phys.*, vol. 134, no. 3, p. 034702, 2011.

[83] J. Böhlin, M. Linares, and S. Stafström, "Effect of dynamic disorder on charge transport along a pentacene chain," *Phys. Rev. B*, vol. 83, p. 085209, 2011.

[84] Y. Yao, W. Si, X. Hou, and C.-Q. Wu, "Monte carlo simulation based on dynamic disorder model in organic semiconductors: From coherent to incoherent transport," *J. Chem. Phys.*, vol. 136, no. 23, p. 234106, 2012.

[85] S. Fratini and S. Ciuchi, "Bandlike motion and mobility saturation in organic molecular semiconductors," *Phys. Rev. Lett.*, vol. 103, p. 266601, 2009.

[86] A. Troisi and G. Orlandi, "Charge-transport regime of crystalline organic semiconductors: Diffusion limited by thermal off-diagonal electronic disorder," *Phys. Rev. Lett.*, vol. 96, p. 086601, 2006.

[87] D. L. Cheung, D. P. McMahon, and A. Troisi, "A realistic description of the charge carrier wave function in microcrystalline polymer semiconductors," *J. Am. Chem. Soc.*, vol. 131, no. 31, pp. 11179–11186, 2009.

[88] D. P. McMahon, D. L. Cheung, L. Goris, J. Dacuna, A. Salleo, and A. Troisi, "Relation between microstructure and charge transport in polymers of different regioregularity," *J. Phys. Chem. C*, vol. 115, no. 39, pp. 19386–19393, 2011.

[89] T. Liu and A. Troisi, "Understanding the microscopic origin of the very high charge mobility in PBTTT: Tolerance of thermal disorder," *Adv. Funct. Mater.*, vol. 24, no. 7, pp. 925–933, 2013.

[90] M. Mladenović and N. Vukmirović, "Charge carrier localization and transport in organic semiconductors: Insights from atomistic multiscale simulations," *Adv. Funct. Mater.*, vol. 25, no. 13, pp. 1915–1932, 2015.

[91] D. L. Cheung, D. P. McMahon, and A. Troisi, "Computational study of the structure and charge-transfer parameters in low-molecular-mass P3HT," *J. Phys. Chem. B*, vol. 113, no. 28, pp. 9393–9401, 2009.

[92] O. Alexiadis and V. G. Mavrantzas, "All-atom molecular dynamics simulation of temperature effects on the structural, thermodynamic, and packing properties of the pure amorphous and pure crystalline phases of regioregular P3HT," *Macromolecules*, vol. 46, no. 6, pp. 2450–2467, 2013.

[93] S. Dag and L.-W. Wang, "Packing structure of poly(3-hexylthiophene) crystal: Ab initio and molecular dynamics studies," *J. Phys. Chem. B*, vol. 114, no. 18, pp. 5997–6000, 2010.

[94] W. Xie, Y. Y. Sun, S. B. Zhang, and J. E. Northrup, "Structure and sources of disorder in poly(3-hexylthiophene) crystals investigated by density functional calculations with van der Waals interactions," *Phys. Rev. B*, vol. 83, p. 184117, 2011.

[95] C. Poelking and D. Andrienko, "Effect of polymorphism, regioregularity and paracrystallinity on charge transport in poly(3-hexylthiophene) [P3HT] nanofibers," *Macromolecules*, vol. 46, no. 22, pp. 8941–8956, 2013.

[96] R. S. Bhatta, Y. Y. Yimer, D. S. Perry, and M. Tsige, "Improved force field for molecular modeling of poly(3-hexylthiophene)," *J. Phys. Chem. B*, vol. 117, no. 34, pp. 10035–10045, 2013.

[97] M. Moreno, M. Casalegno, G. Raos, S. V. Meille, and R. Po, "Molecular modeling of crystalline alkylthiophene oligomers and polymers," *J. Phys. Chem. B*, vol. 114, no. 4, pp. 1591–1602, 2010.

[98] T. J. Prosa, M. J. Winokur, J. Moulton, P. Smith, and A. J. Heeger, "X-ray structural studies of poly(3-alkylthiophenes): an example of an inverse comb," *Macromolecules*, vol. 25, no. 17, pp. 4364–4372, 1992.

[99] R. Colle, G. Grosso, A. Ronzani, and C. M. Zicovich-Wilson, "Structure and x-ray spectrum of crystalline poly(3-hexylthiophene) from DFT-van der Waals calculations," *Phys. Status Solidi B*, vol. 248, no. 6, pp. 1360–1368, 2011.

[100] N. Kayunkid, S. Uttiya, and M. Brinkmann, "Structural model of regioregular poly(3-hexylthiophene) obtained by electron diffraction analysis," *Macromolecules*, vol. 43, no. 11, pp. 4961–4967, 2010.

[101] A. Maillard and A. Rochefort, "Structural and electronic properties of poly(3-hexylthiophene) π-stacked crystals," *Phys. Rev. B*, vol. 79, p. 115207, 2009.

[102] K. D. Meisel, H. Vocks, and P. A. Bobbert, "Polarons in semiconducting polymers: Study within an extended Holstein model," *Phys. Rev. B*, vol. 71, p. 205206, 2005.

[103] S. Zade and M. Bendikov, "Study of hopping transport in long oligothiophenes and oligoselenophenes: Dependence of reorganization energy on chain length," *Chem. Eur. J.*, vol. 14, no. 22, pp. 6734–6741, 2008.

[104] N. F. Mott and E. A. Davis, *Electronic Processes in Non-Crystalline Materials*. New York, USA: Clarendon Press, 1979.

[105] E. J. W. Crossland, K. Tremel, F. Fischer, K. Rahimi, G. Reiter, U. Steiner, and S. Ludwigs, "Anisotropic charge transport in spherulitic poly(3-hexylthiophene) films," *Adv. Mater.*, vol. 24, no. 6, pp. 839–844, 2012.

[106] M. Brinkmann and J.-C. Wittmann, "Orientation of regioregular poly(3-hexylthiophene) by directional solidification: A simple method to reveal the semicrystalline structure of a conjugated polymer," *Adv. Mater.*, vol. 18, no. 7, pp. 860–863, 2006.

[107] S. Sweetnam, K. R. Graham, G. O. Ngongang Ndjawa, T. Heumüller, J. A. Bartelt, T. M. Burke, W. Li, W. You, A. Amassian, and M. D. McGehee, "Characterization of the polymer energy landscape in polymer:fullerene bulk heterojunctions with pure and mixed phases," *J. Am. Chem. Soc*, vol. 136, no. 40, pp. 14078–14088, 2014.

[108] M. Mladenović and N. Vukmirović, "Effects of thermal disorder on the electronic properties of ordered polymers," *Phys. Chem. Chem. Phys.*, vol. 16, pp. 25950–25958, 2014.

[109] M. Pfaff, M. F. Klein, E. Müller, P. Müller, A. Colsmann, U. Lemmer, and D. Gerthsen, "Nanomorphology of P3HT:PCBM-based absorber layers of organic solar cells after different processing conditions analyzed by low-energy scanning transmission electron microscopy," *Microsc. Microanal.*, vol. 18, pp. 1380–1388, 2012.

[110] J. B. Neaton, C. Ederer, U. V. Waghmare, N. A. Spaldin, and K. M. Rabe, "First-principles study of spontaneous polarization in multiferroic $BiFeO_3$," *Phys. Rev. B*, vol. 71, p. 014113, 2005.

[111] F.-C. Sun, A. M. Dongare, A. D. Asandei, S. Pamir Alpay, and S. Nakhmanson, "Temperature dependent structural, elastic, and polar properties of ferroelectric polyvinylidene fluoride (PVDF) and trifluoroethylene (TrFE) copolymers," *J. Mater. Chem. C*, vol. 3, pp. 8389–8396, 2015.

[112] X. Gonze, B. Amadon, P.-M. Anglade, J.-M. Beuken, F. Bottin, P. Boulanger, F. Bruneval, D. Caliste, R. Caracas, and M. M. Côté, et al, "Abinit: First-principles approach to material and nanosystem properties," *Comput. Phys. Commun.*, vol. 180, no. 12, pp. 2582 – 2615, 2009.

[113] P. Giannozzi, S. Baroni, N. Bonini, M. Calandra, R. Car, C. Cavazzoni, D. Ceresoli, G. L. Chiarotti, M. Cococcioni, and I. Dabo, et al, "Quantum espresso: a modular and open-source software project for quantum simulations of materials," *J. Phys. Condens. Matter*, vol. 21, no. 39, p. 395502, 2009.

[114] D. Dudenko, A. Kiersnowski, J. Shu, W. Pisula, D. Sebastiani, H. W. Spiess, and M. R. Hansen, "A strategy for revealing the packing in semicrystalline π-conjugated polymers: Crystal structure of bulk poly-3-hexyl-thiophene (P3HT)," *Angew. Chem. Int. Ed.*, vol. 51, no. 44, pp. 11068–11072, 2012.

[115] A. Maillard and A. Rochefort, "Role of structural order at the P3HT/C60 heterojunction interface," *Org. Electron.*, vol. 15, no. 9, pp. 2091 – 2098, 2014.

[116] B. Aradic and B. H. T. Frauenheim, "DFTB+, a sparse matrix-based implementation of the DFTB method," *J. Phys. Chem. A*, vol. 111, no. 26, pp. 5678–5684, 2007.

[117] C. R. Snyder and J. F. Douglas, "Determination of the dielectric constant of nanoparticles. 1. dielectric measurements of buckminsterfullerene solutions," *J. Phys. Chem. B*, vol. 104, no. 47, pp. 11058–11065, 2000.

Publications list

[1] M. Mladenović, N. Vukmirović and I. Stanković, Electronic states at low-angle grain boundaries in polycrystalline naphthalene, *J. Phys. Chem. C*,vol. 117, no. 30, pp. 15741-15748, 2013.

[2] M. Mladenović and N. Vukmirović, Effects of thermal disorder on the electronic properties of ordered polymers, *Phys. Chem. Chem. Phys.*, vol. 16, pp. 25950-25958, 2014.

[3] M. Mladenović and N. Vukmirović, Charge carrier localization and transport in organic semiconductors: Insights from atomistic multiscale simulations, *Adv. Funct. Mater.*, vol. 25, no. 13, pp. 1915-1932, 2015.

[4] M. Mladenović and N. Vukmirović, Electronic states at the interface between crystalline and amorphous domains in conjugated polymers, *J. Phys. Chem. C*, vol. 119, no. 41, pp. 23329-23333, 2015.

[5] M. Mladenović and N. Vukmirović, Spontaneous polarization induced by side chains in ordered poly(3-hexylthiophene), *J. Phys. Chem. C*, vol. 120, no. 33, pp. 18895-18900, 2016.

Biography

Marko Mladenović was born in 1988 in Zaječar, Serbia. He has finished Mathematical Gymnasium in Belgrade in 2007. Then, he started his undergraduate studies at the School of Electrical Engineering, University of Belgrade, which we has finished in 2011 as the best student at the module of Nanoelectronics, Optoelectronics and Laser Technique. Next year, he has finished his master studies at the same module. Later that year, he started his PhD studies at the same school at the module of Nanoelectronics and Photonics.

Marko Mladenović has started his research at the Scientific Computing Belgrade, Institute of Physics Belgrade in 2011 under the supervision of Dr Nenad Vukmirović. His research interests include atomic and electronic structure of organic semiconductors. During his master and PhD studies he has published 4 regular articles and 1 review article. He attended several conferences and schools. At the European Materials Research Society Conference in 2014 he received graduate student award.

Изјава о ауторству

Име и презиме аутора Марко Младеновић

Број индекса 5021/2012

Изјављујем

да је докторска дисертација под насловом

Електронска својства органских полупроводника на границама домена

- резултат сопственог истраживачког рада;
- да дисертација у целини ни у деловима није била предложена за стицање друге дипломе према студијским програмима других високошколских установа;
- да су резултати коректно наведени и
- да нисам кршио/ла ауторска права и користио/ла интелектуалну својину других лица.

Потпис аутора

У Београду, 31.8.2016.

Марко Младеновић

Изјава о истоветности штампане и електронске верзије докторског рада

Име и презиме аутора Марко Младеновић

Број индекса 5021/2012

Студијски програм Наноелектроника и фотоника

Наслов рада Електронска својства органских полупроводника на границама домена

Ментор проф. др. Јелена Радовановић

Изјављујем да је штампана верзија мог докторског рада истоветна електронској верзији коју сам предао/ла ради похрањена у **Дигиталном репозиторијуму Универзитета у Београду.**

Дозвољавам да се објаве моји лични подаци везани за добијање академског назива доктора наука, као што су име и презиме, година и место рођења и датум одбране рада.

Ови лични подаци могу се објавити на мрежним страницама дигиталне библиотеке, у електронском каталогу и у публикацијама Универзитета у Београду.

Потпис аутора

У Београду, 31.8.2016.

Марко Младеновић

Изјава о коришћењу

Овлашћујем Универзитетску библиотеку „Светозар Марковић“ да у Дигитални репозиторијум Универзитета у Београду унесе моју докторску дисертацију под насловом:

Електронска својства органских полупроводника на границама домена

која је моје ауторско дело.

Дисертацију са свим прилозима предао/ла сам у електронском формату погодном за трајно архивирање.

Моју докторску дисертацију похрањену у Дигиталном репозиторијуму Универзитета у Београду и доступну у отвореном приступу могу да користе сви који поштују одредбе садржане у одабраном типу лиценце Креативне заједнице (Creative Commons) за коју сам се одлучио/ла.

1. Ауторство (CC BY)

2. Ауторство – некомерцијално (CC BY-NC)

3. Ауторство – некомерцијално – без прерада (CC BY-NC-ND)

4. Ауторство – некомерцијално – делити под истим условима (CC BY-NC-SA)

5. Ауторство – без прерада (CC BY-ND)

6. Ауторство – делити под истим условима (CC BY-SA)

(Молимо да заокружите само једну од шест понуђених лиценци.
Кратак опис лиценци је саставни део ове изјаве).

Потпис аутора

У Београду, 31.8.2016.

Марко Младеновић

1. **Ауторство**. Дозвољавате умножавање, дистрибуцију и јавно саопштавање дела, и прераде, ако се наведе име аутора на начин одређен од стране аутора или даваоца лиценце, чак и у комерцијалне сврхе. Ово је најслободнија од свих лиценци.

2. **Ауторство – некомерцијално**. Дозвољавате умножавање, дистрибуцију и јавно саопштавање дела, и прераде, ако се наведе име аутора на начин одређен од стране аутора или даваоца лиценце. Ова лиценца не дозвољава комерцијалну употребу дела.

3. **Ауторство – некомерцијално – без прерада**. Дозвољавате умножавање, дистрибуцију и јавно саопштавање дела, без промена, преобликовања или употребе дела у свом делу, ако се наведе име аутора на начин одређен од стране аутора или даваоца лиценце. Ова лиценца не дозвољава комерцијалну употребу дела. У односу на све остале лиценце, овом лиценцом се ограничава највећи обим права коришћења дела.

4. **Ауторство – некомерцијално – делити под истим условима**. Дозвољавате умножавање, дистрибуцију и јавно саопштавање дела, и прераде, ако се наведе име аутора на начин одређен од стране аутора или даваоца лиценце и ако се прерада дистрибуира под истом или сличном лиценцом. Ова лиценца не дозвољава комерцијалну употребу дела и прерада.

5. **Ауторство – без прерада**. Дозвољавате умножавање, дистрибуцију и јавно саопштавање дела, без промена, преобликовања или употребе дела у свом делу, ако се наведе име аутора на начин одређен од стране аутора или даваоца лиценце. Ова лиценца дозвољава комерцијалну употребу дела.

6. **Ауторство – делити под истим условима**. Дозвољавате умножавање, дистрибуцију и јавно саопштавање дела, и прераде, ако се наведе име аутора на начин одређен од стране аутора или даваоца лиценце и ако се прерада дистрибуира под истом или сличном лиценцом. Ова лиценца дозвољава комерцијалну употребу дела и прерада. Слична је софтверским лиценцама, односно лиценцама отвореног кода.